Mars' Water Cycle Seen Through an Ice Lens

Jonathan Bapst

A dissertation

submitted in partial fulfillment of the

requirements for the degree of

Doctor of Philosophy

University of Washington

2018

Reading Committee:

Joshua L. Bandfield, Chair

Shane Byrne

Michelle Koutnik

Program Authorized to Offer Degree:

Earth and Space Sciences

University of Washington

Abstract

Mars' Water Cycle Seen Through an Ice Lens

Jonathan N. Bapst

Chair of the Supervisory Committee:
Dr. Joshua L. Bandfield
Department of Earth and Space Sciences

The water cycle of Mars has been intensely studied thanks to data from orbiting spacecraft and landers on the surface. Water is of major interest due to its vital connection to life on Earth. The global cycle is driven by the planet's major source of water vapor, the north polar residual water-ice cap, and the amount of this vapor is very sensitive to polar insolation. Climate can be expressed in the behavior of water ice present at the surface, both seasonally and perennially. Here, I enhance our knowledge of Mars' current and recent climate by investigating the occurrence and physical structure of water ice at the surface with a combination of data analysis and numerical modeling.

In chapter 2 I analyze surface temperatures and albedo from broadband thermal-infrared and visible observations, in order to characterize the seasonal cycle of water frost. I identify extensive deposition of water ice in the northern hemisphere during autumn, whereas the southern hemisphere shows little evidence for water ice deposition. I argue this is a result of the configuration of major water sources at present (i.e., the primary source of water vapor being at the north pole).

In chapter 3 I analyze the stability of icy outliers of the northern polar cap of Mars with both high-resolution imagery and numerical models. These outliers are mounds of water ice ~10-50 km in diameter, up to ~2 km thick, and are not contiguous with the residual cap (the most-equatorward being at 70ºN). They are potentially unstable, so secular changes in mound extent are explored using multi-year high-resolution images. I estimate the current annual mass balance using a coupled 1-D thermal and atmospheric model. Both lines of study support the outliers being close to equilibrium, suggesting, at present, surface deposits may equilibrate at the same pace as the changing orbit.

In chapter 4 I derive maps of thermophysical properties of the north polar residual cap itself with thermal models and binned temperature data. I investigate depth-density relationships in the polar water ice deposit and find that porous ice overlies a denser ice substrate, which could indicate recent accumulation. We find a noticeable difference between the interior and edge of the residual cap, supporting recent accumulation over the interior and ablation at the edges. The properties I derive will provide insight into the recent behavior of the martian north polar residual cap, which remains largely unknown.

TABLE OF CONTENTS

LIST OF FIGURES

LIST OF TABLES

ACKNOWLEDGEMENTS

In 2010, I moved away from my home of almost 23 years, Buffalo, New York. My destination was Seattle, where I would begin my studies as a planetary scientist at the University of Washington. Since that time, I have been aided by and have relied upon others to advise me on matters pertaining to science, as well as those beyond. In this section I will acknowledge those who have helped along the way.

I want to thank my academic advisors. Steve Wood, as my first advisor, introduced a mechanical engineer to the topic of martian glaciology among others. He pushed me to present at my first conference less than three months into my tenure as a graduate student. A few years later, Josh Bandfield advised me through my first publication. Josh remained in a major role as my primary advisor, although we were both remote from the university and one another. As my area of research continued to overlap with Josh's area of expertise, this collaboration between us proved invaluable. In the summer of 2014 I moved to Tucson, Arizona, where I began my work with Shane Byrne at the University of Arizona. I could not have asked for a better advisor to see me through an unconventional situation. Shane not only helped guide me through the remainder of my dissertation research, but also proved to be a great influence and friend. Shane is ultra-reliable and never failed to help find solutions when situations got tough. I'd lastly like to thank the rest of my advisory committee for their help and understanding throughout: Michelle, Russ, John and Ed.

The list of personal friends, fellow graduate students, and post-docs that have helped me along my journey in graduate school is too long to list here, and quite frankly, too many to remember. From my time spent in Seattle I would like to thank Adam, Jason, Elena, Frances, Brendan, Ryan, Bret, Logan, Mike, Shelley, Nick, and Devin. From Arizona I would like to thank Mike, Ali, Sarah, Molly, Patricio, Alex, James, Michelle, and Jamie. My brother David, who was both a graduate student and a post-doc during this time, also provided important advice (in addition to sending me cute photos of my niece, Robin). Graduate school is as much about life outside of the office as it is within. Without support from these people, finishing my studies would not have been possible.

Thank you to the administrative staff from both Washington (Noéll, Eunice, Kathy and Ed) and Arizona (Mary, Bert, Tara, Sue, Edith, and Theresa). Without you, nothing would get done (seriously).

I'd like to thank the Astrobiology Program and Vikki Meadows, in particular, for creating such a unique yet immersive program for graduate students. This program has prepared me for interdisciplinary work that will be present in future projects. Some of my best memories of graduate school come from workshops or gatherings with the astrobiology group.

Lastly, I would like to acknowledge my funding sources. The previously mentioned Astrobiology Program helped support my final quarter tuition, in addition to a number of other examples. The NASA Earth and Space Sciences Fellowship supported me for 3 years and provided me with flexibility to explore my own research ideas. From my second year in Tucson until finishing, the NASA Mars Data Analysis Program has supported my research, allowing me to complete this dissertation.

DEDICATION

*To my sister, Kat*e

Chapter 1. INTRODUCTION

Mars exploration has been driven primarily by the tantalizing prospect of life being present today or at some point in the past. Over the past half century orbiting spacecraft and landers at the surface have made key measurements of martian environmental conditions and all reach the same general conclusion: Present-day Mars is far from habitable by standards for Earth life. Billions of years ago Mars may have had abundant liquid water at its surface, but that is not possible today as the mean-annual temperature at the equator is ~220 K (Kieffer *et al*., 1977; Christensen *et al*., 2001), and the atmosphere is ~10^4 times drier than Earth (Smith, 2008). Liquid water, a necessity for life as we know it, is possible only in the deep (~kilometers) subsurface (Ingersoll, 1970; Clifford, 1993), and is largely inaccessible by current spacecraft technology. Near the surface, water can exist in three states: ice, vapor and adsorbate (the latter is not discussed further).

The majority of the known inventory of water is in the form of ice, and is stored in the polar regions as thick sequences built over geologic time; i.e., the Polar Layered Deposits (NPLD and SPLD, for the north and south, respectively; Byrne, 2009). The atmospheric water cycle is controlled by vapor released by the exposed residual water-ice cap at the north pole during summer (Smith, 2002). This configuration is determined by Mars' current orbit and how solar flux varies with latitude. However, Mars experiences cyclical changes in orbital elements (Laskar *et al*., 2004). Because the primary source of water vapor is at the poles, the amount of water in the atmosphere is very sensitive to any changes in insolation, thus conditions have changed over time, even in the geologically-recent past.

The martian orbital history is known for the past ~20 Myr (Laskar *et al*., 2004). Mars' obliquity follows ~120 kyr period where it will often oscillate by ~20º. Mars at present is in an anomalous orbital state where the amplitude of obliquity changes is dampened to only a few degrees per period. Multiple lines of evidence suggest that previous epochs, when large changes in obliquity occur, are characterized by planetary-scale migration of water ice (Head *et al*., 2003; Forget *et al*., 2006; Byrne, 2009; Schorghofer and Forget, 2012). Due to the current low-amplitude period, geographic transport of water ice is relatively inactive and there are relatively small amounts of water in the atmosphere (Mischna *et al*., 2003; Chamberlain and Boynton, 2007). There are many outstanding questions concerning the present, that may also inform us on the past. For example, it is unclear whether water ice is accumulating or ablating at the pole(s). Understanding the climate system at present can provide clues to its behavior during more dynamic periods.

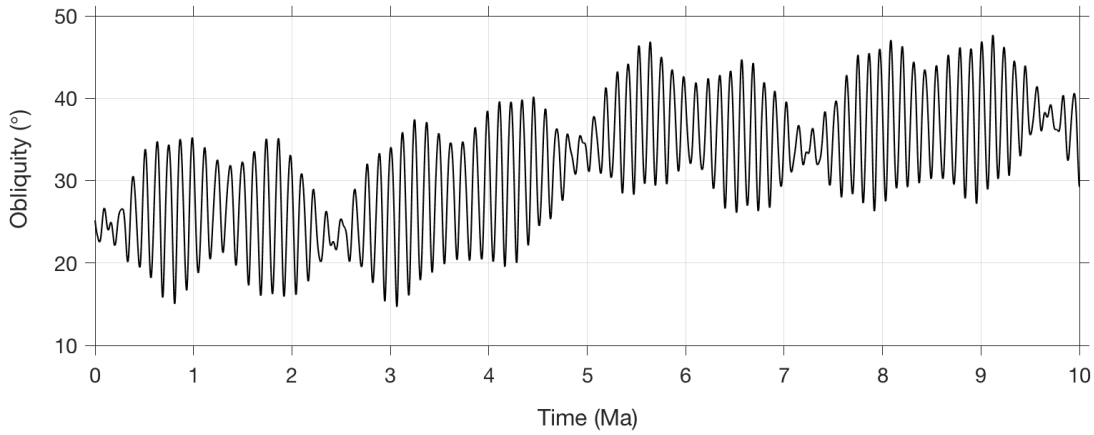

Figure 1.1. Mars' obliquity history for the past 10 Myr from Laskar *et al*. (2004).

Our knowledge of the global water cycle largely comes from studying water vapor in the atmosphere, and how it varies seasonally (Smith, 2002; 2008). The work presented here centers on the water cycle, but from the perspective of water ice, which can provide insight into the

climate on scales larger than those of the annual atmospheric cycle. Each Chapter focuses on a different occurrence of water ice and its connection to the climate. Chapters are written as stand-alone journal articles, with two already having been published (Chapters 2 and 3; see citation listed at chapter title page).

Chapter 2 explores the presence of seasonal water-ice frost. This work involves the identification and mapping of extensive seasonal water ice in the northern polar and upper mid-latitudes (comparably few detections were made in the south). This form of seasonal ice was observed at the Viking 2 Lander site, where it appeared as a thin layer (<1 mm), and both continuous and patchy (Svitek and Murray, 1990). The seasonal cycle of frost is consistent with the current configuration of exposed water ice (i.e., the water source being only in the north).

Chapter 3 focuses on mounds of water ice that are located within north polar craters and are on the geographic edge of where surface ice is present (and presumably stable). High-resolution images are analyzed along the boundary of the lowest-latitude ice mound in Louth crater. This mound has been interpreted to be ablating in the recent past based on geomorphic evidence (Brown *et al*., 2008). Thermal properties of mound water ice are constrained using observed temperatures over a larger ice mound in Korolev crater, which is slightly closer to the pole. Modeled temperatures are used in conjunction with an atmospheric-mixing model to produce estimates of the annual mass balance for both locations.

Deriving thermal properties over the residual ice cap, and NPLD outliers, is the emphasis of Chapter 4. Similar to Chapter 3, observed temperatures and a number of model simulations are used to determine best-fit thermal properties. In addition to studying how thermal properties change across the polar region, the vertical structure of ice is of major interest here. Various thermal models are constructed to explore depth-density relationships in residual ice and are

tested against the data. Depth-density relationships can inform us on the recent history of polar accumulation as the density of ice, in addition to depth-dependent, is also time-dependent (Arthern *et al*., 2000; Bramson *et al*., 2017).

Where ice is present today and in the recent past may lead us to promising sites where habitability is possible during favorable climatic periods. Understanding the present is key to understanding the past. This work will assist us in predicting the extent and behavior of water ice in previous climates.

Chapter 2. HEMISPHERIC ASYMMETRY IN MARTIAN SEASONAL SURFACE WATER ICE FROM MGS TES

Published in the journal Icarus
Bapst, J., Bandfield, J.L., Wood, S.E., 2015. Hemispheric asymmetry in martian seasonal surface water ice from MGS TES. Icarus 260, 396–408. doi:10.1016/j.icarus.2015.07.025

2.1 INTRODUCTION

2.1.1 *Background*

Understanding the climate of Mars, both past and present, is a major goal of Mars exploration. Both orbiting spacecraft and lander datasets are crucial for testing models and hypotheses related to processes of the martian climate. Volatiles have been a major focus because their behavior reflects the state of the climate (Leighton and Murray, 1966). Mars experiences seasonal variations that result in the formation of seasonal surface ice deposits that can be identified, to first order, due to their high albedo. Compositionally, there are two major volatiles in the climate system that can form seasonal frosts: CO_2 and H_2O. In this work, the terms frost and surface ice are synonymous and are used interchangeably and the name does not reflect depositional processes (e.g., precipitation, hoar frost, etc.).

CO_2 makes up about 95% of the martian atmosphere and has a surface frost point temperature of ~148 K (Leighton and Murray, 1966; Kieffer *et al.*, 1992). Because it is the major species in the atmosphere, the surface temperature cannot drop appreciably below this temperature (as it is buffered by the release of latent heat of deposition). Thus, winter hemispheres on Mars include seasonal deposits of CO_2 ice. The atmospherically-derived ice caps cause the total pressure of the atmosphere to vary by ~25% (Wood and Paige, 1992). By contrast, water is a minor constituent of the martian atmosphere (~0.005% by volume) and has

an estimated mean-annual frost point temperature of ~200 K (Kieffer *et al*., 1992). Because of its low number density, the latent heat of water phase transitions has little effect on surface temperatures. Therefore, water frost can be present over a wide range of temperatures below its ~200 K frost point. The temperature contrast between these two ices is crucial for distinguishing ice composition with thermal infrared measurements (e.g., Kieffer and Titus, 2001).

Systematic mapping of the spatial and temporal occurrence of these volatiles in the martian atmosphere, on the surface, and in the subsurface is important for understanding the climate of Mars. Ices at the surface can also be broken into three temporal categories: diurnal, seasonal, and perennial. Diurnal frosts are present for no longer than one sol, and are typically restricted to nighttime when surface temperatures are lowest. Seasonal frosts, most relevant to this work, are present for more than one sol and can affect surface thermophysical properties, as well as the surface energy balance via changes in albedo and the absorption or release of latent heat due to phase transitions (evident in CO_2 seasonal ice). Perennial ices persist throughout the year and are believed to be primary sinks and sources for volatiles in the present martian climate (Jakosky and Farmer, 1982; Smith, 2002; Byrne, 2009).

Much of what we know of the global water cycle is from atmospheric measurements of water vapor (e.g., Jakosky and Farmer, 1982; Smith, 2002; 2004). The largest source of water vapor appears to be the residual water ice cap at the north pole. It is plausible that seasonal water ice, separate from the perennial ice cap, also acts as a major sink/source in this cycle, albeit limited to seasonal timescales. Springtime sublimation of frost and subsequent mixing of water vapor back into the atmosphere could explain observations where water vapor abundance increases before the north polar residual water ice cap is exposed (Smith, 2002). Determining the

extent and timing of seasonal water frost, as well as its relationship to changes in atmospheric water content, improves our understanding of the global water cycle.

The primary focus of this work is to investigate the global distribution of seasonal water ice for all times of year and its role in the global water cycle. We focus primarily on data acquired by the MGS TES bolometers. The TES visible/near-infrared and thermal infrared bolometers measured reflected and emitted radiance for more than three Mars years, from which albedo and temperature can be derived from. These measurements are well calibrated and were acquired systematically over all latitudes and all seasons. By mapping the geographical extent, timing, and impact of seasonal water frost on surface albedo, we can provide insight to the present martian climate.

Previous studies have mainly focused on the presence or absence of a water ice "annulus" along the periphery of the seasonal CO_2 cap during retreat in the springtime (Kieffer and Titus, 2001; Titus, 2005; Wagstaff *et al*., 2008; Appéré *et al*., 2011). Localized water frost in near-tropical southern latitudes (Carazzo *et al*., 2009), and pole-facing slopes between 45°S-50°N (Vincendon *et al*., 2010), have been investigated as well. Szwast *et al*. (2009) explored much of the same data presented here, however their focus was primarily on interannual surface albedo changes due to dust activity as well as mostly omitting temperature analysis. Another major difference between this study and Szwast *et al*. are the geographic regions of interest. We consider the global dataset but focus primarily on regions that host seasonal frost (mid-to-polar latitudes), whereas Szwast *et al*. focused primarily on albedo variations at near-tropical latitudes.

2.1.2 *Lander Observations of Frost*

In situ lander observations of martian surface conditions aid in understanding seasonal frosts. Viking Lander 2 (VL2) landed at 48°N, 135°E in Utopia Planitia and observed seasonal

surface ices for two Mars winters (Figure 2.1; Jones *et al.*, 1979; Svitek and Murray, 1990). On a seasonal basis, the VL2 site only hosted water frost because daytime temperatures were too high for seasonal CO_2 frost (Jones *et al.*, 1979). However, water ice was present because daily temperatures can remain at or below 200 K for a substantial fraction of a martian year (e.g., L_S = ~230-350° at VL2 site).

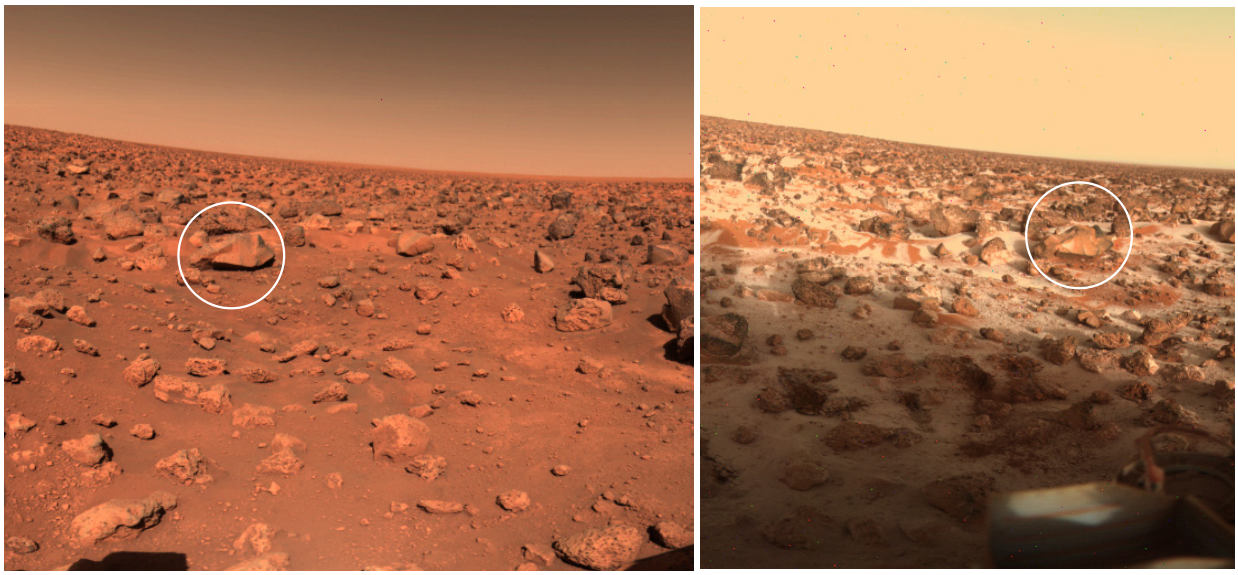

Figure 2.1. Images from Viking Lander 2 showing unfrosted (left) and frosted (right) surfaces in Utopia Planitia (48°N). The frosted image is from L_S = 279° (winter solstice) and is interpreted as seasonal water frost (Svitek and Murray, 1990). The images are capturing roughly the same scene, with the same rock (~1 m) circled in both images for reference.

Water ice exhibited a dynamic evolution while it was observed at the VL2 site (Svitek and Murray, 1990). Frost was initially restricted to shaded areas of the surface (e.g., shadows cast by boulders). Progressing through winter, daytime maximum surface temperatures remained below the water frost point, and frost was observed across most of the surface; i.e., almost continuous. During late winter and early spring, frost simultaneously sublimated and re-deposited in local cold traps, where temperatures were favorable. The dynamic nature and

tendency for water frost to migrate to stable locations resulted in discontinuous frost. This is observed at VL2 and can also be seen in high-resolution images (Figure 2.1). This heterogeneity is present during the frost's early and late seasonal appearances when daytime surface temperatures are too high for stable, continuous frost. Assuming some accumulation occurs throughout winter, water frost is likely thicker during late winter/early spring than in late autumn/early winter.

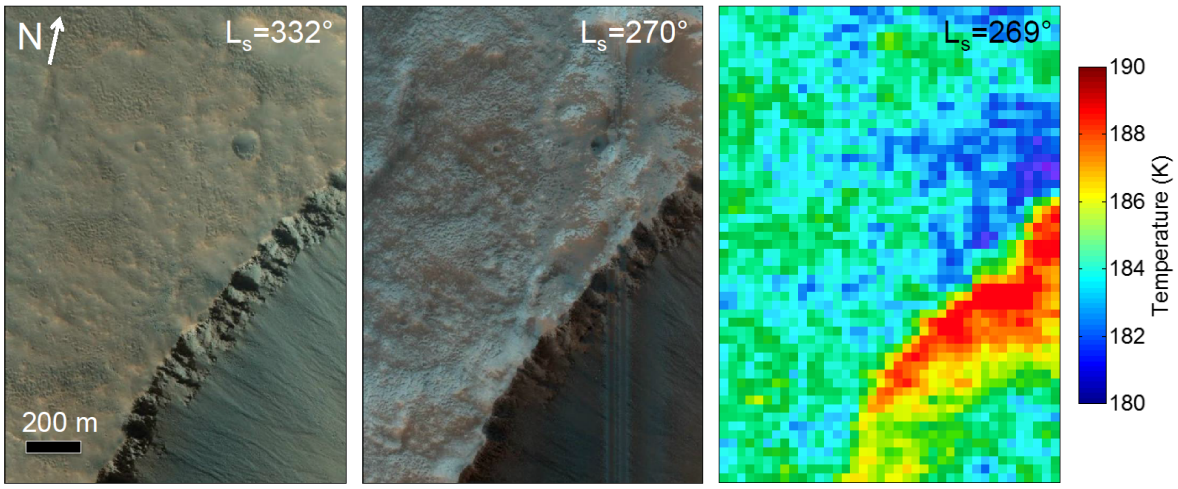

Figure 2.2. Example of seasonal water frost at 42.109°N, 312.031°E. High Resolution Imaging Science Experiment (HiRISE) images (left) ESP_032192_2225_COLOR (2 PM) and (middle) ESP_030847_2225_COLOR (2 PM) and corresponding Thermal Emission Imaging System (THEMIS) I07941019 (5 PM) smoothed brightness temperatures (right). Temperatures are consistent with the presence of water frost (and are too warm for the presence of CO_2 ice).

Based on observed atmospheric water vapor abundances from the Viking orbiters, Svitek and Murray (1990) suggest frost was tens to hundreds of microns thick (with thicker values representing late, less continuous patches of frost). TES column integrated water vapor measurements yield mean-annual abundances of ~12 pr-μm (Smith, 2002), which is consistent with Viking data, therefore water vapor is a plausible source for this frost. Our work does not

make an attempt to estimate frost thickness because the measured albedo can vary greatly due to other properties besides thickness (e.g., grain size).

The Phoenix Lander (PHX), which landed at 68°N, 234°E, observed the beginning of terrain frosting just before the mission ended at L_S ¬= ~150°. Comparable frost morphologies, thicknesses, and temperatures were observed at PHX, with respect to VL2 (Cull *et al*., 2010). Unfortunately, these were only the first appearances of seasonal water frost and the mission did not remain active for periods when more continuous surface frosts were present.

2.2 METHODS

2.2.1 *General Methodology*

In our study, it is necessary to distinguish between H_2O and CO_2 frosts on the martian surface. Surface temperature data can reliably identify surfaces where only water frost would be stable (<~200 K). These ices are also distinguishable via other techniques (e.g., near-infrared spectral absorptions; Carrozzo *et al*., 2009). However, we rely primarily on the TES dataset in this work because of its systematic, multi-annual, and global coverage. CO_2 frost exhibits a characteristic temperature near ~148 K because it is necessarily in equilibrium with the atmosphere. Surfaces at similar or lower temperatures may contain either frost type. For our purposes, due to mixing of multiple surface types in a single TES measurement (~3 x 6 km), and uncertainties in bolometric temperature retrievals, only surface frosts identified using TES data exhibiting temperatures >~170 K can be interpreted as water frost.

Our confidence in identifying water frost at lower temperatures (especially near the lower limit of 170 K) is substantially less than with interpretations made at higher temperatures. One reason for this is that there is observed mixing between the two ices, notably along the boundary of the retreating seasonal cap (Appere *et al*., 2011); i.e., there is no "sharp" H_2O/CO_2 ice

boundary. Sub-pixel mixing of ices and bare surfaces is also problematic. For example, it is possible for a TES pixel measuring 175 K to be composed of ~50% bare surface and ~50% CO_2 ices by area.

We cannot rule out the contribution of CO_2 ice in this temperature range (~170-180 K), especially as retreat of CO_2 ice can be heterogeneous at scales well below that of TES (Searls *et al*., 2010). However, at temperatures closer to 200 K (our upper limit for H_2O frost detection), it is unlikely that CO_2 covers a large fraction of the surface since this would greatly reduce the observed temperature. We also frame our interpretation based on published cap edge data (e.g., Piqueux *et al*., 2015b), in order to strengthen arguments for water frost in areas beyond the seasonal CO_2 cap edge.

In addition to temperature analysis, we also studied albedo and changes in albedo, relative to a zonally-averaged "frost-free" summer albedo (Figure 2.3). To derive these values, albedo was spatially binned and averaged over all Mars years studied, ~30° L_S after summer solstice (i.e., L_S = 120° in the north, L_S = 300° in the south; 1° L_S slice used per Mars year). This time was chosen to ensure minimum seasonal frost cover and relatively low atmospheric opacity (Smith, 2002). Averaged albedo ("frost free") was then subtracted from the entire albedo dataset to emphasize any seasonal changes in albedo.

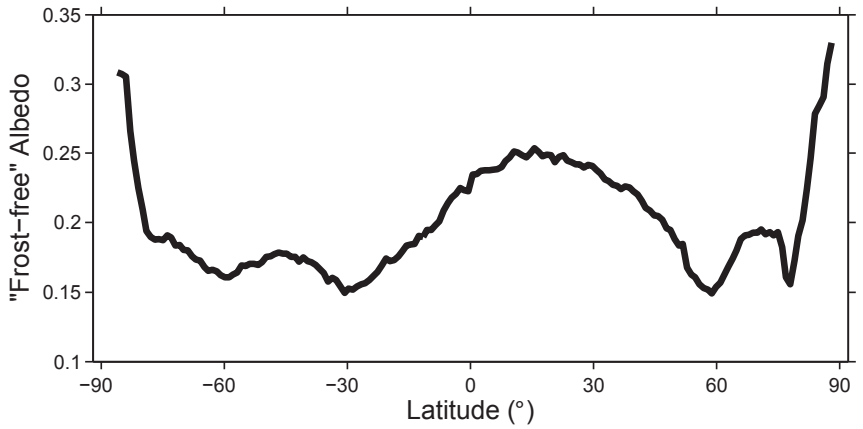

Figure 2.3. Estimate of zonally-averaged "frost-free" surface albedo from TES. These values were subtracted from albedo data to create change in albedo maps (e.g., Fig. 2.4). For details on calculating these values see section 2.4.2.

2.2.2 *TES Instrument Description*

A complete description of the TES instrument as built and instrument operations can be found in Christensen *et al*. (2001). MGS was operational in orbit around Mars from 1997 to 2006 with systematic TES mapping from a near-polar orbit at a fixed equatorial crossing local time of ~2 AM/PM beginning in March of 1999 (L_S = 107° of Mars Year (MY) 24, where the start of MY 0 is defined as April 24th, 1953; Piqueux *et al*., 2015a). TES consists of an interferometer spectrometer with co-aligned visible/near-infrared (0.3-2.7 μm) and thermal infrared (5.5-100 μm) bolometers. The TES focal plane consists of three cross-track and two along-track detectors with an instantaneous field of view of ~8.5 mrad, resulting in ~3 x 6 km sampling at nadir. The TES instrument uses a pointing mirror that allows for limited targeting capability, limb observations, emission phase function measurements, and periodic full aperture calibration observations.

The optical system consists of a single off-axis parabolic mirror operating at f/8. A reflecting resonant fork chopper, operating at 30 Hz, is used to separate the visible/near-IR and thermal channels.

The visible/near-infrared bolometer was calibrated using periodic observations of the internal calibration lamps and space. Lamp observations were acquired once daily and once weekly for the primary and redundant lamps, respectively. These data are corrected for lamp and instrument temperature. For each planet observation, the detector response is corrected for

variations with temperature and the measured bolometer signal (voltage) is converted to integrated calibrated radiance.

2.2.3 *TES Bolometer Data*

Data was retrieved via the Planetary Data System (PDS). After Christensen *et al*., (2001), the Lambert albedo AL, as acquired from the PDS, is calculated using the TES visible bolometer measured radiance R, the Sun-Mars distance D (in AU), the incidence angle i, and the solar irradiance at 1 AU integrated over the TES bolometer spectral response S using:

$$A_L = \frac{\pi R D^2}{S \cos(i)} \qquad (2.1)$$

The 1-σ precision of the visible bolometer calibrated radiance corresponds to a noise-equivalent delta reflectivity (NEΔR) of 0.00043 and is equivalent to an SNR (signal-to-noise ratio) of 2300 for a surface with unit reflectivity at average Mars insolation. The derived 1-σ variation in the zero-level radiance is ~3.75 × 10-6 W cm^{-2} sr^{-1} for all six detectors. For a typical martian surface (e.g., AL ~ 0.20, corresponding to a radiance of ~1.75 × 10-3 W cm^{-2} sr^{-1}), the 1-σ error in such a measurement is +/- 0.002 albedo. This is negligible relative to albedo differences between frost and bare soil (typically >0.05).

The thermal bolometer calibrated radiance is determined in a manner similar to the spectrometer radiance (Christensen *et al*., 2001). The weighted integrated radiance as a function of scene temperature is computed by convolving the relative spectral response of the bolometer with the blackbody calibration surface radiance. A lookup table of Planck radiance convolved with the instrument spectral response is used to convert integrated radiance to brightness temperature.

Inherent instrumental error of the thermal bolometer, as was the case with the visible bolometer, is negligible for our purposes (~1-2 K; Christensen, 2001). However, atmospheric effects can yield thermal bolometer brightness temperatures that deviate up to ~10 K or more relative to the actual surface kinetic temperature (e.g., Bandfield and Feldman, 2008;). For this reason, and the susceptibility to sub-pixel mixing, we do not interpret data exhibiting temperatures <170 K as water frost.

2.2.4 *Dataset Constraints and Binning Methodology*

MGS data relevant to this work extend from MY 24 to MY 28. The bolometer data were restricted from MY 24 (beginning at L_S = 104°) to the end of MY 27. MY 28 was omitted due to large gaps in nadir observations during that phase of the mission. To ensure high quality, data were restricted to emission angles of 0-20°, solar incidence angles of 0-80°, and local solar times of 1200-1600H.

Zonally-averaged albedo and temperature data were calculated for 1° latitude by 1° L_S bins, at all longitudes. We calculated zonal means for the following reasons:

1. The aim of this work is to investigate global climatological processes that have widespread influence across most longitudes for a given latitude and is likely apparent in zonally-averaged data. Examples include seasonal and perennial deposits of H_2O ice and CO_2 ice on the surface.
2. Previous derivations of atmospheric water abundance, dust and water ice opacity (e.g., Smith (2004) and Szwast *et al*. (2008) using TES; Toigo *et al*. (2013) using CRISM) as well as seasonal ice retreat (Wagstaff *et al*., 2008; Appéré *et al*., 2011) were displayed as zonal averages and this work may be more readily compared with these previous studies at first order.

3. The recession and growth of the seasonal cap in the northern hemisphere is roughly axially symmetric with minor longitudinal variations (Kieffer and Titus, 2001); although the same is not necessarily the case for the southern hemisphere seasonal cap (e.g., Hellas basin; Kieffer *et al*., 2000).

Longitudinally-resolved data were used from MY 26 to aid in validating our interpretation of the zonally-averaged data. Bolometric albedo and temperature data were retrieved from 35° to 90° latitude in both hemispheres and divided into larger 5° L_S increments to ensure enough data to populate most bins. Linear interpolation was performed for each 5° L_S bin to fill in gaps between orbit tracks. We calculated the change in albedo by the same approach as the zonally-averaged data (Section 2.1), using an interpolated summer map at the same times of year to estimate seasonal frost-free surface albedo.

2.3 RESULTS

2.3.1 *Overview of TES Bolometric Temperature and Albedo*

The multi-year TES bolometer data show that albedo and temperature variations occur both spatially and temporally (Fig. 2.4). Some latitudinal variations in albedo are constant in time and are due to the heterogeneity of the martian surface (e.g., relatively bright, dusty regions that dominate latitudes between ~0-30°N; see Fig. 2.3; Christensen *et al*., 2001). Other variations occur seasonally (e.g., surface frosts, aphelion water-ice cloud belt) or interannually (e.g., MY 25 global dust storm).

To better outline seasonal variations we have subtracted out our approximation of the martian "bare" surface, illuminating albedo changes (described in Section 2.1; Fig. 2.5). Equatorial regions experience small seasonal albedo changes; up to ~±0.05 (excluding global dust storm events; e.g., MY 25).

Large seasonal increases in planetary albedo (0.05-0.35) are restricted to latitudes poleward of ~45°, during spring and early summer (in either hemisphere), and increases in magnitude with increasing latitude. This albedo variation can be attributed largely to the seasonal CO_2 ice caps, which have been described in previous work (e.g., Kieffer *et al.*, 1977; 1992). The large variations in albedo and temperature at these latitudes repeat, showing similar patterns each year.

The relationship between temperature and corresponding albedo increases for specific latitudes shows clear trends (Fig. 2.6, 2.7). Significant albedo changes (>0.05) primarily occur at lower temperatures, <200 K during winter in both hemispheres. When temperatures initially drop below ~200 K during autumn in the northern polar latitudes, there is a corresponding increase in albedo that doesn't return to initial summertime values until the spring. The southern polar region does not exhibit this behavior, although increased albedo is observed in late winter/spring (Fig. 2.5).

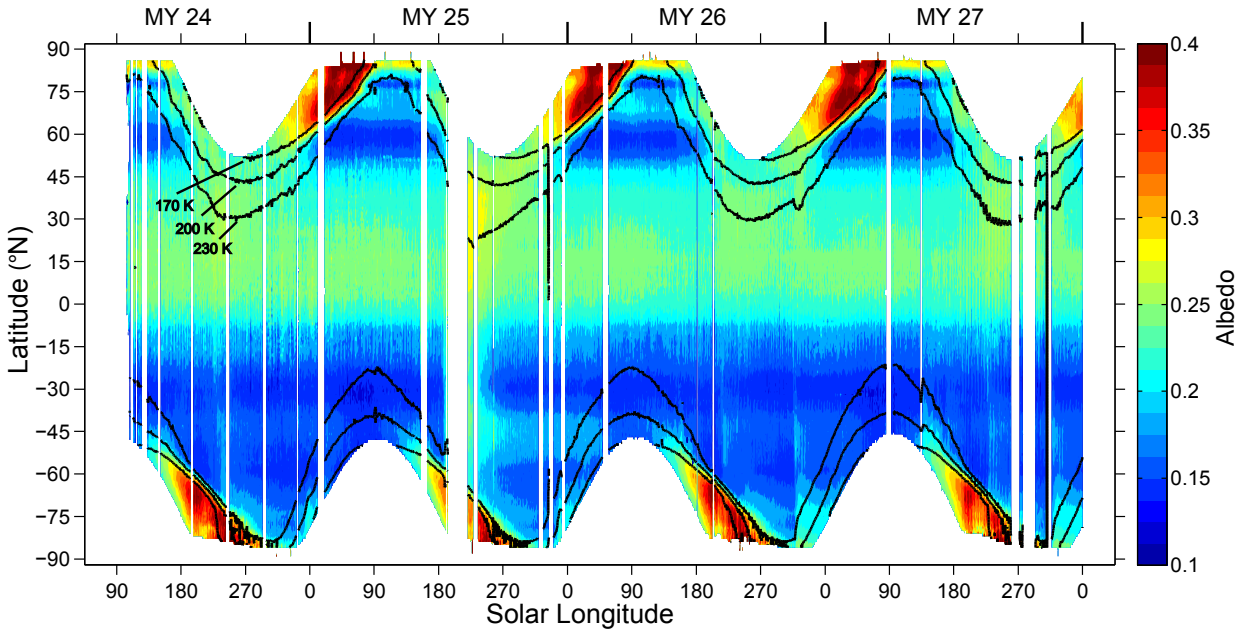

Figure 2.4. Zonally-averaged 2 PM TES color-shaded albedo and temperatures (three contours at 170, 200, and 230 K). Dominant features include seasonal polar caps, dust storms, and natural

variability in the martian surface albedo (e.g., more reflective northern hemisphere). Note the large gap in data in MY25 due to a global dust event. Color bar limits do not reflect the full range of the data.

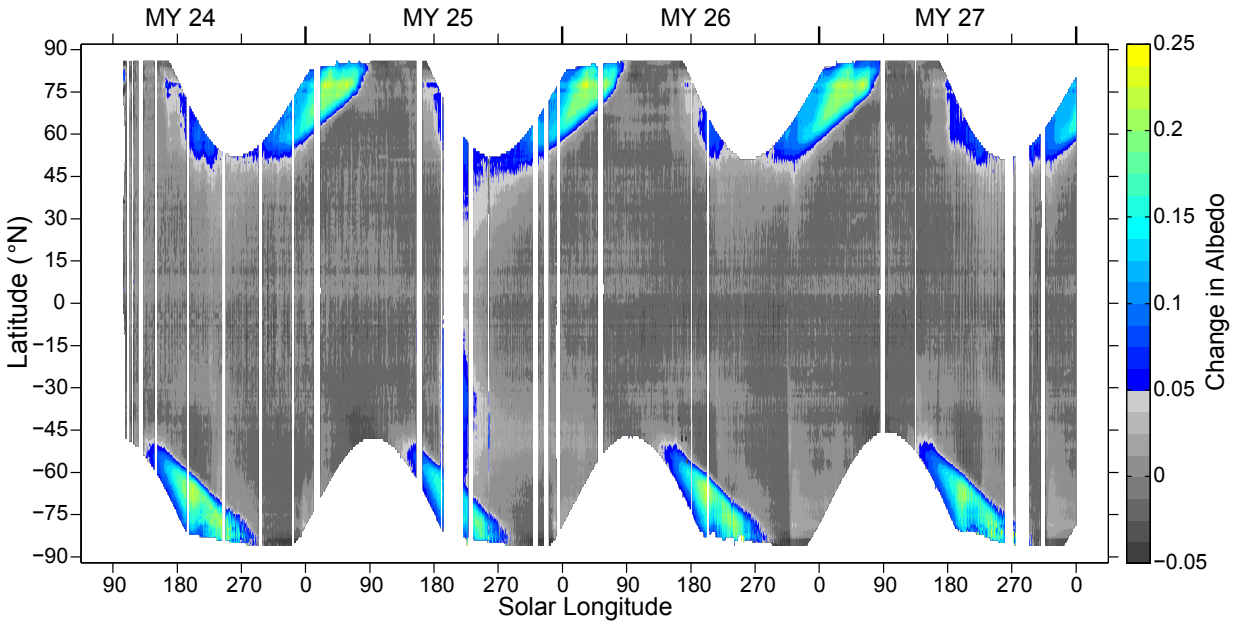

Figure 2.5. Zonally -averaged 2 PM TES color-shaded albedo change (relative to summer surface, see Section 2.1). Note the asymmetrical behavior in mid-to-high latitude albedo between the northern and southern hemispheres in late autumn. Also, note the general lack of interannual variations, with the MY 25 dust storm being most obvious.

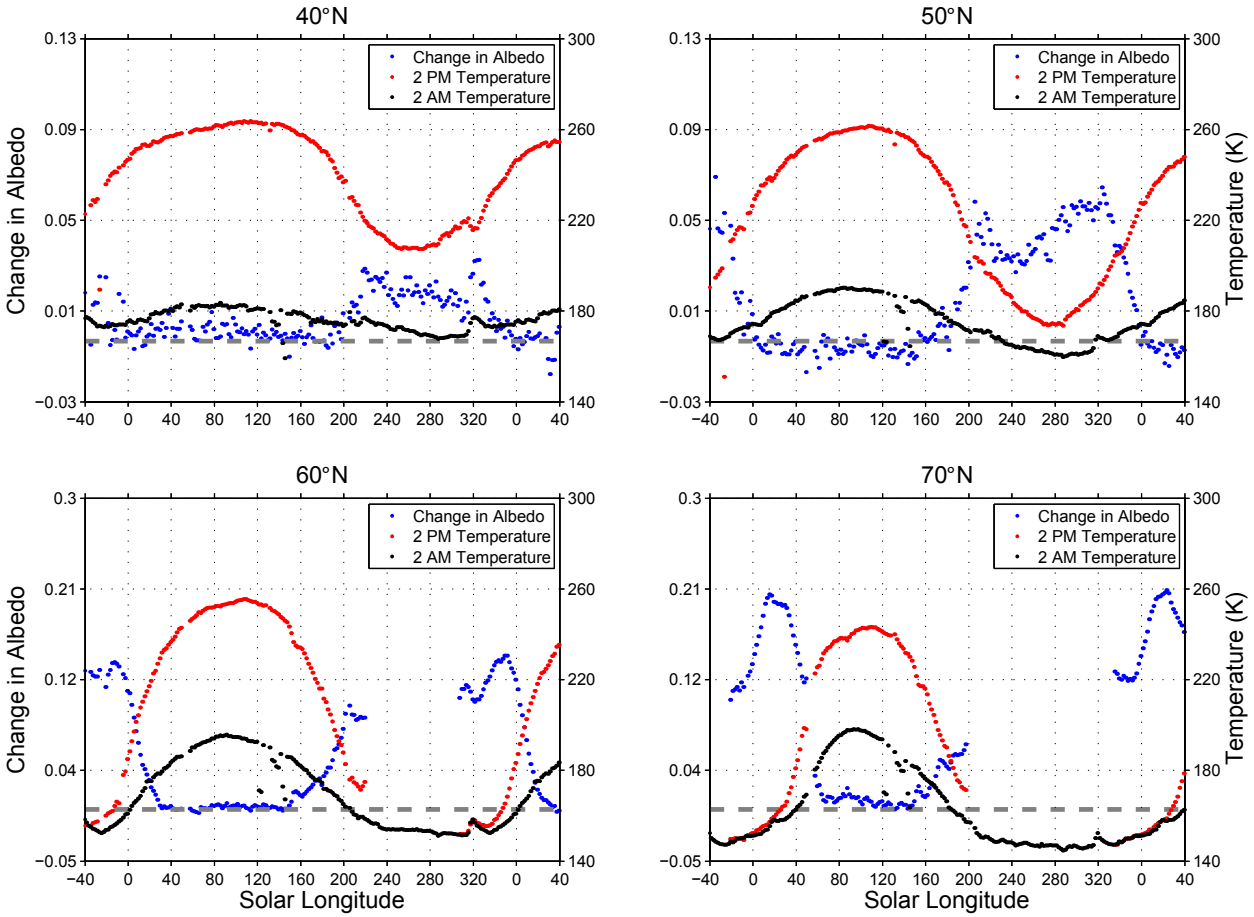

Figure 2.6. The behavior of zonally-averaged TES albedo and AM/PM temperature for 40°, 50°, 60°, and 70°N in MY 26. Data are re-binned in 3° L_S increments for clarity. Dashed gray line indicates zero change in albedo. As seen in Figures 2.4 and 2.5, the onset of albedo increase is earlier at higher latitudes and is consistent with water ice temperatures (too high for CO_2). 50°N and 70°N can be compared to the VL2 and PHX sites, respectively.

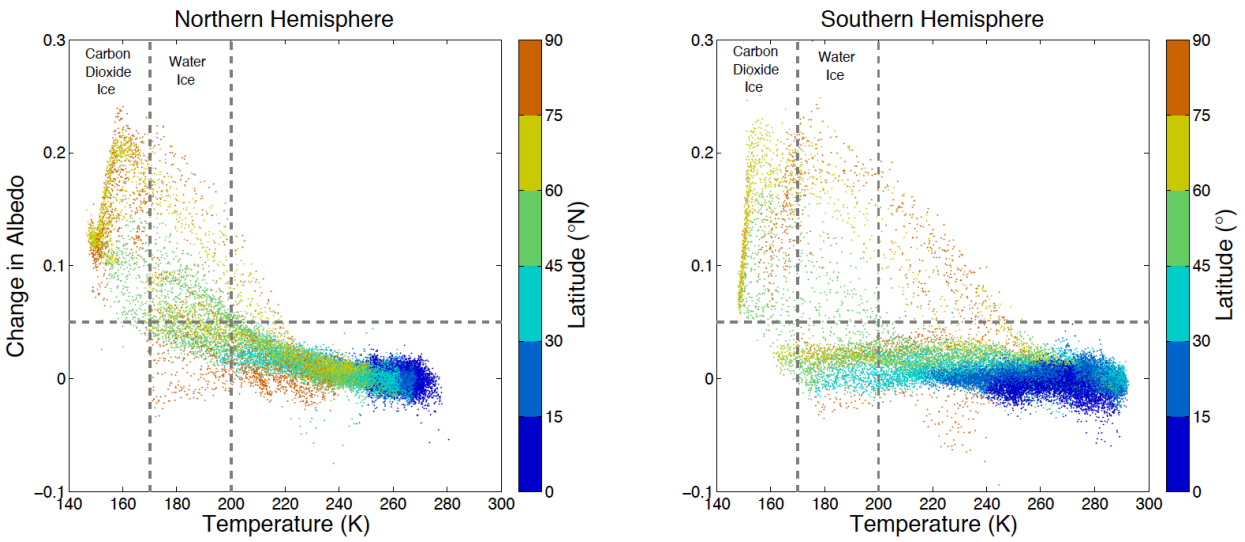

Figure 2.7. Scatter plots showing trends in MY 26 zonally-averaged TES albedo (change) and temperature. Dashed lines include interpretations of surface ices from this study. Colors indicate latitude. The largest albedo changes occur at an abrupt temperature, characteristic of CO_2 ice in equilibrium with the atmosphere (<170 K). Both hemispheres exhibit this abrupt behavior indicative of seasonal CO_2 ice. However, in the north, there is a negative slope at intermediate temperatures of ~170-200 K, with many observations falling in our criteria for water ice, suggesting extensive water frost. Scatter outside of these trends can be attributed to dust storms, clouds, and longitudinal variability (e.g., Hellas basin seasonal CO_2 ice).

2.3.2 *Atmospheric Effects on Albedo and Temperature*

In order to confidently identify surface frost it is necessary to rule out albedo changes due to atmospheric aerosols. To do this, we compare TES-derived albedo, daytime surface temperature, and climatology data (Smith, 2004; Fig. 2.8). The climatology data include TES-derived optical thicknesses of atmospheric aerosols (i.e., dust and water ice), as well as TES-derived atmospheric water vapor abundances.

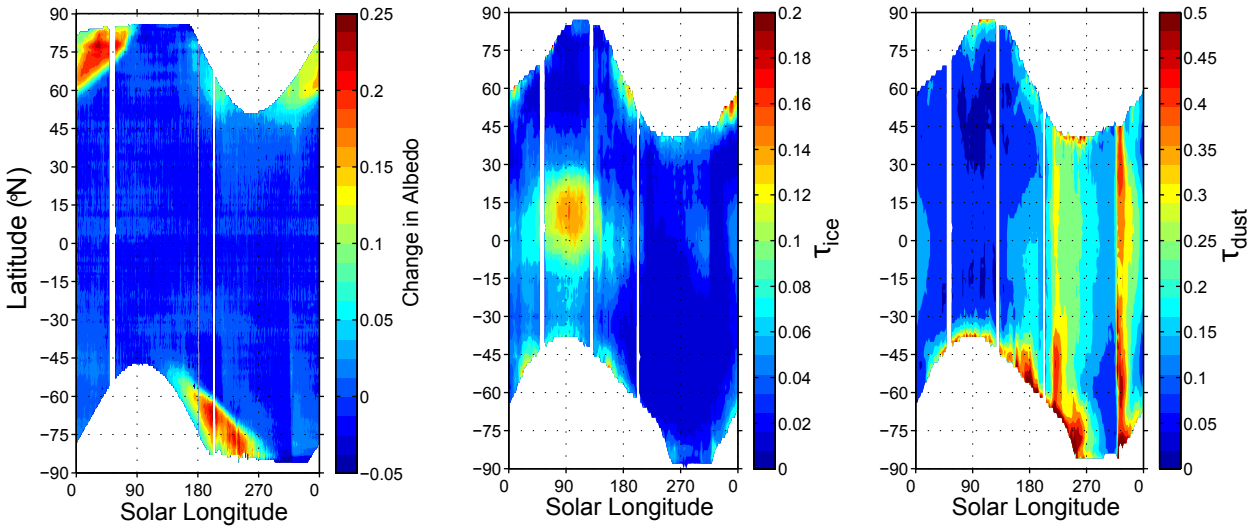

Figure 2.8. From left to right, MY 26 zonally-averaged TES change in albedo (Fig. 2.4), ice, and dust opacity (the latter two after from Smith (2004)). Note the lack of correlation between high ice/dust opacities and observed albedo changes. Both opacity datasets show heightened activity around the seasonal CO_2 cap (i.e., the polar hood) in both hemispheres whereas albedo increases, separate from seasonal CO_2 ice, are observed only in the northern hemisphere.

High atmospheric dust loadings can result in large increases in albedo (e.g., the MY 25 global dust storm), on the order of 0.10. The MY 25 global dust storm resulted in albedo changes that can last up to one Mars year (Smith, 2004), although the largest changes are restricted to certain regions and don't typically result in albedo changes >0.05 (Szwast *et al.*, 2006). More typical dust loadings have a small or negligible effect, resulting in albedo changes of <0.05 (e.g., MY 26 northern winter solstice dust storms). High dust loadings are relatively rare and are restricted to a limited time periods that are easy to identify and exclude from our analysis. In general, atmospheric dust has a greater effect on albedo than atmospheric water ice. This is because the highest dust opacities are about twice as large as water ice opacities observed by TES (Smith, 2004).

Elevated water ice opacities can lead to small increases in albedo (<0.05) relative to the albedo changes due to the presence of surface frosts (Fig. 2.8). For example, the aphelion water ice cloud belt (heightened tropical water ice cloud activity around $L_S \sim 90°$; Clancy *et al*., 1996) shows negligible changes (e.g., typically <0.03) in retrieved albedo even though it exhibits the highest water ice opacities measured by TES (Smith, 2004). Near both poles during their respective late autumn, the atmosphere appears to be similarly cloudy and dusty. As observed by TES, the north polar hood is generally dominated by dust and the south is dominated by water ice (Smith, 2004). However, TES-derived albedo changes show little correlation with the patterns of dust and water ice opacity and exhibit much larger variations than those associated with periods of high opacity in equatorial regions. Both polar regions, excluding regions containing perennial surface ices, have a zonally-averaged bare-ground albedo of ~0.2. This implies similar atmospheric aerosol loadings would affect planetary albedo in those regions equally (i.e., if such aerosols were the primary cause of albedo variation). Thus, the contribution from clouds is not primarily responsible for the observed albedo changes, consistent with previous work (e.g., Christensen, 1988).

TES albedo and climatology data are only available for regions exhibiting surface temperatures >~200 K because aerosol data derived from nadir observations can only be retrieved when there is significant temperature contrast between the surface and the atmosphere (Smith, 2004). Limb sounding data, from both TES and the Mars Climate Sounder aboard Mars Reconnaissance Orbiter, are not subject to this restriction. The behavior of the atmosphere during polar night generally agrees with the spatially and temporally limited nadir observations (Smith, 2004; Benson *et al*., 2010; 2011). For example, the MCS limb-derived aerosol abundances show values similar to those retrieved from the TES data, even over cold surfaces. Based on these

observations, outside of major inter-annual dust storms, larger seasonal albedo variations (>~0.05) can be attributed to the presence of seasonal surface frosts.

2.3.3 *Seasonal Water Frost – Northern Hemisphere*

Substantial albedo increases (0.05-0.35) combined with temperatures between 170-200 K support the presence of extensive surface water frost in the northern polar and mid latitudes, most notably during the autumn, winter and spring (L_S = ~160-90°; Fig. 2.5). Northern hemisphere water frost appears near the pole prior to the appearance of the CO_2 seasonal cap (L_S = 160°) and lasts for a substantial period of time (~100 sols), including regions where seasonal CO_2 frost is not present (e.g., VL2 at 48°N; Fig. 2.1b, 2.5). The duration of stable frost increases with latitude (e.g., analogous to the seasonal CO_2 cap).

We can estimate the time which water frost is present by the onset of albedo increases that fall outside CO_2 frost temperatures. By this method, H_2O frost precedes CO_2 frost by ~10-20° L_S in the northern hemisphere. Similarly, H_2O frost appears to outlast CO_2 frost ¬in the northern hemisphere (increasing poleward).

The longitudinally-resolved data (Fig. 2.9a) is consistent with the advance of water frost in late autumn is asymmetric about the pole, with the boundary varying by ~10° latitude. Also, both zonally-averaged data (Fig. 2.5) and longitudinally-resolved data (Fig. 2.9a) support the presence of a water ice annulus throughout the spring season. In the latter dataset, the annulus spans all longitudes and varies between ~5-8° in latitude during retreat of the seasonal CO_2 ice cap (L_S = ~0-90°).

It is difficult to place an exact latitudinal lower limit on seasonal water frost in the northern hemisphere with TES data. The equatorward boundary is not sharp and extends over a range of latitudes (Fig. 2.9a). Because surface temperatures can be heterogeneous for a given

martian surface (e.g., due to slopes, shadows cast by local topography, variation in bare-surface albedo and thermal inertia, etc.), a sharp boundary is not expected. We approximate an equatorward extent of ~40°N, based on the observed seasonal temperature and albedo trends (Fig. 2.5, 2.6, 2.9a).

There are other mechanisms that may obscure the extent of seasonal frosts in TES data. For example, dust activity causes a lack of albedo contrast during the maximum extent of surface water frost in the northern hemisphere (approximately winter solstice). TES data show atmospheric dust decreasing the observed planetary albedo over icy surfaces. Global dust opacities are highest during northern winter, and appear to decrease the observed TES albedo, by up to 0.10. This affects regions that showed frost cover in late autumn, essentially masking the presence of ice. However, the estimated effect is an upper limit as the south experiences the same (if not more severe) dust activity and seasonal cap retreat appears largely unobscured by the atmosphere.

(a)

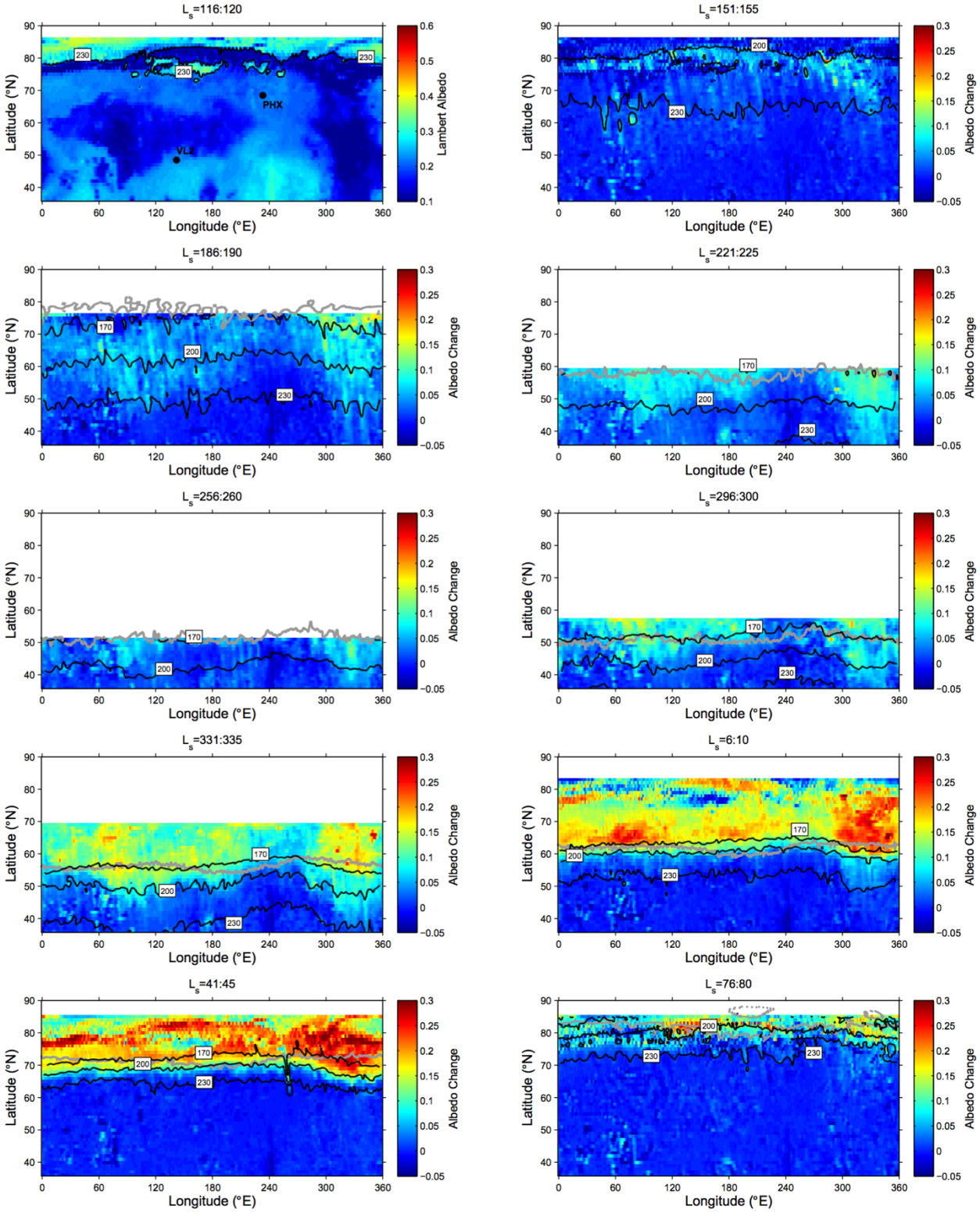
L_s=116:120
L_s=151:155
L_s=186:190
L_s=221:225
L_s=256:260
L_s=296:300
L_s=331:335
L_s=6:10
L_s=41:45
L_s=76:80
Latitude (°N)
Longitude (°E)
Lambert Albedo
Albedo Change
PHX
VL2
170
200
230

(b)

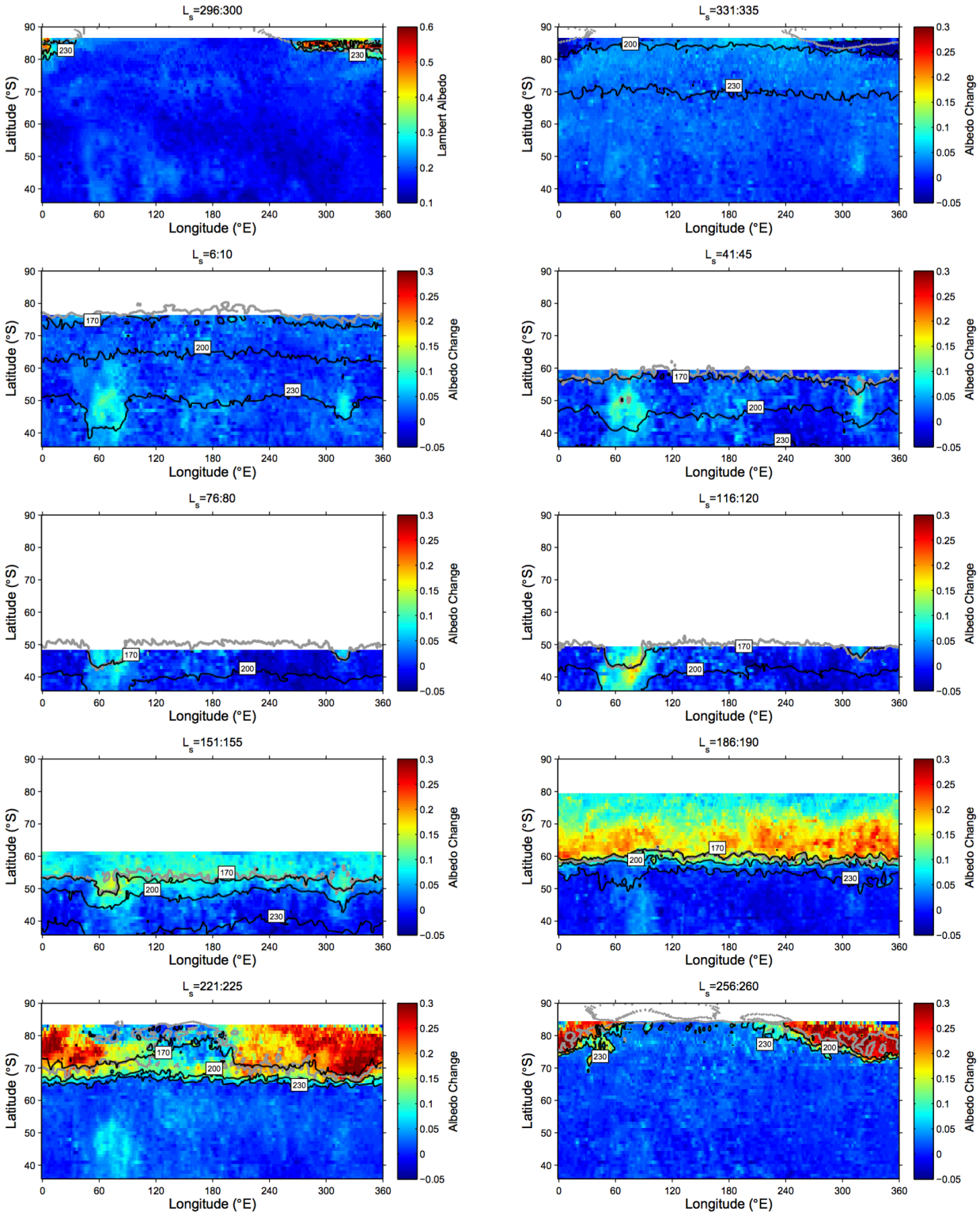
L_s=296:300
L_s=331:335
L_s=6:10
L_s=41:45
L_s=76:80
L_s=116:120
L_s=151:155
L_s=186:190
L_s=221:225
L_s=256:260
Latitude (°S)
Longitude (°E)
Lambert Albedo
Albedo Change
170
200
230

Figure 2.9. Longitudinally-resolved TES daytime bolometric albedo change, temperature (black contours at 170, 200 and 230 K), and derived seasonal CO_2 cap edges (grey; Piqueux *et al*., 2015b), all for MY 26. Maps extend from 35° to the pole for both (a) northern and (b) southern hemispheres. The respective hemispheric pole is at the top in all subfigures. The top left panel in each figure represents the summertime "frost-free" reference albedo map which is subtracted from subsequent panels. Each panel represents a 5° L_S period and are separated in 35° L_S intervals. Cap edge data was stored in 10° L_S bins, so the closest overlapping data was used for each figure (e.g., the cap edge data for 220-230° L_S was plotted with our data from 221-225° L_S). Note the similarities in the behavior of seasonal cap retreat and the appearance of water ice "annuli" in both hemispheres with the best examples at L_S ~10°, 45° (north) and L_S ~155°, 190° (south).

2.3.4 *Seasonal Water Frost – Southern Hemisphere*

The southern hemisphere shows similar annual temperature trends when compared to the north, consistent with the presence of water frost in southern autumn, winter and spring, or L_S = ~0-270°. However, during autumn and most of winter (L_S = ~0-170°), there are no albedo changes associated with water frost temperatures, in stark contrast to the northern hemisphere. In spring, zonally-averaged TES data (Fig. 2.4, 2.5, 2.7) show significantly higher albedo (>0.05) and temperatures well above the range of CO_2 ice in southern spring, suggesting the presence of water frost.

Zonally-averaged data are difficult to interpret because seasonal CO_2 ice forms at lower latitudes in the southern hemisphere (e.g., Hellas basin). Thus, averaging may produce ambiguous results due to latitudinal mixing of CO_2-ice-covered and non-CO_2-ice-covered surfaces. Longitudinally-resolved TES albedo and temperature data help eliminate this ambiguity (Fig. 2.9b). We observe that winter and spring albedo changes are less symmetric about the south pole than the north, which is due, in part, to Hellas basin (see Fig. 2.9b, ~35-55°S, 50-100°E).

The basin experiences persistent cloud cover (in addition to seasonal frost) which is evident in its typically heightened albedo from autumn to spring. Thus, zonally-averaged data are less reliable at those latitudes.

The data are consistent with a water ice annulus during southern spring (see L_S = ~180° in Fig. 2.9b). Compared to the annulus identified in the north, the southern annulus appears narrower, varying between ~2-5° in latitudinal extent (compared to ~5-8° in the north) and develops later in the respective winter season (occurring ~40° L_S later in the south). As was the case in the north, the expected water frost boundary appears diffuse. Using longitudinally-resolved data and excluding large basins we place a lower latitudinal limit of ~50°S, which is consistent with less extensive water frost in the south.

2.4 DISCUSSION

2.4.1 *Comparison of Northern and Southern Hemisphere Observations*

The northern polar region exhibits surface water frosts as temperatures decrease in autumn, whereas the south shows little evidence for water frost despite similar surface temperature trends (Fig. 2.5, 2.7). A potential explanation for this hemispherical asymmetry involves the disparity in atmospheric water vapor abundance between the two hemispheres during their respective autumn seasons. On a mean-annual basis, the northern hemisphere column abundance of water in the atmosphere is ~13 pr-μm whereas the average in the south is ~7.5 pr-μm (Smith, 2004). To estimate the corresponding frost point temperature at the surface for a given atmospheric water abundance, we follow the methodology of Schorghofer and Aharonson (2005). This approach assumes a well-mixed atmosphere where the partial pressure of water vapor in the atmosphere is proportional to the total CO_2 pressure, which follows hydrostatic equilibrium. The main unknowns are condensation height and column abundance of

water vapor, of which observational constraints exist only for frost-free surfaces (Smith, 2002). The corresponding mean-annual frost point temperatures, for the north and south, are ~198 K and ~194 K, respectively.

Annually-averaged values can be somewhat deceiving because atmospheric water abundances vary widely through the year, exhibiting seasonal cycles (Fig. 2.10). The data show a trend, prominent in both hemispheres, of decreasing atmospheric water content during summer and reaching minima around autumnal equinox in the north (L_S = ~180°) and mid-autumn in the south (L_S = ~45°). The difference in timing suggests that the surface in the north begins cold-trapping water in early autumn (described in Section 3.3), whereas seasonal water frost occurs later in the south, when albedo measurements are prevented by the polar night. The minima occur at ~8 pr-μm in the north (frost point = ~196 K) and ~3 pr-μm in the south (frost point = ~187 K). However, the difference between hemispheres is difficult to explain based on temperatures, column water vapor abundances, and the resulting predicted frost points. Much of southern hemisphere at temperatures below expected frost points (<190 K) do not show evidence of frost (Fig. 2.5, 2.7, 2.9).

In addition to the differences in ice stability temperatures, there are several other explanations for the hemispheric asymmetry in water frost occurrence. Recent work has shown that at the PHX site the atmosphere was not well mixed with respect to water vapor (a key assumption in our estimate of the frost point; Tamppari, *et al.*, 2010). If vapor was typically restricted to the lower atmosphere its number density would be higher at the surface, resulting in warmer frost point temperatures. TES data suggest that water frost occurs at temperatures >200 K (Fig. 2.7, 2.9), but cannot be confirmed due to sub-pixel mixing and uncertainty in estimated surface temperatures (see Section 2.2).

Another possible factor is the argument of perihelion and the effect it has on pronouncing differences between the hemispheres, especially concerning maximum surface temperatures. Since perihelion occurs before southern summer it would be plausible that the surface is too warm to host H_2O frost before polar night. However, this isn't supported by the data because the surface temperatures drop below 200 K without a persistent increase in albedo (as we see in the north; Fig. 2.4). Perhaps, the lack of a perennial H_2O cap in the south compared to the north leads to insufficient sublimation in order to humidify the atmosphere to where we see similar trends in seasonal frost. Since the timing of perihelion changes over geologic time, different epochs of Mars could have experienced markedly different seasonal frosting.

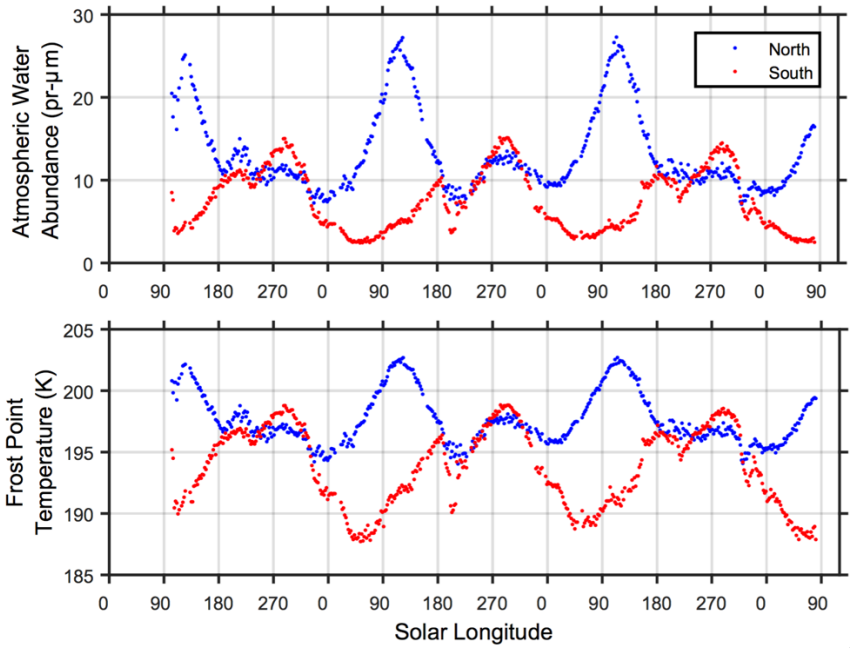

Figure 2.10. Zonally-averaged TES atmospheric water abundance data after Smith *et al.* (2004), covering MY 24-27 and split into hemispheric averages at 2° L_S increments. The top panel displays the data in column density (pr-µm) and the lower panel displays data as frost point temperature, estimated from column density after Schorghofer and Aharonson (2005), assuming a condensation height equal to twice the scale height (22 km and 11 km, respectively). Note the large differences in maximum and minimum values between the hemispheres.

Lastly, it is also possible that the vertical distribution of water vapor in the southern hemisphere behaves differently than the north due to a lack of seasonal water frost. If water frost enhances the lower atmosphere vapor density, preferentially, then the absence of water frost in the south could result in a well-mixed atmosphere, which is commonly assumed to be the case (Schorghofer and Aharonson, 2005). Because the surface does not effectively trap water (due to lower frost points in the south), the vapor remains in the atmosphere where it is mixed. Regardless of the exact mechanism, we observe a stark contrast in seasonal water frost behavior between the two hemispheres.

2.4.2 *Comparison of TES and Lander Observations*

As observed by VL2, seasonal water frost occurs at 48°N, beginning at L_S = ~230° (Svitek and Murray, 1990). Zonally-averaged TES data show an increase in albedo beginning at L_S = ~200° at 48°N (Fig. 2.5, 2.6). This is substantially earlier than what was observed at VL2. Longitudinally-resolved TES data suggest that the first appearances of daytime frost at 48°N occur at other longitudes which explains the apparent disagreement in timing (Fig. 2.9a; see Section 3.3). These data also agree well in timing with the observed frost conditions at VL2 (Fig. 2.11).

Seasonal water frost deposited in the shadows of rocks was observed at the PHX site (68°N), beginning at L_S = 157°. However, observations ended before the onset of widespread seasonal H_2O and CO_2 frost (Cull *et al*., 2010). Using CRISM data, Cull *et al* (2010), identified seasonal water frost, on level, sunlit surfaces, after L_S = 160° around the PHX site. TES data show increases in albedo beginning L_S = ~160° at 68°N (Fig. 2.5, 2.6). Similar arguments for frost timings at the VL2 site can be made for PHX and longitudinal variation in the onset of frosting is smaller at higher latitudes.

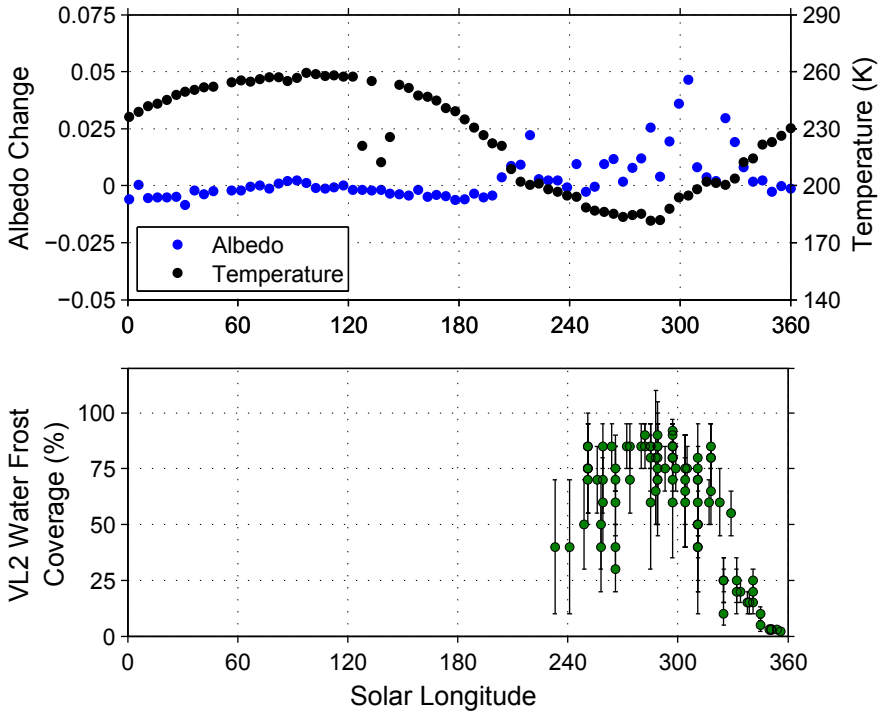

Figure 2.11. (top) MY 26 TES 2 PM albedo change (relative to an absolute surface albedo of ~0.25) and temperatures from longitudinally-resolved data (Fig. 2.9a). Here, we show data for a 1° by 1° bin encompassing the VL2 site (48°N, 135°E). (bottom) Observations at VL2 site of surface water frost coverage during winter. Re-plotted data from Svitek and Murray, (1990). The agreement between these observations is pretty good, however albedo changes are relatively small compared to higher latitudes and looks less "clear" than zonally-averaged data at 50°N (Fig. 2.6).

2.4.3 *Implications of Widespread Seasonal Water Frost*

Global Transport

In the north, extensive seasonal H_2O frost appears to extend beyond the seasonal CO_2 cap, both spatially (~5-10° latitude) and temporally (~20-100° L_S). This cycling of water at the surface may have a significant influence on the martian climate. Formation of surface frost and subsequent mixing of vapor back into the atmosphere could play an important role in the global water cycle, especially while the perennial water ice caps are covered by seasonal CO_2 ice. Our

results suggest that the martian surface acts as both a significant sink and source for water, with extensive frost forming and disappearing each year.

Water vapor abundance in the northern hemisphere diminishes by about 50% between L_S = ~140°-240° and has been interpreted to be due to transport to the southern hemisphere and non-atmospheric sinks (Fig. 2.10; Smith, 2002; Smith *et al*., 2004). However, southward vapor transport is relatively weak due to the asymmetrical strength of Hadley circulation on Mars, the primary means for meridional transport (Richardson and Wilson, 2002). Our results suggest that, rather than being transported to the southern hemisphere, a significant fraction of atmospheric water vapor is deposited onto the surface, beginning at L_S = ~140° at high latitudes, and advancing equatorward with time. During spring, Smith (2002) identified a rise in atmospheric water vapor prior to the exposure of the residual water ice cap in the north. Surface water frost (including both the annulus and presumably mixed ices in the seasonal cap) could act as a source for this early increase of atmospheric water vapor. In conclusion, not only is southward water vapor transport weakened by south-to-north-favored Hadley circulation (Richardson and Wilson, 2002), but is also weakened by removal of water vapor from the atmosphere via frost deposition.

Water Ice Annulus

In the northern hemisphere water frost is a known component during the spring retreat of seasonal ices (Kieffer and Titus, 2001; Titus, 2005; Wagstaff *et al*., 2008; Appéré *et al*., 2011), and is consistent with the data discussed here. Although there is a physical basis for expecting a water annulus in the southern hemisphere, previous work has not identified a feature, as is observed in the north (Titus, 2005). This observation is consistent with asymmetric water vapor abundances between the two hemispheres (Smith, 2004) and may be due to efficient transport of

water from the southern hemisphere to the northern hemisphere during southern winter (Richardson and Wilson, 2002).

Longitudinally-resolved southern hemisphere data are consistent with a water ice annulus (Fig. 2.9b). This may be due to our interpolation of the data or subpixel mixing but at certain times the retreating southern cap edge resembles the appearance of the northern cap edge during northern spring (e.g., L_S ~190° in the south, L_S ~10° in the north). Vincendon *et al*. (2010) found seasonal water frost occurs on pole-facing slopes as low as 13° latitude in the south and 32° latitude in the north. Although their study didn't extend beyond 50° latitude in either hemisphere, their results support the presence of water frost in the south.

We also included derived seasonal CO_2 cap edge data from Piqueux *et al*. (2015b) to aid in our interpretation (see grey data in Fig. 2.9a,b). In general, the derived cap edge traces the 170 K contour, with better agreement in the south. One explanation for areas where these differ could be due to binning (see Fig. 2.9 caption). The displayed cap edges reinforce the notion that there are significant changes in albedo that span large areas outside of complete seasonal CO_2 ice cover.

The source of vapor to generate a water annulus in the south is uncertain. Water frost has been identified (Vincendon *et al*., 2010), but is it abundant enough to produce features we observe in the north? One scenario we envision is that water frost is preferentially deposited during autumn into large southern basins (e.g., Hellas, Argyre), perhaps analogous to icy seasonal outliers in northern polar regions (Cantor *et al*., 2010). This could explain the lack of a zonal frost albedo signature in autumn in the southern hemisphere. During southern spring, the water frost is sublimated from the basins and is available to produce a north-like annulus. Additionally, the "Houben" effect (Houben *et al*., 1997) could enhance the supply of water vapor

to the cap edge during retreat by re-circulating water that was deposited with and cold-trapped by the seasonal CO_2 cap (Titus, 2005). Further analysis of higher resolution thermal and visible data may resolve the nature of water frost during southern spring.

Ground Ice Stability

The seasonal presence of surface water frost can enhance the stability of ground ice, which is sensitive to surface temperature and humidity (e.g., Mellon and Jakosky, 1993). Neutron spectroscopy suggests near-surface ground ice is prevalent poleward of ~45° in both hemispheres (Feldman *et al*., 2002; Bandfield and Feldman, 2008), which agrees well with theory (Leighton and Murray, 1966; Mellon and Jakosky, 1993; Mellon *et al*., 2004). Variation in albedo on seasonal timescales can greatly affect surface temperatures, which will propagate to the subsurface. Lowering of surface temperatures due to seasonal increases in albedo can extend the boundary of stable ground ice equatorward.

In addition to albedo, surface water frost can also increase the near-surface water vapor density above what is inferred from orbit. During the periods that surface frost is present, the surface is cold and TES atmospheric water data are not available. During late winter/early spring the surface water frost will sublimate and re-deposit during the daytime (as seen at VL2) until it is completely removed. During this period vapor density at the surface may increase beyond what is predicted in an atmosphere-only scenario, due to a local near-surface source of vapor. As a result, the effective mean-annual surface vapor density could be substantially higher than what is traditionally inferred from column measurements (e.g., Mellon *et al*., 2004).

To illustrate this in an idealized example we consider a 10 μm layer of water frost that is sublimated and mixed in the lower 1 km of atmosphere (i.e., effective condensation height of 1 km; this is a plausible diurnal mixing height for water after Tamppari *et al*., 2010). Following the

methodology of Schorghofer and Aharonson, 2005, and with a new condensation height of 1 km, we calculate a partial pressure at the surface of ~1.0 Pa which corresponds to a frost point temperature of ~212 K. This value is higher than what is predicted when assuming a more typical condensation height (e.g., ~2 × scale height or ~22 km). A frost point of 212 K is equivalent to a column density of ~96 pr-μm, assuming a condensation height of 22 km. This would fall near the maximum column abundance measured and is an example of how the vertical distribution of water vapor can result in different partial pressures at the surface. This effect could significantly affect ice stability (Mellon *et al*., 2004), though it strongly depends on the mass of water sublimated, the height to which mixing occurs, the atmospheric temperature profile, and the mixing timescale.

Seasonal water frost would promote ground ice stability and may considerably increase its geographical extent. This could help explain recent observations of impact craters that expose near-surface, putatively unstable, ground ice (Byrne *et al*., 2009; Dundas *et al*., 2014). Further modeling is required to quantify the effects of seasonal surface water ice on the permafrost subsurface of Mars, and determine their significance.

2.5 CONCLUSIONS

Multi-year TES planetary albedo and temperature data show a variety of dynamic processes, and can provide insight into the global climate of Mars. This work has documented our interpretation of the spatial and temporal extent of seasonal water frost on Mars. We argue that extensive deposits of surface water frost are present throughout autumn, winter and early spring in the northern hemisphere of Mars. When sublimated, this water frost layer may act as a substantial source in addition to the north polar residual cap.

We see less compelling evidence for seasonal water frost in the southern hemisphere except for a narrow window during retreat of the seasonal cap (L_S ~180°). This is similar to, though less extensive than the annulus in the north. This can be explained by the lower atmospheric water abundance in the south, though, other factors, such as differences in the vertical distribution of atmospheric water vapor between the two hemispheres, may also play a role.

The hemispheric asymmetry in seasonal water frost likely reflects an asymmetry in the global water cycle. From a different perspective, though, it seems that the occurrence of water frost may perpetuate this asymmetry. Assuming water frost is atmospherically derived, the production of frost removes water vapor from being transported southward, which is already impeded due to topography (Richardson and Wilson, 2002). This mechanism is expected to be less effective in the south, due to the lack of water frost, therefore enhancing net transport to the northern hemisphere. How seasonal frost cycles vary with Mars' orbital variations may be important for understanding past and future climates.

Lastly, water vapor may be enhanced in the lower atmosphere during seasonal sublimation. This additional source of vapor at the base of the atmosphere could significantly affect the mean-annual vapor density at the surface, which would stabilize ground ice at lower latitudes than currently predicted.

Chapter 3. ON THE ICY EDGE AT LOUTH AND KOROLEV CRATERS

Published in the journal Icarus
Bapst, J., Byrne, S., Brown, A.J., 2017. On the icy edge at Louth and Korolev craters. Icarus. doi:10.1016/j.icarus.2017.10.004

3.1 INTRODUCTION

The history and evolution of water on Mars, from evidence of flowing liquid water in the deep past, to the present-day state of kilometer-thick deposits of water ice at the poles, is largely uncertain. Throughout its history, Mars has undergone cyclical changes in its orbital elements (Laskar *et al.*, 2004). These changes result in a redistribution of sunlight about the martian surface, affecting surface temperatures. Water ice is extremely sensitive to these changes due to the Clausius-Clapeyron relationship, i.e., the nonlinear relationship between temperature and saturation vapor pressure of water.

Evidence supporting climate change and the redistribution of water ice in Mars' recent past (~100 Ma) includes, but is not limited to, the polar layered deposits (Milkovich and Head, 2005), viscous flow features (Milliken *et al.*, 2003), lobate debris aprons (Pierce and Crown, 2003; Holt *et al.*, 2008), dissected mantle deposits (Mustard *et al.*, 2001), latitude-dependent topographic statistics (Kreslavsky and Head 2000, 2002), tropical mountain glaciers (Head and Marchant, 2003; Forget *et al.*, 2006), expanded craters in Arcadia Planitia (Viola *et al.*, 2015), and extensive subsurface ice in Arcadia Planitia (Bramson *et al.*, 2015), and Utopia Planitia (Stuurman *et al.*, 2016). Evidence for more recent climate change includes the location and depth of ice-exposing fresh impact craters (Byrne *et al.*, 2009; Dundas *et al.*, 2014).

Although these discoveries are providing insight into previous climate episodes, fundamental questions remain unanswered. One unknown is the present-day mass balance of the north polar residual cap (NPRC), which is composed almost entirely of water ice. The NPRC represents the most recent layer of the north polar layered deposits (NPLD), and is in direct contact with the atmosphere. The kilometers of water ice in the NPLD likely represent a history of Mars climate (Squyers, 1979; Toon *et al*., 1980; Milkovich and Head, 2005; Byrne, 2009), while the NPRC reflects the present. It is unknown what the current mass balance of this cap is (Byrne, 2009). Observations of large-grained water ice exposed at the surface of the cap suggest a state of retreat (Langevin, 2005). However, Brown *et al.* (2016) have shown that the NPRC experiences both periods of ablation and accumulation. Specifically, the authors report an apparent transition from ablation to accumulation at Gemini Lingula at L_S~120°. They report that the mode flip is latitude dependent, with changes from ablation to accumulation earlier for regions closer to the pole, and later for regions away from the pole. Lastly, impact crater statistics suggest fast resurfacing of the residual cap, where craters are infilled on the order of 10^3 years (Tanaka, 2005; Banks *et al.*, 2010; Landis *et al.*, 2015).

The focus of this work concerns water ice outliers that sit within large impact craters in the northern plains of Mars. These outliers are similar to the polar deposits in surface texture (Brown *et al.*, 2008), thermal properties (Armstrong *et al.*, 2005), and the presence of layered water ice deposits (Conway *et al*., 2012; Brothers *et al*., 2015), yet some are located 100's of km equatorward of the perennial cap. There have been 11 craters identified poleward of 70°N that host exposed water ice mounds (Conway *et al.*, 2012). Due to their location, these ice mounds represent the warmest perennial surface ice on Mars, which makes them potentially sensitive to climate change. We focus on two of these deposits within Louth and Korolev craters.

The smallest, and most-equatorward of these water-ice mounds is found in Louth crater (Fig. 3.1a). Louth is a 36 km diameter crater located at 70.2°N, 103.2°E and hosts an ice mound ~10 km diameter, and up to ~250 m thick. Previous work characterized the Louth ice deposit in terms of surface texture, composition, and morphology (Brown *et al.*, 2008). These observations were interpreted as consistent with a state of net ablation. We conduct high-resolution image analysis to constrain interannual changes along the boundary of the ice mound. We also employ a model to estimate the seasonal and annual mass balance at Louth. Lastly, we compare the results of our modeling to a companion paper (Brown *et al.*, this issue) who map seasonal accumulation/ablation at Louth using near-infrared spectroscopy. Observations like these can aid in constraining the range of acceptable mass balance models for Louth.

The largest ice mound is found in the 83 km diameter Korolev impact crater (72.8°N, 164.5°E) which hosts a ~60 km diameter mound up to 2 km in thickness (Fig. 3.1b; Conway *et al.*, 2012; Brothers *et al.*, 2015). Because Korolev is 2.6° poleward of Louth we expect less ablation/greater accumulation compared to Louth. No image analysis is performed for Korolev, but we do use the larger ice mound to constrain thermophysical properties used as inputs in our model. Any changes in mass occurring at these mounds today must be balanced by other reservoirs (e.g., NPRC, mid-latitude ground ice), and so in estimating this value we provide insight into the transfer of water on a planetary scale.

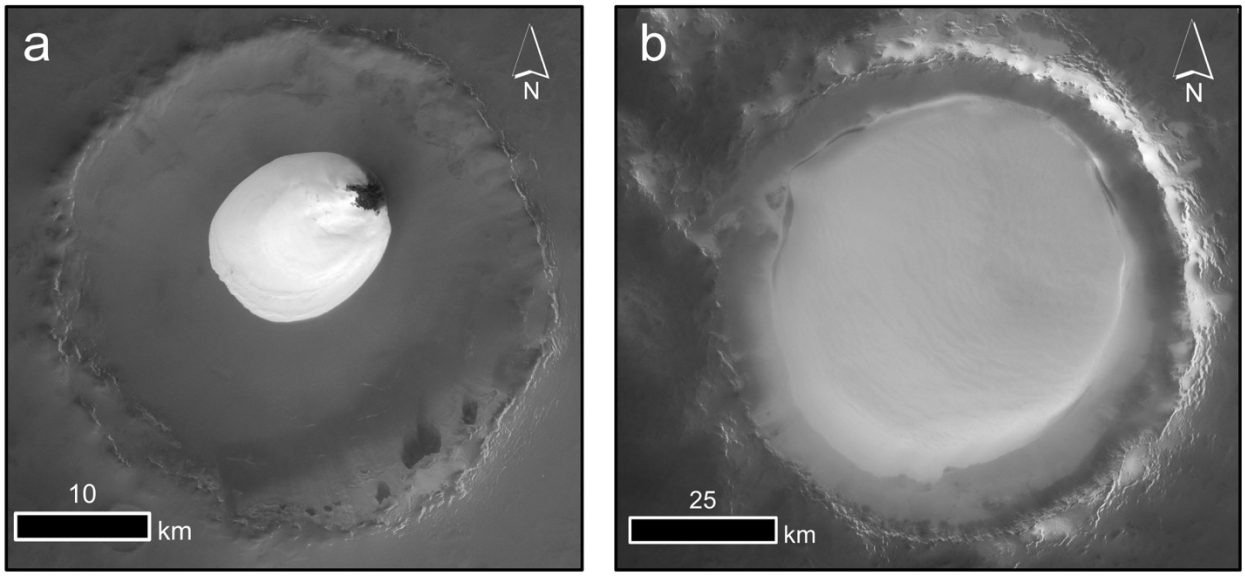

Figure 3.1. (a) Louth (HRSC_1343_0000) and (b) Korolev (HRSC_5726_0001) craters.

3.2 METHODS

Our study addresses the present-day mass balance of these two ice mounds. First, we analyze high-resolution, multi-year observations of the ice mound boundary, to constrain the extent of interannual changes. This method is only applied at Louth due to the lack of sufficient high-resolution coverage at Korolev. A model is developed and used to calculate mass balance for martian ice mounds. Using temperatures derived from the Thermal Emission Spectrometer (TES) we are able to constrain surface thermophysical properties of the Korolev ice mound. Due to insufficient instrument resolution, we cannot perform the same thermal analysis over the smaller Louth ice mound. Therefore, based on similar composition, surface texture, and latitude, we assume it shares the same thermophysical properties. We develop and couple an atmospheric water mixing model to our thermal model, which allows for exchange of water between the surface and the atmosphere. We study a range of model inputs with emphasis placed on albedo, windspeed, and slope.

3.2.1 *High-resolution Image Analysis*

We track the Louth ice mound boundary using multiyear, high-resolution images, to identify any changes that indicate a longer-term trend. Distinguishing between new and old ice at visible wavelengths is ambiguous. Thus, we search only for lateral changes between the ice and bare-regolith surface at the mound boundary.

Louth crater has been repeatedly imaged by the High Resolution Imaging Science Experiment (HiRISE) for over four Mars years (MY28-33). The HiRISE instrument (McEwen *et al.*, 2007) consists of a 0.5 m mirror and CCD's capable of imaging at blue, green, red, and near-infrared wavelengths (~0.4-1.0 μm). At nadir viewing in the north polar region, HiRISE can achieve up to ~0.3 m/pixel sampling, which is crucial for identifying any changes in the extent of the ice mound.

Of the approximately 40 HiRISE images at this location, our analysis is restricted to about 20 of those (Table S1). The criteria for selecting favorable images include restricting the data by season to L_S=90-160°, or northern summer, in order to minimize the presence of atmospheric dust and ice clouds (Benson *et al.*, 2011), as well as seasonal CO_2 (Piqueux *et al.*, 2015b) and water (Bapst *et al.*, 2015) frosts. We restrict emission angles to <10° to minimize distortions due to topography. Any image with obvious signs of seasonal frost and/or clouds was omitted. Lastly, the northeast region of the mound is ignored in our analysis due to incomplete coverage and the presence of dunes/aeolian deposits which obscure the ice mound boundary (Brown *et al.*, 2008).

Overlapping images were georeferenced to each other in ArcMap in order to identify changes in ice extent. While referencing the images, we focused on matching features (i.e., tie points) close (<100 m) to the ice boundary. This is valid since our study focuses only on the ice

boundary, and not features on the mound or large distances (>100 m) from the boundary. Examples of tie points used are the intersections of polygonal troughs or large rocks. Approximately 20-30 tie points were used per image pair and were fit using a spline transformation as this produced the least distortion when flipping between images.

3.2.2 *Thermal Modeling*

Observed Temperatures

We constrain model surface properties (e.g., thermal inertia; TI) using observed temperatures from Mars Global Surveyor Thermal Emission Spectrometer (TES). Due to its larger foot print (~6x3 km), and susceptibility to smearing in the downtrack direction (Titus *et al.*, 2001; Putzig *et al.*, 2004), we cannot be confident in identifying TES temperatures of the ~10 km Louth ice mound without mixing of the surrounding, lower TI, regolith. Instead, we derive surface properties for the larger ice mound in Korolev crater, and assume Louth shares the same properties. At Korolev, the water ice mound fills a large fraction of the 83 km diameter crater and encompasses many TES footprints, thus alleviating concerns of subpixel mixing between ice and regolith.

We use JMARS GIS software (Christensen *et al.*, 2009) to acquire TES temperatures, and Lambert albedo for desired spatial and temporal conditions. Both AM and PM data are collected, and are used both individually and together as described in our fitting methods below. Our nominal case will include the best-fit TI derived using both AM and PM temperatures combined. This approach minimizes error between the TES dataset and our model (Table S1).

Thermal Model Description

We use a surface energy balance and 1-D heat diffusion model to calculate surface and subsurface temperatures for our regions of interest. Subsurface temperatures are simulated by solving the heat equation via the Crank-Nicolson method (i.e., semi-implicit), and heat fluxes are calculated across layer interfaces. The model grid is non-uniform in space, with increasing layer thickness with depth. The top and bottom boundaries are governed by surface energy balance and Mars heat flow (30 mW m^{-2}), respectively. Model inputs can be seen in Table 3.1, and model variables in Table 3.2.

At the surface, incoming and outgoing radiation are balanced along with conduction into the subsurface and, at times, the latent heat due to phase transitions of CO_2 ice:

$$S(1-\alpha) + F_{vis\downarrow}(1-\alpha) + \epsilon F_{IR\downarrow} + L\frac{dm}{dt} + k\frac{dT}{dz} = \epsilon\sigma T^4 \qquad (3.1)$$

Scattered visible light (F_{vis}) is parameterized as an additional 2% of the solar flux while downwelling infrared (F_{IR}) is an additional 4% of the noontime flux (Aharonson and Schorghofer, 2006; Dundas and Byrne, 2010). The model allows for the formation of CO_2 ice when saturation conditions are met. CO_2 frost point temperature is calculated using Viking Lander pressure measurements (Tillman *et al.*, 1993) which are extrapolated to the elevation of the ice mound surface, approximately -4.5 km for both craters. When CO_2 ice is present, the surface albedo is changed to 0.6 and the emissivity to 0.9. Surface emissivity is 0.95 otherwise.

Derivation of Thermal Properties

In determining whether a model is a good fit to TES data we calculated a reduced chi-squared statistic, χ^2:

$$\chi^2 = \frac{1}{(N-2)}\sum\frac{\left(T_{obs,i}-T_{model,i}\right)^2}{\gamma^2} \qquad (3.2)$$

Here, T is temperature, γ is TES target temperature variance (0.4 K for a surface temperature of 280 K and 1.5 K for a surface at 150 K; Christensen *et al.*, 2001), and N is the number of data points minus the number of degrees of freedom.

We calculate fits for the Korolev water ice mound using a one layer thermal model (i.e., one set of thermal properties for all depths). Aside from the presence of seasonal CO_2 ice, we set surface albedo constant, and investigate a range between 0.3 and 0.6 in 0.01 increments, based on the observed range from TES (discussed further in Section 3.4.3). We vary the TI from 500-2500 J m^{-2} K^{-1} $s^{-1/2}$ in increments of 50 J m^{-2} K^{-1} $s^{-1/2}$, thus our range includes the TI of pure water ice (2170 J m^{-2} K^{-1} $s^{-1/2}$). Although albedo is one of our fitting parameters, we explore a range in our mass balance calculations. This is due to its relative uncertainty, seasonal variability, and because it strongly controls daytime surface temperatures.

Table 3.1. Model Inputs

Parameter	Description	Value	Units
α	Albedo	0.35-0.65	Dimensionless
ϵ	Emissivity	0.9-0.95	Dimensionless
L	Enthalpy of Sublimation of CO_2	5.899×10^5	J mol^{-1}
k	Thermal Conductivity	1.8-2.05	W m^{-1} K^{-1}
u	Wind Speed	1, 3, 5	m s^{-1}
κ	Von Karman Constant	0.4	Dimensionless
z_o	Surface Roughness	0.001	m
f	Coriolis Parameter	[1]$\sim 2 \times 10^{-4}$	rad s^{-1}
D	Molecular Diffusivity of water vapor in CO_2 gas	[2]$\sim 1 \times 10^{-3}$	m^2 s^{-1}

[1]Calculated at ~70ºN, where $f = 2\Omega \sin(\text{latitude})$ where Ω is rotation rate (rad s^{-1})
[2]Calculated after Chittenden *et al.* (2008)

Table 3.2. Model Variables

Parameter	Description	Units
S	Solar Flux	W m^{-2}
T	Surface Temperature	K
u_*	Surface Friction Velocity	m s^{-1}
h	Logarithmic Wind Profile Height	m
f	Coriolis Parameter	rad s^{-1}
d	Laminar Layer Thickness	m
ν	Atmospheric Kinematic Viscosity	m^2 s^{-1}
K	Eddy Diffusivity	m^2 s^{-1}
ρ	Atmospheric Density	kg m^{-3}
ρ_v	Water Vapor Density	kg m^{-3}
Γ	Water Vapor Mixing Ratio	mol mol^{-1}
c	Free Convection Rate	m s^{-1}
D	Molecular Diffusivity of water vapor in CO_2 gas	m^2 s^{-1}
$\dot{m}$	Water Vapor Mass Flux	kg m^{-2} s^{-1}

Slope Model

Conway *et al.* (2012) report a mean surface slope for Louth and Korolev of 3.2º and 3.5º, respectively. Due to their quasi-domal shape, the steepest slopes generally occur near the boundary and decrease towards the center of the ice mounds. A flat model is therefore more representative of the center of the mound. Because our focus with HiRISE is the boundary of the Louth ice mound, we must consider the effect of slopes. A digital elevation model (DEM) constructed from HiRISE stereo pair images supplies us with a ~1 m resolution slope map (Fig. 3.2). A transect of the DEM shows a rough surface with a wide range of slopes, up to 25º. The mean slope near the boundary is about 7º, thus we model slopes of 5º and 10º for both equatorward and poleward facing cases.

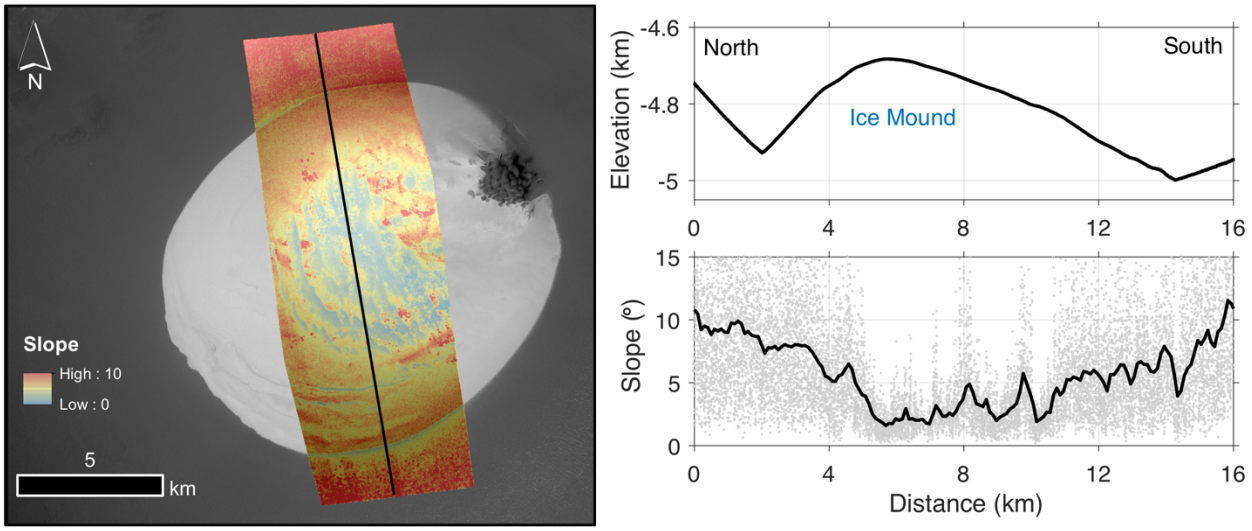

Figure 3.2. (left) Slope map from HiRISE DTEPC_045439_2505_045887_2505_A01 over Louth crater ice mound (CTX B22_018301_2503_XN_70N257W). (right) Plots of elevation and slope for transect running approximately north-south. Note the increasing slope towards the edges of the ice mound.

Our model accounts for the radiative effects from surrounding terrain, as well as limiting view of the sky, similar to the model described in Aharonson and Schorghofer (2006). The

surrounding terrain is modeled as a semi-infinite plane, which requires its own set of thermal properties, as it represents a regolith surface. Due to similarities in latitude we adopt the regolith and ice table properties of the Phoenix landing site (Mellon *et al.*, 2009; Zent *et al.*, 2010). Properties include a regolith TI of 300 J m^{-2} K^{-1} $s^{-1/2}$, a depth to ground ice of 5 cm, and a surface albedo of 0.25. All other properties remain the same as thermal models of the ice mounds.

3.2.3 *Atmospheric Model*

We develop a 1-D atmospheric model to simulate boundary-layer water vapor mixing and water ice accumulation/ablation, i.e., exchange of water vapor with the surface (Fig. 3.3; Table 3.1, 3.2). The model domain extends from the surface to 6 km altitude, a typical boundary layer height on Mars (Haberle *et al.*, 1993, Petrosyan *et al.*, 2011). Pressure is assumed constant with time and decreases with altitude, using a scale height of 11 km. We assume the atmospheric temperature at the surface is equal to the diurnal mean surface temperature and then decreases at a rate of -4.5 K km^{-1} (Petrosyan *et al.*, 2011). The interface of the mixing model and surface is assumed to be a relatively shallow, laminar layer where vapor transport to and from the surface is governed by molecular diffusion and free convection (Fig. 3.3).

We do not allow for the condensation of volatiles in the atmosphere. Although nucleation of water ice crystals was observed in the boundary layer at the Phoenix Lander site (Whiteway *et al.*, 2009), the ice sublimated before reaching the surface and it is not clear if any surface accumulation of water ice via snowfall occurs today. Modeling this complex process of atmospheric condensation and potential precipitation is outside the scope of this paper. If snowfall is an important part of the present-day mass balance then our model results may underestimate accumulation.

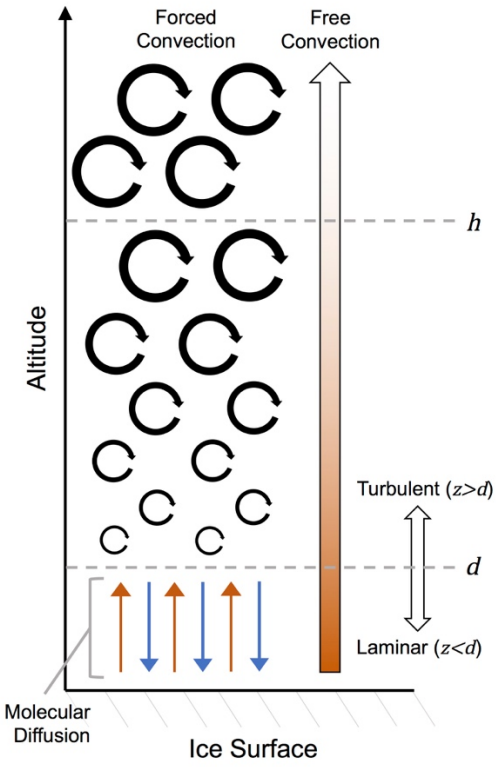

Figure 3.3. Cartoon schematic of the atmospheric model. The mixing model (z>d; i.e., turbulent) includes eddy diffusion (i.e., forced convection) and free convection. Eddy diffusivity increases with altitude until z=h, then remains constant. Free convection becomes less effective with height because density inversions only occur near the surface where sufficient water vapor is available. The surface accumulation/ablation model (z<d; i.e., laminar) includes molecular diffusion and free convection between the surface and the base of the turbulent zone.

Our mixing model includes treatments for both free and forced convection. Both models use an explicit numerical approach. In line with the approaches of previous authors (e.g., Wallace and Sagan, 1979; Svitek and Murray, 1990; Zent *et al.*, 1993) we assume a logarithmic wind profile, which depends on surface roughness, z_o.

$$\frac{u}{u_*} = \frac{1}{\kappa}\ln\left(\frac{z}{z_0}\right) \qquad (3.3)$$

Here, *u,* is the horizontal wind velocity at height, *z*. u_* is the surface friction velocity, and κ is the Von Karman constant, equal to 0.4. We must estimate a value for the aerodynamic surface roughness of the ice mounds, as there are no direct measurement of this property. Here we assume a value of 1 mm, within the range of terrestrial ice sheets (Paterson, 1994), as well as similar to those used previous studies of martian ice (Wallace and Sagan, 1979; Dundas *et al.*, 2010). Assuming a value for the horizontal wind speed (Table 3.1) at height, *z*, will yield u_* which in turn determines the forced convection mixing rate (i.e., eddy diffusivity). Free convection mixing rates are determined, in part, by the gradient in atmospheric density and water vapor.

Eddy diffusivity will increase with height until a limiting height, *h*, above which eddy diffusivity remains constant (Svitek and Murray, 1990). This height is defined as

$$h \sim 0.2 \frac{u_*}{f} \qquad (3.4)$$

where *f* is the Coriolis parameter, which varies with latitude (see Table 3.1).

For the near-surface laminar layer, we estimate its thickness, *d*, after Wallace and Sagan (1979):

$$d = 30 \frac{\nu}{u_*} \qquad (3.5)$$

where ν is the kinematic viscosity of the atmosphere. This value can be thought of the height for which the atmosphere transitions from laminar to turbulent flow, and is typically 1-3 cm. The diffusivity of the lower layer is based on laboratory experiments of water vapor diffusion under Mars conditions (~0.001 m^2/s; Hudson *et al.*, 2007; Chittenden *et al.*, 2008). The laminar layer is used to calculate the exchange of vapor through the lower boundary in the mixing model, thus allowing for deposition and sublimation of water ice. Free convection is allowed to transport water vapor away from, but not towards the surface (i.e., ablation only).

Forced Convection Mixing

Our forced convection model is driven by horizontal wind, *u,* at a given height above the surface (Eqn. 3). Wind measurements taken by the Viking Landers, at a height of 1.6 m, show an average around 2-3 m/s (Hess *et al.*, 1977). Here we use a range of wind speeds at 1.6 m: 1, 3, and 5 m s^{-1}. In our model, wind, and therefore forced convection mixing rates, are constant in time. Viking and Phoenix landers both observed a dependency of wind speed with local time, namely with gusty periods recurring at specific local times (Hess *et al*., 1977; Holstein-Rathlou *et al*., 2010). Although we do not model this complexity, we expect gusts >5 m s^{-1} will increase mixing rates beyond what is modeled here and therefore enhance accumulation or ablation, depending on local time, season and model parameters. Conversely, periods of quiescence, that we also do not model, will suppress mixing and so accumulation and ablation rates.

After calculating u_* (Eqn. 3), we can solve for the eddy diffusion coefficient, *K,* after

$$K = \kappa \cdot u_* \cdot z \qquad (3.6)$$

We calculate this value from $z=d$ to $z=h$, and then use the value at h for $z>h$ (K=0 for $z<d$). Eddy diffusivity is used to simulate convective mixing in a 1-D diffusion model, similar to the approach outlined Zent *et al.* (1993).

$$\rho \frac{\partial \Gamma}{\partial t} = \frac{\partial}{\partial z}\left(\rho K \frac{\partial \Gamma}{\partial z}\right) \qquad (3.7)$$

Here the diffused quantity is water mixing ratio, Γ, and ρ is the atmospheric density. We solve Eqn. 7 numerically, allowing changing K with altitude, and a non-uniform grid.

Free Convection Mixing

Free convection in our mixing model is driven by unstable, positive gradients in total atmospheric density (i.e., buoyant air), whereas a stable density gradient (i.e., decreasing density with altitude) is negative. Density depends, in part, on mean molecular mass, and adding water to

the martian atmosphere can reduce this (Ingersoll, 1970). The atmospheric model produces positive density gradients when sufficient amounts of sublimated water vapor lead to such decreases in density.

This buoyancy-driven mixing acts in only one direction, away from the surface. We model the process by calculating the upward vertical flux of water vapor between model layers that exhibit inverted density gradients. We assume unidirectional transport (c>0) and solve the advection equation (Eqn. 8) numerically using the up-wind differencing scheme (Pelletier, 2008).

$$\frac{\partial \rho_v}{\partial t} = c\frac{\partial \rho_v}{\partial z} \qquad (3.8)$$

Water vapor density, ρ_v, is transported vertically only where positive atmospheric density gradients are present. Advection occurs at a rate proportional to c (in units m s^{-1}), which we parameterize after previous free convection approaches for Mars (Ingersoll, 1970; Hecht, 2002; Dundas and Byrne, 2010).

$$c = 0.15\ D\ [GrPrLe]^{\frac{1}{3}}\ \frac{1}{\Delta z} \qquad (3.9)$$

We use expressions from Hecht (2002) for the Grashof (Gr), Prandtl (Pr), and Lewis (Le) numbers and D is the diffusivity of water vapor in CO_2 gas. The final form for our advection rate is

$$c = 0.15\ \left[\left(\frac{g}{\nu}\right)\left(\frac{\Delta\rho}{\Delta z}\right)\frac{D^2}{\rho}\Delta z^4\right]^{\frac{1}{3}}\frac{1}{\Delta z} \qquad (3.10)$$

where g is martian gravity, 3.71 m s^{-2}.

Surface Exchange and Boundary Conditions

Transport of water vapor through the laminar atmospheric layer between the surface and our mixing model occurs via molecular diffusion and free convection. Molecular diffusion acts in both directions (i.e., can lead to either deposition or sublimation) while free convection only

occurs when the surface is undergoing sublimation. In the thermal model we neglect the effect of latent heat with respect to phase changes of water ice. Our results, at the most extreme, show a maximum of ~100 μm of water ice sublimated diurnally. In this case, the calculated effect due to latent heat equates to a maximum temperature depression of <1 K (due to sublimation), which is less than the uncertainty in TES data and therefore our thermal model.

Molecular diffusion of vapor into and out of the lower-most atmospheric mixing model layer is calculated as

$$\dot{m} = D\frac{(\rho_{v,atm}-\rho_{v,sat})}{d} \quad (3.11)$$

where $\dot{m}$ is the mass flux (kg m^{-2} s^{-1}) through the laminar layer of thickness d (Eqn. 5). For this study, we can set $\rho_{v,sat}$ equal to the saturation water vapor density (calculated from our modeled surface temperature) because we are considering a surface of perennial water ice. $\rho_{v,atm}$ comes from the lowermost layer in our atmospheric mixing model. A positive flux indicates ice deposition while a negative flux indicates ablation. The calculated mass of water vapor is placed into or removed from the bottom atmospheric layer, which is then allowed to subsequently evolve with the mixing model.

Free convection transport from the surface to the mixing model is determined after Dundas and Byrne (2010). There are only a couple of minor modifications made to this scheme. Instead of a diurnally varying atmospheric temperature based on surface temperature, we assume the atmospheric temperature is equal to the diurnal mean surface temperature. Additionally, instead of a constant value of atmospheric vapor density we incorporate the value of our lower-most mixing model layer, which varies in time, to determine mass flux.

The upper boundary of the model is prescribed using 6 km altitude water vapor densities from the Laboratoire de Météorologie Dynamique (LMD) Mars Climate Database (MCD;

Millour *et al.*, 2014). These GCM results were acquired in 10° L_S increments and interpolated to meet our model time step (Fig. 3.4).

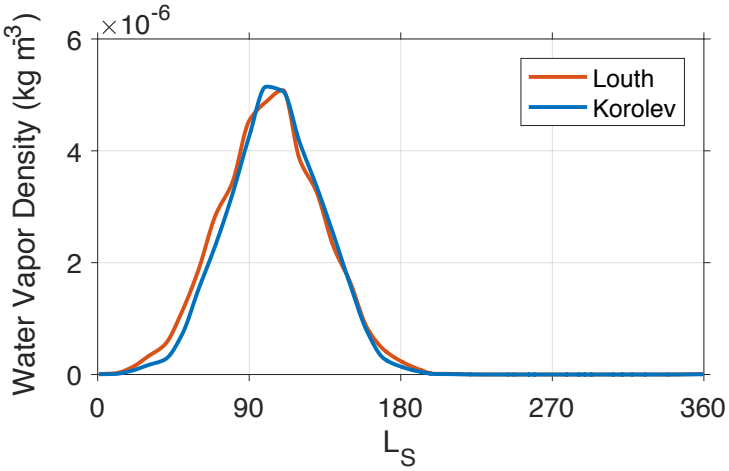

Figure 3.4. Water vapor density at 6 km from LMD MCD for Louth and Korolev. Data was acquired in 10º L_S increments and interpolated. These curves represent the top boundary condition in our atmospheric mixing model.

Lateral Atmospheric Mixing

Our 1-D model assumes no lateral transport of water vapor. While this assumption may be valid for large ice sheets (e.g., regions of the NPRC), it may over or underestimate the water vapor content of the atmosphere during certain seasons for smaller ice deposits. We suspect this would be most important in summer when the ice mound ablation rate is highest. The expected plume of water vapor above the mound will mix with the surrounding atmosphere, which does not sit above a perennial ice deposit, and would therefore contain less vapor. The omission of this effect restricts ablation in the model. If we assume our calculated eddy diffusivity rate acts equally in the lateral direction, the approximate length scales are 4 and 75 km, for timescales of one sol and one half of a Mars year, respectively. We suggest 1-D models may underestimate ice loss for smaller ice mounds (diameters <10 km). Lateral transport is more important at the

boundaries. Therefore, our mass balance model is more applicable to the center of the mound. Mass balance where net ablation is predicted should be considered a lower limit, especially for the Louth ice mound.

3.3 RESULTS

3.3.1 *Multiyear HiRISE Image Analysis*

The morphology of the boundary varies about the perimeter of the mound. The north and south sides of the mound exhibit some key differences (Fig. 3.5). The northern boundary is abrupt, hosting off-mound patches of ice in some areas but typically not extending from the ice-covered surface more than 10-20 m (Fig. 3.5a). The southern boundary of the mound is more diffuse, with patchy, light-toned material (likely water ice), extending out 100s of meters from the ice mound (Fig. 3.5b). The size of these ice patches varies but most are between 1-10 m. No interannual changes were observed at the southern boundary.

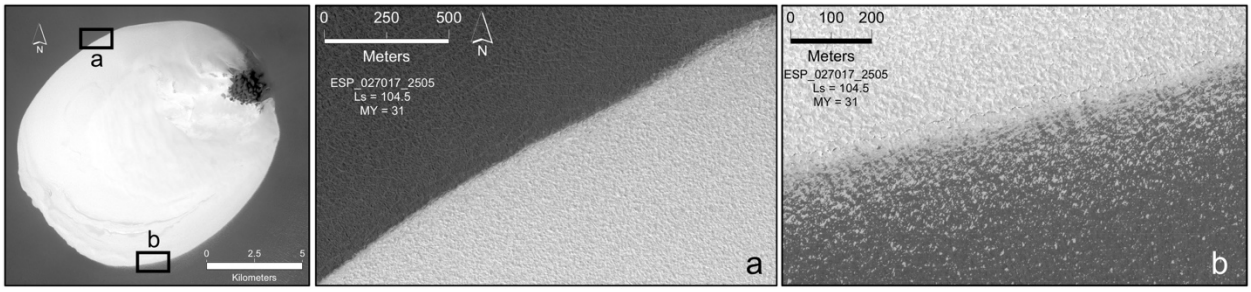

Figure 3.5. CTX image (CTX B22_018301_2503_XN_70N257W) of the Louth ice mound with HiRISE insets showing the different morphology between the (a) north and (b) south sides of the mound, blue and red outlines, respectively.

The north-northwest side of the mound exhibits a region (~1 km along the perimeter) where apparent changes in ice extent are observed (Fig. 3.6). Between MY30/31, the ice boundary appears to retreat 5-10 m. In MY32, the boundary appears to have advanced back to its

MY30 extent. One hypothesis is the removal and replacement of surface ice; however, this seems unlikely because the ice returns to the exact same position as MY30. An alternate hypothesis is that ice was covered and then exhumed by a thin veneer of windblown sediment. Future monitoring may shed light on potentially important aeolian processes occurring on or around the ice mound. Aside from this one example, no other sections of the ice mound boundary showed interannual variation. Regardless of the cause for the observed activity, the observations do not support a secular trend for the current mass balance of the ice mound.

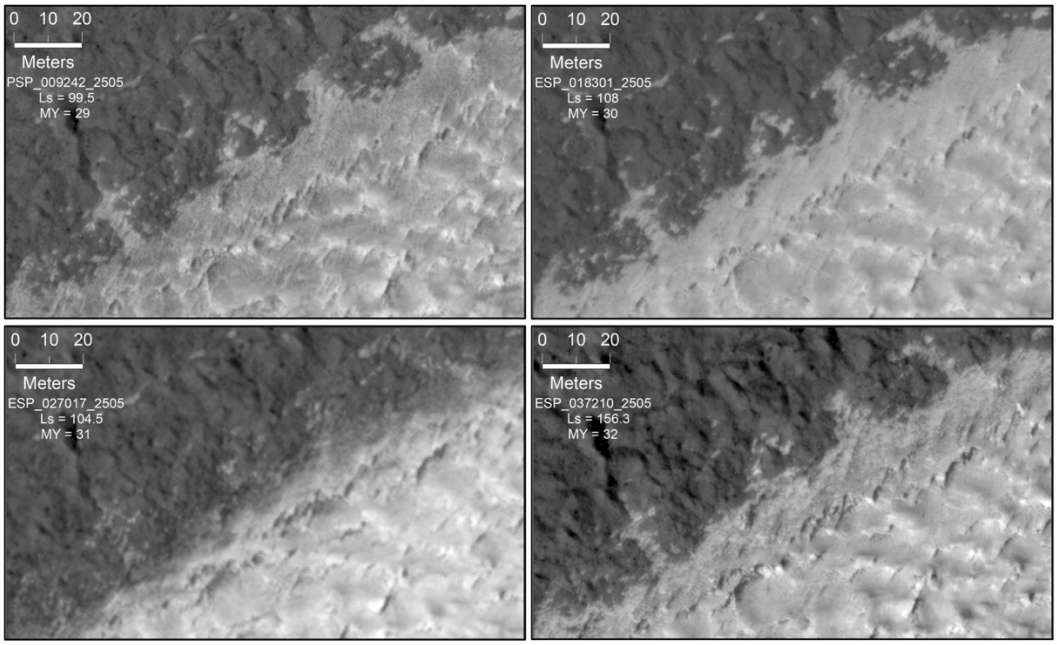

Figure 3.6. Multiyear HiRISE images of the northern boundary (within area of Fig. 3.5a) where extent of the ice mound appeared to vary. Images shown are within the same season, northern summer ($100^{\circ}<L_S<156^{\circ}$), to limit seasonal effects. North is up.

3.3.2 *Modeling Results*

Best-fit Thermal Models

We calculate reduced χ^2 statistics for a range of thermal models against the TES temperatures for the Korolev crater ice mound. We include albedo as our second fitting

parameter, in order to compare with observed albedo from TES, and constrain a nominal modeling case. The range of best-fit TI found is between 1550-2000 J m^{-2} K^{-1} $s^{-1/2}$, and albedo of 0.39-0.47 depending on whether we fit the AM-only, PM-only or AM and PM temperatures (Table 5.2). Thus, our derived properties for Korolev are consistent with an ice deposit, are in line with previous authors estimates of the same region (Armstrong *et al.*, 2005), and are similar to the properties of the NPRC (Paige *et al.*, 1994). The relatively high TI we find is rare on Mars, whose surface is dominated by regolith and dust (TI <500 J m^{-2} K^{-1} $s^{-1/2}$; Edwards and Bandfield, 2009). Moving forward, we choose a nominal value for TI from the best-fit to AM and PM temperatures together (1550 J m^{-2} K^{-1} $s^{-1/2}$; Fig. 3.7). We also vary albedo between 0.35-0.50, which encompasses the range of derived values from fitting TES temperatures (Table 5.2).

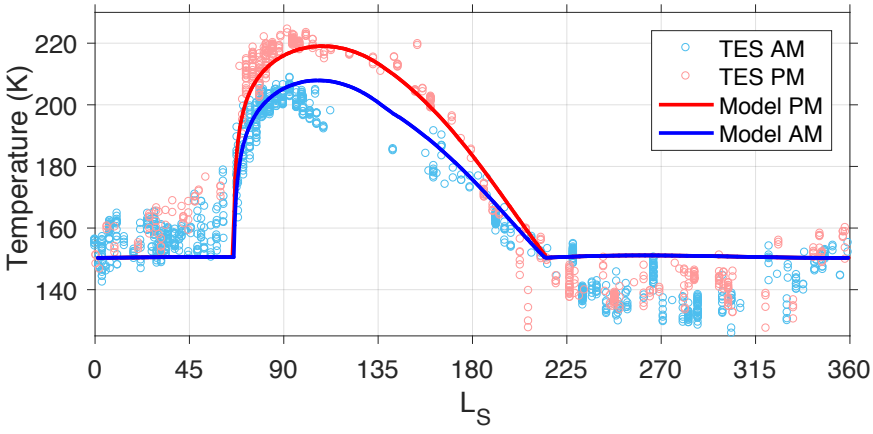

Figure 3.7. Annual AM and PM temperatures for modeled Korolev ice mound plotted over TES data. The AM and PM curves shown here are for their respective best fit parameters; i.e., for both AM and PM data: TI = 1550 J m^{-2} K^{-1} $s^{-1/2}$, α=0.42.

Mass Balance of Louth and Korolev Ice Mounds

Modeled mass balances show varying degrees of dependency with respect to our tunable parameters, i.e., wind speed (Fig. 3.8) and albedo (Fig. 3.9). We describe results for the full range of these parameters in this section. Mass balance is described in units of water ice

thickness, assuming an ice density of 920 kg m^{-3}. Our derived TI range (1550-2000 J m^{-2} K^{-1} $s^{-1/2}$) is lower than expected for pure water ice (2170 J m^{-2} K^{-1} $s^{-1/2}$). This difference can be explained by the presence of pores in the ice, which would lower the density and the thermal conductivity (Paterson, 1994). If the conductivity were unaffected by porosity, the implied density for our nominal TI of 1550 J m^{-2} K^{-1} $s^{-1/2}$ would equal 470 kg m^{-3} (i.e., a porosity of 0.49). However, conductivity is likely affected by porosity, so the actual porosity could be less and so the density higher. Ultimately, height changes could be up to 2 times higher than reported in the text and figures due to ice porosity.

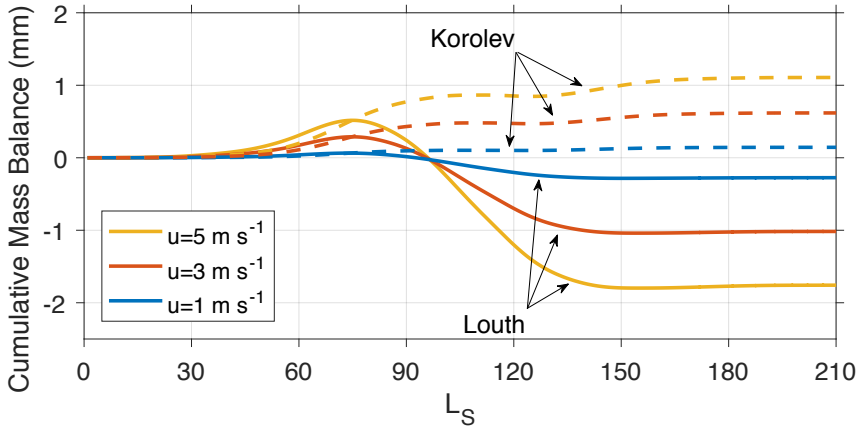

Figure 3.8. Cumulative mass balance at Louth (solid lines, albedo=0.40) and Korolev (dashed lines; albedo=0.45) for three wind speeds (see legend). Resulting annual mass balances at Louth are -0.27, -1.02, and -1.76 mm per Mars year, Korolev yields +0.14, +0.62, and +1.11 mm per Mars year, each for wind speeds of 1, 3, and 5 m s^{-1}, respectively.

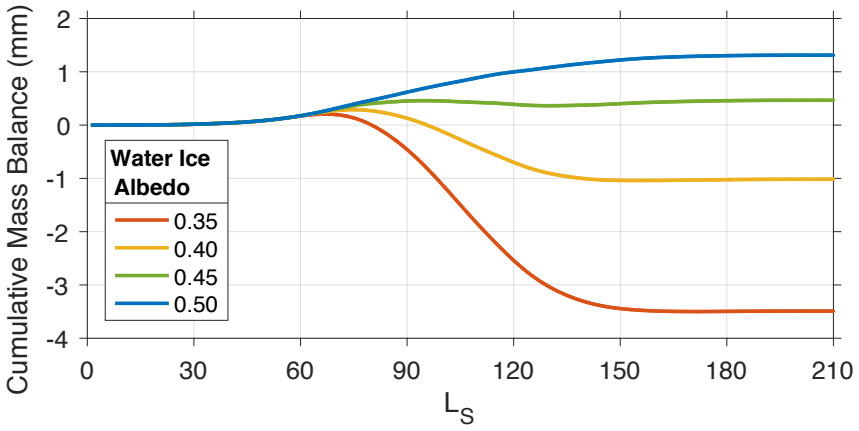

Figure 3.9. Cumulative mass balance at Louth for five albedo cases in our range of 0.35 to 0.50. Models shown were run for one wind speed, u=3 m s^{-1}.

Increasing wind speed results in faster mixing rates in the atmosphere, and thus allows quicker transport of water to and from the surface. Wind speed in our model does not change the sign of the annual mass balance (e.g., +/-; Fig. 3.10), but will enhance either accumulation or ablation (Fig. 3.8). We adopt u=3 m s^{-1} as our nominal wind case, as it is closest to the observed, average wind speed at the Viking Lander sites (Hess *et al.*, 1977).

The prescribed water-ice albedo has a strong influence on temperatures, and thus the sublimation and deposition of ice (Fig. 3.9). Albedo also has control over the sign of the annual mass balance (Fig. 3.10). For u=3 m s^{-1}, and a range of albedo of 0.35 to 0.50, our model yields annual mass balance of -3.49 to +1.31 mm and -2.80 to +1.34 mm per Mars year for Louth and Korolev, respectively. The steady-state (mass balance equals zero) albedo values are 0.431 and 0.423 for Louth and Korolev, respectively. Thus, the change in latitude between these sites requires only a small increase in albedo (~0.01) to stabilize an ice deposit at Louth versus Korolev.

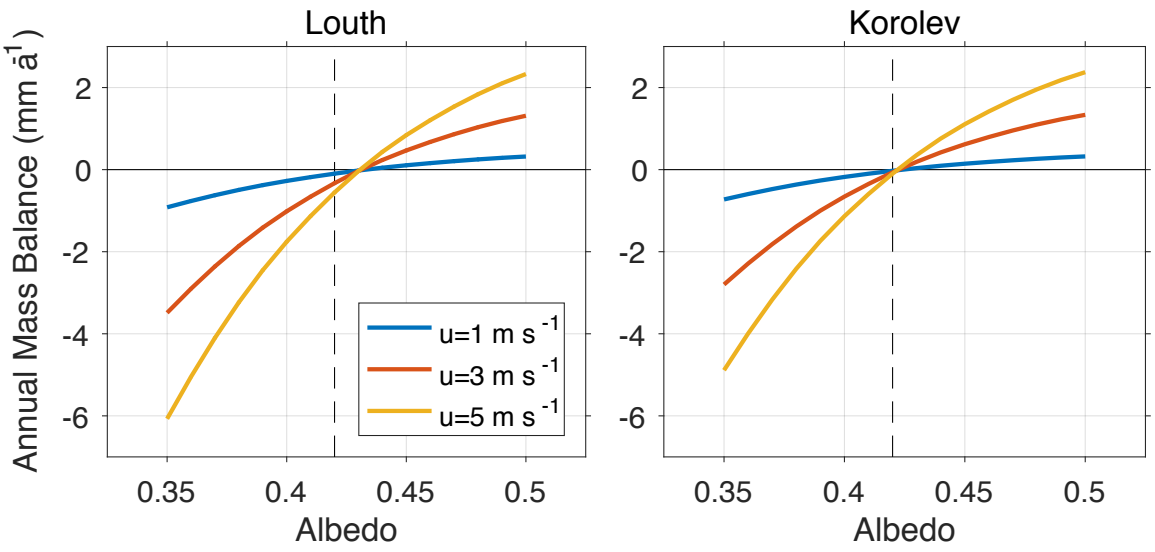

Figure 3.10. Net annual mass balance as a function of albedo for (left) Louth and (right) Korolev, shown for the three wind speeds investigated. The dashed line represents our best-fit albedo (0.42).

Seasonal Trends in Accumulation and Ablation

Seasonal trends can be characterized using cumulative mass balance for our nominal windspeed (u=3 m s^{-1}; Fig. 3.9). We describe the seasonal behavior for both net accumulation (e.g., higher albedo), and net ablation (e.g., lower albedo) cases. In all models, spring involves the defrosting of CO_2 ice on both ice mounds (L_S~60°) which is closely followed by accumulation of water ice as the atmosphere begins to become more humid (Fig. 3.11). Between L_S~75-90°, models with lower albedo will switch from accumulation to ablation. In high ablation cases, the rates do not vary considerably with season, but do reach a maximum around L_S~110°. Models with high albedo continue to accumulate through late spring and summer. Mid-range albedo models that showed ablation after L_S~90° will revert back to accumulation later in the summer (L_S>150°), as peak temperatures have passed. The amount of accumulation in late summer is usually several times less than accumulation occurring between L_S=60-90°. In late

summer the atmosphere loses water vapor due to both the mixing of drier air at 6 km, and the deposition of ice at the surface (Fig. 3.11). Though minor, the atmosphere also shows nighttime depletion throughout summer (<5 pr-µm of water). For the rest of the year, and into the next (L_S=220-60°), seasonal CO_2 ice is present and any source of water vapor from the surface into the atmosphere is inhibited by cold temperatures (≤150 K). The dry atmosphere during this time allows only a small amount of surface accumulation.

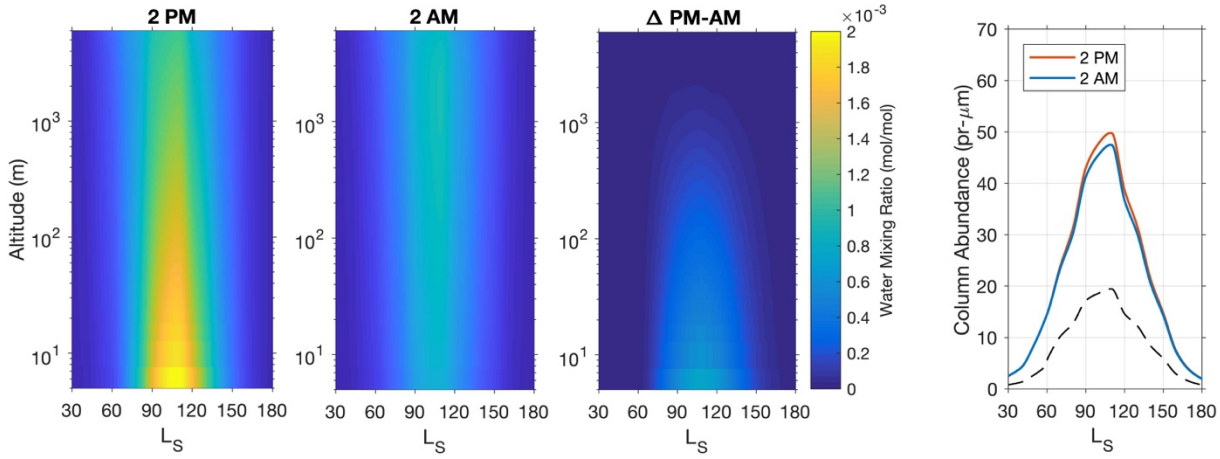

Figure 3.11. Seasonal and diurnal behavior of water at Louth for an albedo of 0.42 and u=3 m s^{-1}. Note the $\log_{10}$ vertical axes (altitude) and L_S range (showing only spring and summer). (left) 2 PM vertical water mixing ratio (left-middle) 2 AM vertical water mixing ratio, and (right-middle) their difference. During summer, significant nighttime depletion occurs diurnally, from the surface to a few hundred meters in altitude. (right) Column integrated mass of water up to 6 km as a function of season for 2 AM and 2 PM. Nighttime depletion during peak water vapor seasons is <5 pr-µm. The dashed line represents the estimated amount of atmospheric water vapor above the model domain, assuming water is evenly-mixed and extends to one scale height.

3.4 DISCUSSION

3.4.1 *Potential for Observing Change at Louth*

Here, we estimate the timescale required to detect change in images at HiRISE resolution (i.e., ~25 cm per pixel). We consider results from our thermal and accumulation model for sloped cases (see Section 3.2.2 for description of slope model). From the HiRISE DEM (Fig. 3.2) we calculate a slope at the mound boundary of 7°. For this slope about 3 cm must be removed vertically to remove 25 cm of ice laterally at the boundary (i.e., exposing 1 pixel of regolith). Thus, over our baseline of 4 Mars years, an accumulation or ablation rate of about 1 cm per Mars year is required in order for a change to be detected with HiRISE. Modeled ablation rates show significant enhancement on equator-facing slopes of 5-10° (Fig. 3.12). For an equator-facing slope of 7° our model predicts an ablation rate of about -2 mm per Mars year, under nominal conditions. At this rate, a one pixel change observed by HiRISE would require about 15 Mars years or 28 Earth years. Detection via our methods likely requires many pixels of change between images to identify loss, thus our time estimate is a lower limit. Improved topographic data (e.g., from stereo imaging) will be helpful in determining areas (e.g. steeper slopes) that are likely candidates for observable change.

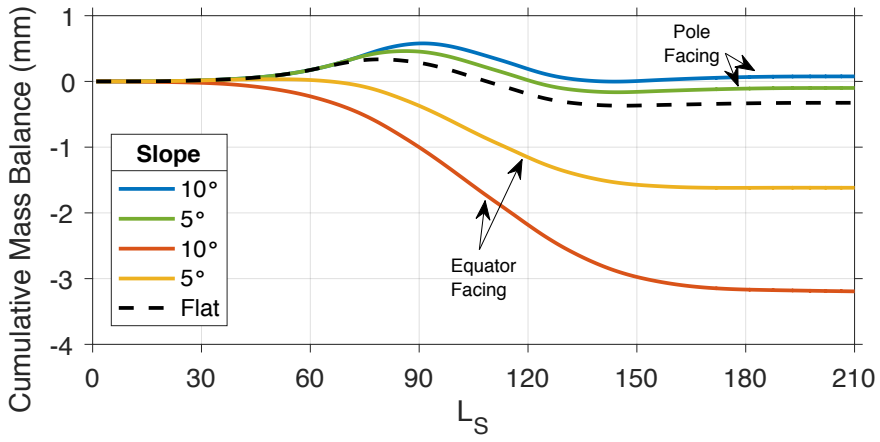

Figure 3.12. Cumulative mass balance at Louth for sloping surfaces of 5º and 10º, and for both equator- and pole-facing slopes. Models shown were run for a windspeed, u=3 m s^{-1}, and a constant albedo of 0.42.

3.4.2 *Louth and Korolev Comparison*

Model results for the full of range of parameters (Fig. 3.10) show that the two sites behave similarly, as they are separated by only 2.6° in latitude. Our best fit to a combination of AM and PM TES temperatures at Korolev yields an albedo of 0.42 (Table 5.2). We adopt this into our nominal case in order to make predictions for the present-day mass balance at both sites. Following this assumption of ice albedo, we estimate the annual mass balance to be virtually zero (-0.06 mm per Mars year) at present at Korolev. Assuming the ice in Louth crater shares the same albedo, which cannot be directly measured by TES due to sub-pixel mixing, its annual mass balance is -0.32 mm per Mars year.

Should this value of annual mass balance be valid over Louth's recent geologic past, it suggests 1 m of ice loss every 6 kyr. If the Louth ice mound was ablating at this rate it would be completely removed in 1.5 Myr. However, Mars' orbital elements, most notably obliquity, change on 51-120 kyr timescales over the past 20 Myr (Laskar, 2004). Orbital changes will alter annual temperatures globally, which causes increases and decreases in the amount of atmospheric water vapor (Mischna *et al.*, 2003; Chamberlain and Boynton, 2007; Schorghofer and Forget, 2012), and so present-day accumulation/ablation rates are not necessarily representative of the past.

3.4.3 *Seasonally-varying Albedo*

At the Korolev site we have an accurate time series of albedo from TES observations (Fig. 3.13). The mean TES albedo between L_S~60-160° (i.e., clear and seasonal frost-free conditions) is 0.367; however, albedo varies by >25% during this period. Seasonal changes in albedo discussed here have been identified previously for Korolev (Byrne *et al.*, 2008), and similar trends (offset in season) have also been identified in the NPRC (Bass *et al.*, 2000; Byrne *et al.*, 2008; Cantor *et al.*, 2010, Brown *et al.*, 2012; 2016). Korolev shows a decrease in albedo beginning around L_S~60-70° that continues until L_S~90°, likely associated with heterogeneous defrosting of CO_2 ice (Searls *et al.*, 2010), with albedo changing from ~0.45 to ~0.3 in that timespan. At L_S~90° this trend reverses, and albedo increases until L_S~120° where it levels off around 0.40, and slowly decreases into late summer. It is unknown what causes the brightening, though the deposition of fine-grained water ice has been suggested (Armstrong *et al*., 2005; 2007). For L_S>160° data are unreliable as the mound is obscured by the onset of autumn and the formation of the polar hood (Benson *et al.*, 2011).

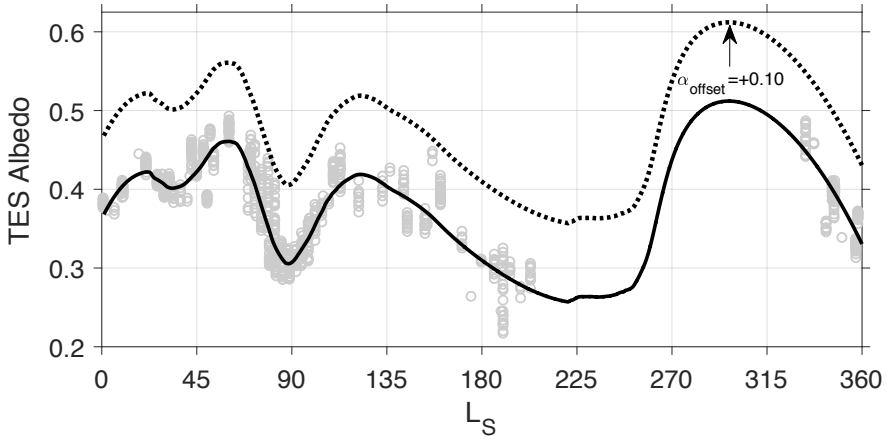

Figure 3.13. TES albedo (grey circles) of the Korolev ice mound, along with the smoothed data (solid line; smoothed with moving window of 20º L_S) used in our model. The change in albedo α_{offset} is applied in our fitting of models with TES temperature data (dotted line).

The timing of changes in accumulation and ablation in our model depends heavily on albedo (Fig. 3.9; Section 3.2.3). Therefore, we explore the effect of observed seasonal albedo variation with respect to seasonal and annual accumulation. In order to quantify the impact of time-variable albedo, we identify models to compare with constant albedo cases.

Our method for finding best-fit thermophysical properties when albedo varies differs from the constant albedo methodology we described earlier. We use the smoothed TES albedo data (Fig. 3.13) for the entire year and apply a constant offset (in increments of ±0.01). We calculate the same reduced chi-squared statistic (Section 3.2.2) between modeled and observed temperatures to find the best-fit thermal inertia and offset applied to the observed albedo variation. With this varying albedo method, the best-fit derived TI is 1250 J m^{-2} K^{-1} $s^{-1/2}$ and albedo offset is +0.10 (Table 5.2). In the data studied here, we find when incorporating a time-varying albedo the best-fit TI is ~20% less than what is derived from constant albedo models and their respective best-fit values.

First, we compare cases of constant and variable albedo by plotting total annual mass balance against the difference from best-fit albedo or best-fit albedo-offset (Fig. 3.14). In general, we find excellent agreement between the two treatments of albedo. One notable difference is that time-varying albedo cases show a slight increase in annual accumulation, and is more pronounced in results for Louth. The difference in steady-state albedo (i.e., value at which net annual mass balance is zero) between the two cases is small (~0.01; Fig. 3.14). This difference is on the order of that between Louth and Korolev steady-state albedo (~0.01; Fig. 3.10). The results suggest that derived properties assuming a constant albedo are valid for estimating the annual mass balance.

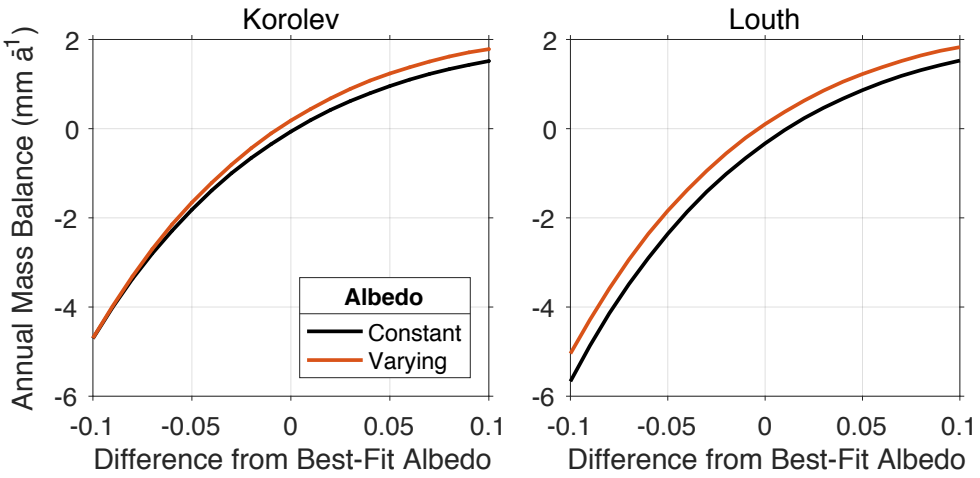

Figure 3.14. Annual mass balance for constant and seasonally-varying albedo at Korolev and Louth, for a wind speed of 3 m s^{-1}. Values are plotted in albedo space as the difference from their respective best-fit albedo (i.e., 0.42 for constant case, and an offset of +0.10 for the time-varying case). The differences are relatively constant over the range of albedo shown, which is equivalent to 0.32 to 0.52 in our constant albedo models.

When comparing seasonal accumulation between the two approaches we see the model predicts similar behavior (Fig. 3.15). However, constant albedo cases do exhibit a prolonged ablation period that persists beyond mid-summer, L_S~140° (Section 3.2.3). In contrast, the cases with time-varying albedo exhibit ablation until L_S~110°, which then levels off over the remainder of the summer. Ablation ends ~30° L_S later for the constant albedo case. The sign of the net mass balance changes between the two cases, but this is only possible as our best-fit albedo yields a near-zero annual mass balance at both sites. Thus, for the best-fit models shown, even small differences (Fig. 3.14) can result in a different sign of annual mass balance (Fig. 3.15).

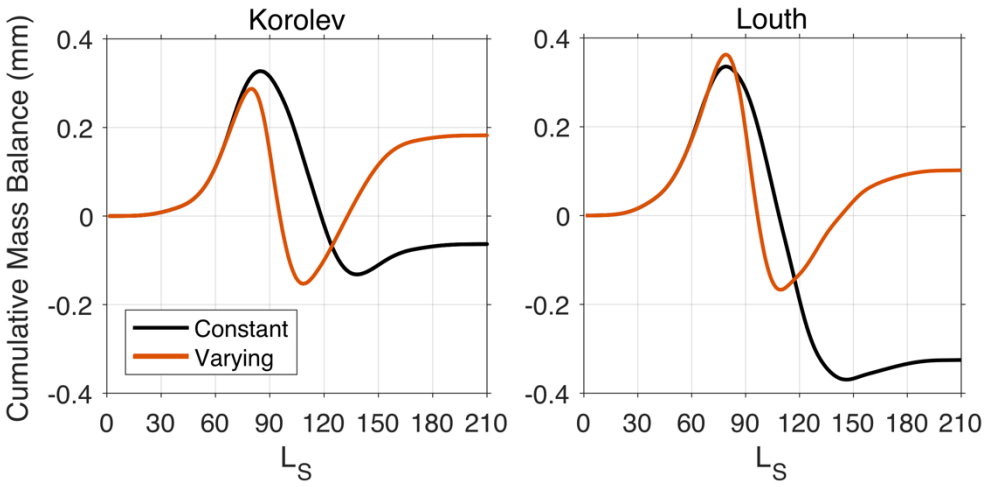

Figure 3.15. Cumulative mass balance using best-fit TI and albedo for cases of constant and time-varying albedo; u=3 m s^{-1}.

3.4.4 *Near-infrared Observations at Louth*

We compare our model output to the results of a near-infrared spectroscopic analysis of changes in water ice absorption at Louth (Brown *et al.*, 2017). This technique has been used previously in determining the timing of deposition and ablation (e.g., "mode flips") that occur throughout the year on the NPRC (Brown *et al.*, 2012; 2016). With repeat near-infrared imaging via the Compact Reconnaissance Imaging Spectrometer for Mars (CRISM), a subtle mode flip was observed at the center of Louth between L_S=100-110° (Brown *et al.*, 2017), corresponding well to the modeled transition between accumulation and ablation seen in models of Louth (Fig. 3.15, constant albedo of 0.42). It should be noted that such models indicate Louth is in a state of net ablation. In contrast, models that result in net accumulation show this transition occurring later in season. Models with time-dependent albedo show different timing in their transition from net accumulation to net ablation (Fig. 3.15), but a more-accurate time series of albedo at Louth is necessary to explore this further. Our work here supports the interpretation that the Louth ice mound is undergoing net ablation at present (Brown *et al.*, 2008). Beyond L_S~150° there is little

data to constrain the ice mound behavior, but our model shows limited accumulation in this period, consistent with the results of Brown *et al.* (2017).

3.5 CONCLUSIONS

Circumpolar ice mounds represent, on average, the warmest ice deposits on the surface of Mars. Thus, they are expected to be sensitive to changes in climate. In the work presented here, we analyze high-resolution images of the most-equatorward example of these ice mounds (Louth Crater) and the temperatures of the largest example (Korolev). Using a thermal and atmospheric mixing model, we estimate the present-day exchange of water vapor between the icy surface and the martian atmosphere. Our range of model parameters is constrained by the observed temperatures, albedo, and slope. In making these calculations we not only gain insight into the long-term stability of such features, but we better understand their role in the global climate system.

The Louth Crater water ice mound has been repeatedly imaged for over four Mars years by the HiRISE instrument, at resolutions up to ~25 cm per pixel. We document the analysis of this high-resolution dataset, to quantify potential changes in the position of the ice mound boundary. In particular, we sought an indication of present-day change in response to the changing martian climate. In our analysis, we find no evidence for secular, interannual changes taking place at the ice mound boundary. However, these constraints are loose, where up to a few cm of ice loss/gain per Mars year is necessary for detection (assuming we are sensitive to single-pixel changes). Thus, we are limited by the spatial resolution of the data and the lifespan of HiRISE. Decades of high-resolution monitoring may be required to confirm any secular accumulation or ablation occurring at Louth via this method.

We acquire TES temperatures for the Korolev ice mound, for both night and day. We use a set of 1-D thermal models, encompassing a range of albedo and thermal properties, and determine a best fit to the observed TES data. Differentiating between the different times of day, and what dataset is being fit, is important for selecting appropriate model properties (Table 5.2). We use the best fit to both AM and PM temperatures to determine the thermal properties of our modeled ice surface (TI derived here to be 1550 J m^{-2} K^{-1} $s^{-1/2}$).

Our atmospheric model accounts for mass transport due to forced and free convection. Rates of ice deposition and sublimation are affected by atmospheric mixing rates, and the thickness of the laminar atmospheric layer (Wallace and Sagan, 1979; Svitek and Murray, 1990). Our nominal wind speed is 3 m s^{-1}, as this value represents the average wind speed from *in situ* Viking lander measurements (Hess *et al.*, 1977). We find that the annual mass balance is sensitive to surface albedo. With the range of albedos determined from our fitting of TES data, we find a range of mass balance rates between -6 and +2 mm per Mars year at both sites (Fig. 3.10). When including our nominal albedo value (0.42) we find small values of net annual ablation, <0.5 mm of ice loss per Mars year. This range is consistent with our image analysis of the Louth ice mound.

TES data from the Korolev ice mound show systematic changes in albedo with season (Fig. 3.13). Thermal models, including a time-dependent treatment of albedo, show derived thermophysical properties similar to those found in the constant albedo case. We also found annual mass balance does not differ greatly between the two approaches.

In the current climate, it is predicted that the majority of water ice lost at lower latitudes will accumulate on the NPRC (Levrard *et al.*, 2007). It has been posited that the most recent layers in the northern polar deposits indicate present-day net accumulation (Smith *et al.*, 2016).

Icy outliers, such as those in Louth or Korolev, can record a different, yet valuable, history of Mars climate.

Chapter 4. THERMOPHYSICAL PROPERTIES OF THE NORTH POLAR RESIDUAL ICE CAP OF MARS

4.1 INTRODUCTION

The north and south polar regions of Mars host Polar Layered Deposits (NPLD and SPLD, respectively) that are sequences of water ice with varying degrees of dust (sufficient to produce visible layering in exposures), and are up to 2-3 km-thick. Together, they account for the vast majority of known water ice on Mars (Plaut *et al.*, 2007; Phillips *et al.*, 2008; Byrne, 2009). The spatial extent of the layered deposits is substantial, with the NPLD extending from the pole equatorward at all longitudes to roughly 80°N, and the SPLD extending equatorward at some longitudes to 72°S.

The PLDs are thought to have formed over the recent geologic past (~10^6-10^8 yr; Levrard *et al.*, 2007; Phillips *et al.*, 2008; Byrne, 2009; Greve *et al.*, 2010; Hvidberg *et al.*, 2012; Smith *et al.*, 2016), where climate change is driven by changes in orbital elements (Laskar *et al.*, 2004). Due to the abundance of troughs that expose sequences of the layered-deposits, the NPLD have been the primary focus for determining a climatological record. Previous studies have explored the linking of stratigraphic sequences to changes in martian orbital elements (Laskar *et al.*, 2002; Milkovich and Head, 2005; Hvidberg *et al.*, 2012; Sori *et al.*, 2014; Becerra *et al.*, 2016). However, inferring past climate from layer properties remains uncertain.

One significant difference between the two poles is the composition of ice at the surface. High-albedo residual ice caps remain at both poles after retreat of the much-larger seasonal CO_2 caps. The southern residual ice cap (SRC) is dominated by a few-meter-thick layer of CO_2 ice (Byrne and Ingersoll, 2003). The northern residual ice cap (NRC) is composed of water ice and

is on the order of a meter thick (Herkenhoff *et al.*, 2007). No perennial CO_2 ice is observed in the north.

Several studies have analyzed NRC albedo and composition (e.g., Kieffer, 1990; Langevin *et al*., 2005); yet comparably few have addressed its thermophysical state (Paige *et al*., 1994; Putzig *et al.*, 2005), and none have addressed how its properties change with depth. The present-day mass balance of the NRC is unknown (Byrne, 2009). Langevin *et al.* (2005), using near-infrared spectral measurements, concluded that the surface of the NRC is coarse-grained ice, implying older ice or net ablation. The same study also found the surface to be mostly dust-free, which is unexpected for a sublimating layer, where formation of a dust lag seems likely. Brown *et al.* (2016), also using near-infrared spectral measurements, observed transitions between accumulation and ablation as a function of season, but did not favor a particular mass-balance scenario. Smith *et al.* (2016), using sounding radar, report on a packet of ice-rich layers (on the order of 100s of meters thick), consistent with recent periods of accumulation, although this evidence cannot be used to invoke accumulation at present-day.

Study of the NRC can inform us of the potential link between climate and polar geology. The NRC interacts strongly with the current climate; e.g., supplying almost all atmospheric water vapor in northern summer (Smith *et al.* 2008). Past residual caps (now layers within the NPLD) were also likely to have been strongly influenced by past climates. Thus, understanding the current climate and NRC can unlock a larger climatic record.

Knowledge of how density varies with depth constrains environmental conditions (e.g., ice accumulation rates) that are vital to understanding how the climate affects polar stratigraphy. In terrestrial ice sheets and glaciers, the density of ice increases with depth; i.e., ice deposited at the surface, typically as highly-porous snow (>50% porosity), undergoes densification, and will

evolve towards low-porosity glacial ice. The primary physical mechanisms involved in near-surface terrestrial densification are gravity-driven compaction and temperature-gradient driven vapor transport (Herron and Langway, 1980; Arthern and Wingham, 1998).

Adapting terrestrial models of ice densification to Mars, Arthern *et al.* (2000) found that this process should occur much more slowly under drier, lower-gravity martian conditions. Unlike Earth, densification on Mars is dominated by vapor transport through the pore space in the ice. The predicted depth-density profiles of martian ice are especially sensitive to the accumulation rate. If accumulation rates are low, zero-porosity ice will be present at the surface. When accumulation rates are sufficiently high, low densities can be maintained at the surface (e.g., 360 kg m^{-3} or ~60% porosity).

The focus of this study is the physical nature of the NRC or what we consider the most-recent and potentially active layer of the NPLD. Constraining the thermophysical properties of today's NRC can inform us as to how NPLD layers form. The vertical structure of the NRC can provide potential inferences into the recent climate. Here, we investigate how relevant properties of NRC water ice (e.g., density, albedo) vary, both laterally and vertically into the subsurface.

Observed temperatures of Mars have been used previously to constrain thermophysical parameters of the near-surface (Kieffer *et al.*, 1977; Paige *et al.*, 1994; Putzig *et al.*, 2005). It is common to use thermal inertia (TI; expressed in units J m^{-2} K^{-1} $s^{-1/2}$) to describe thermophysical properties.

$$TI = \sqrt{k\rho c} \qquad (4.1)$$

Here k is the thermal conductivity (W m^{-1} K^{-1}), ρ is the bulk density (kg m^{-3}), and c is the specific heat capacity (J kg^{-1} K^{-1}). Surface temperatures are affected by a region of the subsurface approximated by the thermal skin depth, δ, in meters.

$$\delta = \frac{TI}{\rho c}\sqrt{\frac{P}{\pi}} \qquad (4.2)$$

Here P is the period of surface temperature variation (e.g., diurnal, seasonal) in seconds, assumed to be sinusoidal. Additionally, this relationship between TI and skin depth assumes a homogeneous subsurface (i.e., constant thermal properties with depth). For the properties of pure ice, and the period of one martian year, the thermal skin depth is 6.4 m. This is an upper limit as the ice we investigate is: a) not pure (e.g., has some porosity, which lowers both the thermal conductivity and density), b) may exhibit some depth dependence, c) does not have a perfectly sinusoidal forcing function, and d) the period of the observations used is less than one martian year (the effective period is closer to ¼ due to seasonal CO_2 ice). If we assume a more typical situation with an ice porosity of 50% (assuming properties described in Section 3.2.2), and consider a period of ¼ the martian year, we find a skin depth of 2.2 m.

Earlier studies have used thermal models with depth-dependent properties to explore surfaces where changes with depth are expected (Mellon *et al.*, 2004; Putzig *et al.*, 2007; Bandfield, 2007; Bandfield and Feldman, 2008; Vasavada *et al.*, 2012; Hayne *et al.*, 2017; Putzig *et al.*, 2014). We explore three relationships of depth versus density, in order to compare the near-surface structure of the NRC with predicted profiles (e.g., Arthern *et al.*, 2000).

Investigators have previously explored the thermal nature of the NRC with thermal-infrared datasets (Paige *et al.*, 1994; Putzig *et al.*, 2007; Putzig *et al.*, 2014). Paige *et al.* (1994) used Viking Infrared Thermal Mapper (IRTM) observations to derive albedo and thermal inertia simultaneously (similar to this study). They characterized the NRC as a high-albedo (>0.40), high-TI unit (>750 J m^{-2} K^{-1} $s^{-1/2}$), in contrast to the surrounding, lower-TI regolith. Paige *et al.* (1994) also show that the presence of thin (~mm) coatings of dust are consistent with IRTM observations. Putzig *et al.* (2007) prescribe albedo in their fitting approach, retrieve a TI value

for each temperature measurement and average the results. However, near-surface layering (Bandfield and Feldman, 2008; Putzig *et al.*, 2014), results in a seasonally-dependent "apparent" TI that is difficult to compare to that derived from temperature measurements acquired over a significant portion of the martian year (e.g., from Paige *et al.* (1994) and this work). Regardless, their averaged TI is consistent with the NRC as a high-TI unit. In section 4.4.1, the results of our work will be compared to these earlier studies, where applicable.

4.2 METHODS

4.2.1 *Observational Data*

Data used in this study were acquired by the Thermal Emission Spectrometer (TES) aboard Mars Global Surveyor (MGS). MGS was operational over four Mars Years (MY), specifically MY24-28 (see Piqueux *et al.*, 2015a for a description of the martian calendar). The primary science orbit of MGS was inclined approximately 93°, which resulted in high data density near the martian poles (Fig. 4.1), useful for a study of polar surface properties. Unfortunately, it also results in a region of low-to-zero data density poleward of 87°N. This region of the pole was only observed sporadically via cross-track spacecraft rolls and off-nadir pointing of TES. Because data are sparse here we, ignore this region for this work.

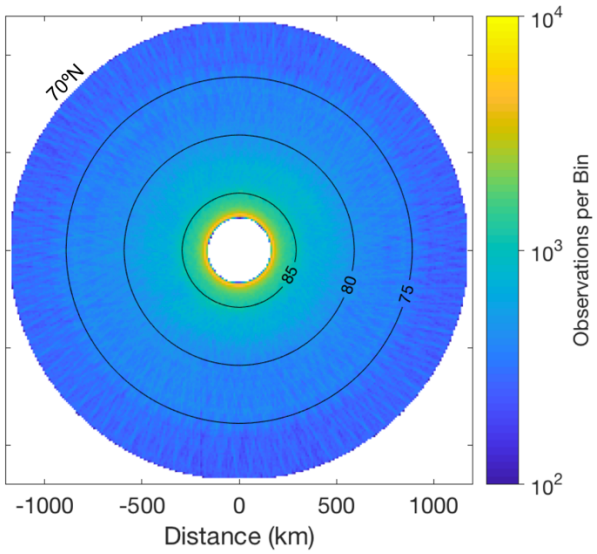

Figure 4.1. Number of observations per 10 by 10 km bin, with latitude labeled. Note the increase in density towards the pole and the logarithmic scale.

TES consists of a thermal-infrared spectrometer as well as co-aligned visible and thermal-infrared bolometers. A single TES footprint is approximately 3 by 3 km, but is lengthened by a factor of 2-3 in the along-track direction due to smearing (Christensen *et al.*, 2001; *Titus et al.*, 2001; Putzig *et al.*, 2005). We assume brightness temperatures derived from the thermal infrared bolometer represent kinetic surface temperatures, similar to previous studies using TES data to interpret thermophysical properties (Putzig *et al.*, 2005; Putzig *et al.*, 2007; Bandfield and Feldman, 2008). Data include observations poleward of 70°N, for all Mars years, and are restricted to emission angles ≤20°. Additionally, data with 'bad' nadir opacity ratings are omitted (Christensen *et al.*, 2001). Opacity ratings are sparse over the NRC due to relatively low daytime peak surface temperatures (e.g., <220 K), which are insufficient for spectrometer retrievals (Smith *et al.*, 2001). Because erroneous data are still possible over the cap we ignore brightness temperatures <160 K and >350 K. 160 K is roughly 10 K higher than the expected kinetic temperature of CO_2 ice on Mars and is chosen due to the likely heterogeneous defrosting

of CO_2-covered terrain within a TES pixel (Bapst *et al.*, 2015, Piqueux *et al.*, 2015b). Thus this step removes TES observations over surfaces, even those partially bearing seasonal CO_2 frost, from our study.

The latitudes of TES observations are converted to distance from the pole via the MATLAB Mapping Toolbox 'distance' function, which uses a martian reference ellipsoid and returns the arc length between two points (here, the observation and the pole). The data are then divided into 10 by 10 km bins. Bins with fewer than 100 observations are omitted from the results presented. Data are presented in units of distance from the pole, with 0ºE at the bottom of each figure, increasing counter-clockwise (e.g., Fig. 4.1, 4.2).

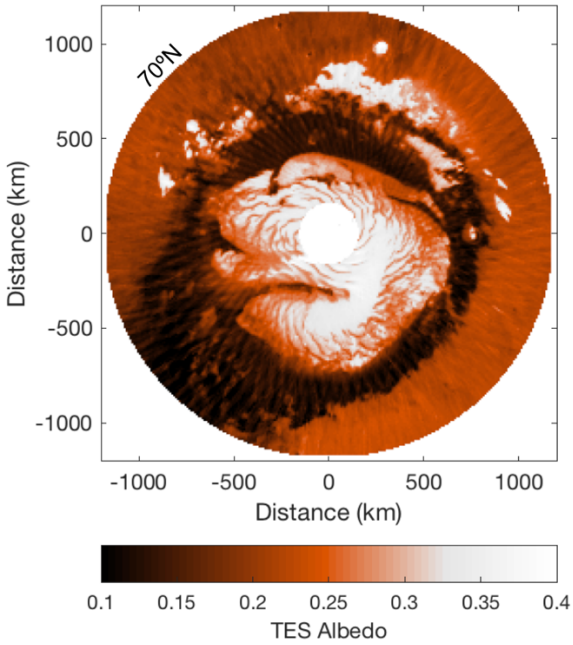

Figure 4.2. Mean TES albedo poleward of 70ºN in 10 km bins, between L_S=100-150º.

4.2.2 *Model and Fitting Procedures*

A 1-D thermal diffusion model is employed to generate surface temperatures in order to link the measured surface temperatures to near-surface thermophysical properties. The model

boundaries are controlled by insolation/emission at the surface, with conduction of heat into the subsurface, and geothermal heat (30 mW m^{-2}) at the base. Model simulations are carried out for various ranges of input parameters (Table 4.3). For simplicity, we assume a constant elevation of -3000 m to calculate CO_2 condensation temperatures, from rescaling the Viking Lander pressure measurements (Tillman *et al.*, 1993) using an atmospheric scale-height of 10.8 km. Atmospherically scattered visible light is parameterized as an additional 2% of the solar flux while downwelling infrared is an additional 4% of the noontime flux (Aharonson and Schorghofer, 2006). We refer the reader to Chapter 3 (Bapst *et al.,* 2017) for additional model description.

In all cases, the thermophysical properties of the surface materials are those of water ice of varying density. Layers of regolith at the surface are not investigated or expected over the NRC due to its high albedo (Fig. 4.2). At zero porosity (solid ice) we assume thermal properties of k=3.2 W m^{-1} K^{-1}, ρ=920 km m^{-3}, and c=1600 J kg^{-1} K^{-1}. For porous ice, density scales linearly with porosity, c remains constant, and k follows an empirical relationship based on the measured thermal conductivity-density relationship of terrestrial snowpack (described below; Calonne *et al.*, 2011). Hemispherical albedo is derived as part of the model solution and emissivity is fixed at 0.95.

How thermal conductivity changes with ice porosity is of major relevance to this work. We adopt an expression of thermal conductivity as a function of ice density (Eqn. 4.3) from a study on terrestrial snowpack (Calonne *et al.*, 2011), and modify it to match the conductivity of pure water ice at martian temperatures (i.e., k=3.2 W m^{-1} K^{-1} or TI=2200 J m^{-2} K^{-1} $s^{-1/2}$ for zero porosity; See Fig. 4.3 for examples of this relationship from various terrestrial studies).

$$k = 2.5 \times 10^{-6}\rho^2 - 1.23 \times 10^{-4}\rho + 0.024 \qquad (4.3)$$

Different models of thermal conductivity as well the temperature-dependent effects on thermal properties are explored in Section 4.4.3 but do not largely affect the results or conclusions presented using the model of Calonne *et al.* (2011).

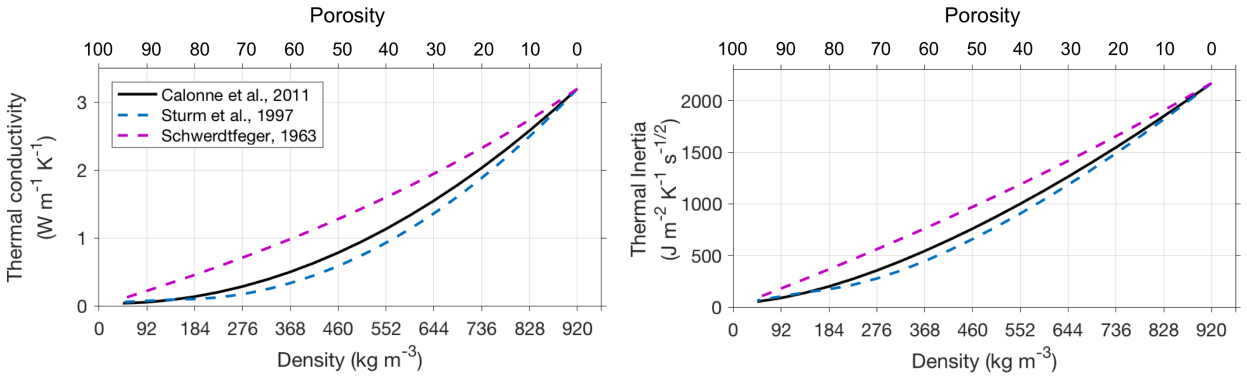

Figure 4.3. Relationships explored in this work between (left) ice conductivity and (right) thermal inertia, as a function of density/porosity of ice.

The simplest subsurface model investigated here is the vertically homogeneous case (i.e., constant thermal properties with depth), that has been used in previous derivations of thermal properties of the north polar region (Paige *et al.*, 1994; Putzig *et al.*, 2005). Porosity and albedo are the free variables in this case.

Table 4.3. Lookup-Table Elements

Parameter	**Range**
Latitude	70-90° in 0.5° increments
Albedo	0.1-0.3 in 0.05 increments 0.3-0.6 in 0.025 increments
Surface Porosity	0-0.95 in 0.05 increments (equivalent to TI range of ~50-2200 J m^{-2} K^{-1} $s^{-1/2}$)
Abrupt Change to Pure Ice (zero porosity)	Depth to pure ice of 0.01, 0.025, 0.05, 0.1, 0.2, 0.3, 0.4 ,0.5, 0.6, 0.7, 0.8, 0.9, 1, 1.5, 2, 2.5, 3, 3.5, 4, and 5 m
Exponentially Decreasing Porosity	*e*-folding depths of 0.05, 0.1, 0.2, 0.3, 0.4 ,0.5, 0.6, 0.7, 0.8, 0.9, 1, 1.25, 1.5, 2, 2.5, 3, 3.5, 4, 4.5, and 5 m
Linearly Decreasing Porosity	Porosity gradient of 0.01, 0.02, 0.03, 0.04, 0.05, 0.06, 0.07, 0.08, 0.09, 0.1, 0.2, 0.3, 0.4, 0.5, 0.6, 0.7, 0.8, 0.9, 1, and 2 m^{-1}

Three separate depth-density relationships are explored beyond the homogeneous case (Fig. 4.4; ranges explored for each case are shown in the lower section of Table 4.3). The three cases are:

1. Linearly increasing density with depth until solid ice is reached. This best resembles profiles of depth and density present in Arthern *et al.* (2000).
2. Exponentially increasing density with depth that approaches solid ice (Hayne *et al.*, 2017).
3. An abrupt increase in density to that of solid ice at a discrete depth (akin to an ice table, e.g., Mellon *et al.*, 2009; Schorghofer, 2010).

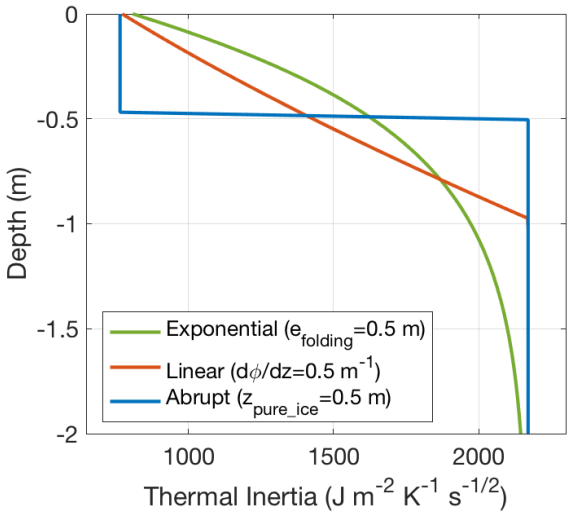

Figure 4.4. Example of depth-density relationships explored in this work. In this case, each model shown has a surface porosity of 50% (equivalent TI=760 J m^{-2} K^{-1} s$^{-1/2}$) and densifies towards zero porosity, i.e., pure ice (TI=2200 J m^{-2} K^{-1} s$^{-1/2}$).

As in Chapter 3 (Bapst *et al.*, 2017), we quantify our fit between TES-derived and model surface temperatures by calculating a reduced-χ^2 statistic (Eqn. 4.4).

$$\chi^2 = \frac{1}{(N-M)} \sum \frac{\left(T_{obs,i} - T_{model,i}\right)^2}{\gamma^2} \qquad (4.4)$$

Here, T is temperature, γ is the variance in TES observations (linearly scaled between 0.4 K for a surface temperature of 280 K and 1.5 K for a surface at 150 K; Christensen *et al.*, 2001), and N is the number of data points. M is the number of degrees of freedom, where M=2 (surface porosity and albedo) for the homogenous case and M=3 (surface porosity, its variation with depth and albedo) for the depth-varying cases. Multiple data points within each bin are included in calculating the reduced-χ^2 statistic, as opposed to the "one-point" approach, where albedo is prescribed (e.g., Putzig *et al.*, 2005).

Another major difference between the work presented here and that of previous authors is that we omit data acquired within specific seasons. We utilize a seasonal window after CO_2 ice

has largely defrosted (L_S>90º). We find it is especially important to omit spring data (L_S=0-90º) as during this time the seasonal layer of CO_2 ice is sublimating at the surface (Piqueux *et al.*, 2015b). A 1-D thermal model can only represent the surface as either CO_2 covered or not, whereas in reality the defrosting process is heterogeneous at scales smaller than TES can observe (Searls *et al.*, 2010). During spring, TES measurements may contain a mix of temperatures from CO_2-covered and CO_2-free surfaces, potentially resulting in erroneous fits between our model and the observations. We explored fitting with other seasonal windows starting at different times, i.e., L_S=0-180º. Differences in results using a seasonal window starting between L_S=90-150º were small, with our preferred choice of L_S=110º maximizing data beyond the defrosting season. The choice of end season also made little difference as long as the window includes the onset of seasonal CO_2 ice (L_S~180-200º). Based on these tests, we select a nominal window of L_S=110-270º for the derivations presented here.

4.3 RESULTS

Model fits of albedo and near-surface thermal properties are presented in this section. Because our model is designed to retrieve the thermal properties of porous ice, our results over regolith-covered surfaces are not valid and should be ignored (for clarity, bins with derived surface TI<800 J m^{-2} K^{-1} $s^{-1/2}$ and with derived albedo <0.45 are masked out in Figures 4.5 and 4.6, with the exception of albedo maps).

4.3.1 *Homogeneous Model*

Derived TI is typically high (≥1000 J m^{-2} K^{-1} $s^{-1/2}$) across the NRC and its outliers (Fig. 4.5). Model-derived albedo of the NRC is consistent with the pattern of observed albedo across the NRC (Fig. 4.2), but differs substantially in absolute value (derived albedo being ~0.2 higher).

NRC material can be effectively selected with derived albedos ≥0.50 (~5x10^4 derivations), yielding a mean NRC TI of 1044 J m^{-2} K^{-1} s$^{-1/2}$ and standard deviation of 140 J m^{-2} K^{-1} s$^{-1/2}$. The highest derived TI values are present on the edge of the NRC, near the pole at ~315ºE, and the icy outliers (i.e., lower-latitude residual ice that is discontinuous from the NRC). On the lower end of the TI range described above is southern Gemina Lingula (~150-200 km from the NRC edge), which yields TI values of 900-1000 J m^{-2} K^{-1} s$^{-1/2}$.

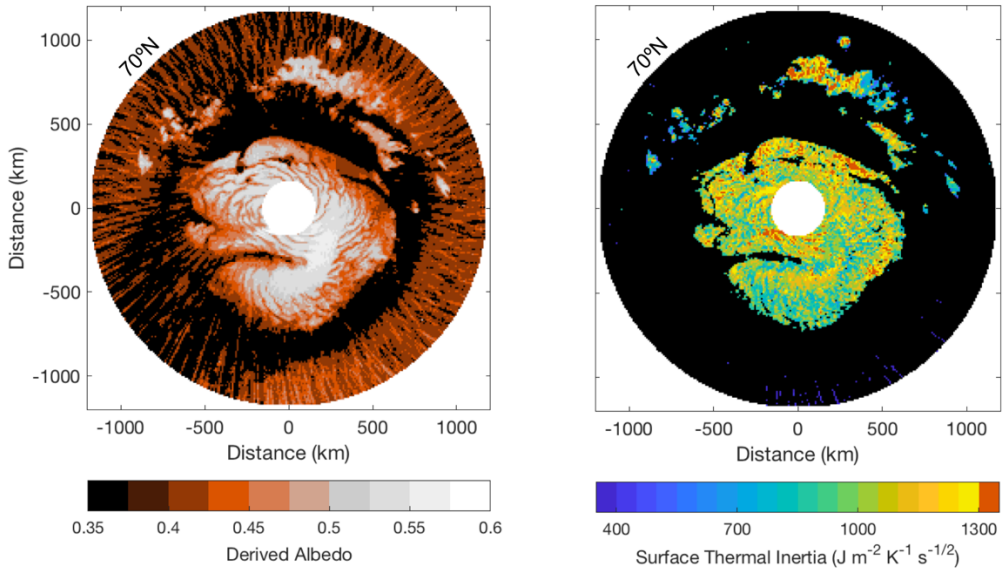

Figure 4.5. Derived albedo and TI for the north polar region of Mars above 70ºN for the homogeneous case.

4.3.2 *Depth-varying Models*

The three depth-density relationships explored (i.e., abrupt, exponential, and linear changes in thermal properties with depth; Fig. 4.4) all yield similar best-fits for derived values of albedo and surface TI (Fig. 4.6). Model-derived hemispheric albedo is similar to the homogeneous case (Fig. 4.5), and is slightly closer to the TES-derived albedo (model-derived albedo being ~0.15 higher than observations).

The spatial pattern of surface TI across the residual cap shares some similarities to the results of the homogeneous case. However, a clear delineation becomes apparent between the edge and the interior of the NRC. We find that the interior of the NRC (i.e., the highest-albedo region, i.e., >0.50) exhibits lower surface TI (~600-800 J m^{-2} K^{-1} $s^{-1/2}$) than the edges of the NRC. The higher TI regions at the edge of the NRC vary in width from 10s of km to 100s of km. These regions are characterized by lower albedo (Fig. 4.2, 4.5, 4.6) and higher surface TI (≥1000 J m^{-2} K^{-1} $s^{-1/2}$). The icy outlier regions span a range of surface TI (~700-900 J m^{-2} K^{-1} $s^{-1/2}$), and are more similar to the NRC interior than its edges (they also share a similarly high albedo).

Additionally, we explore the best-fit depth-dependent relationship for each case (Fig. 4.6, right column). For the abrupt scenario, we display the best-fit depth to pure ice. For linear and exponential cases, we plot the e-folding depth of the porosity. We find abrupt and e-folding depths correspond to the pattern observed in surface TI. Regions with higher surface TI (e.g., the NRC edge) exhibit greater depths to pure ice, in the range of 1.0-5.0 m, indicating a more homogeneous subsurface. The NRC interior (where we derive lower surface TI) exhibits more-shallow transitions to solid ice, in the range of 0.2-1.0 m. Icy outliers show the shallowest depth to pure ice (as shallow as 0.1 m).

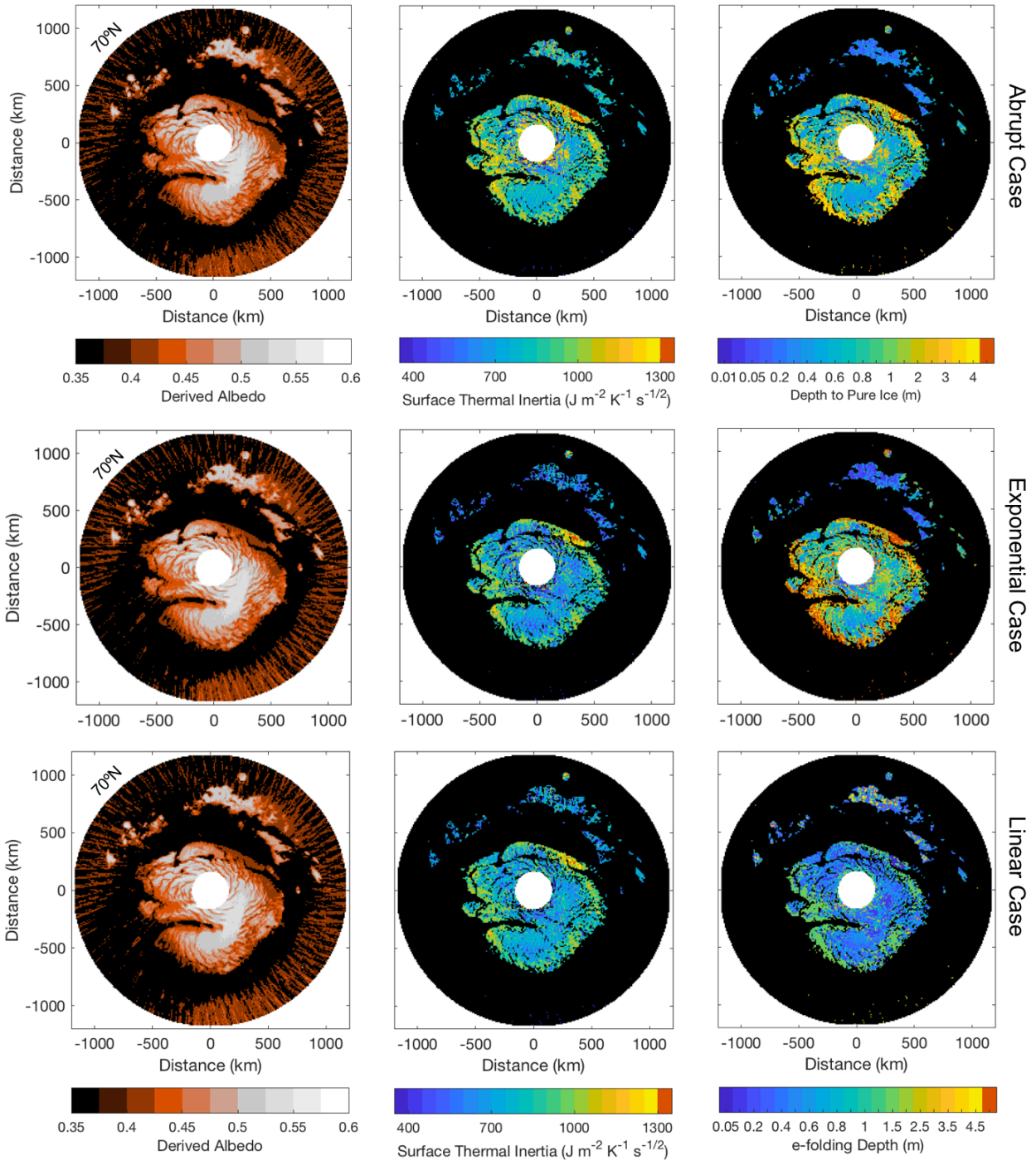

Figure 4.6. Best-fit albedo, surface TI, and depth-dependence for the three cases explored. The depth-dependence plots have low surface TI regions masked out (black). The linear case of depth-dependence is expressed as an e-folding depth for easy comparison to the exponential case.

4.3.3 *Best-fit Comparison*

We compare the reduced-χ^2 statistic for the four different cases explored: homogeneous, abrupt, exponential, and linear (Fig. 4.5). Regolith surfaces provide the worst fit to our thermal models, as expected with our primary focus on ice properties. All of the models with depth-dependent properties produce a better fit to the NRC than the homogeneous model. The largest improvement in fits is observed over the icy outliers and the edges of the cap.

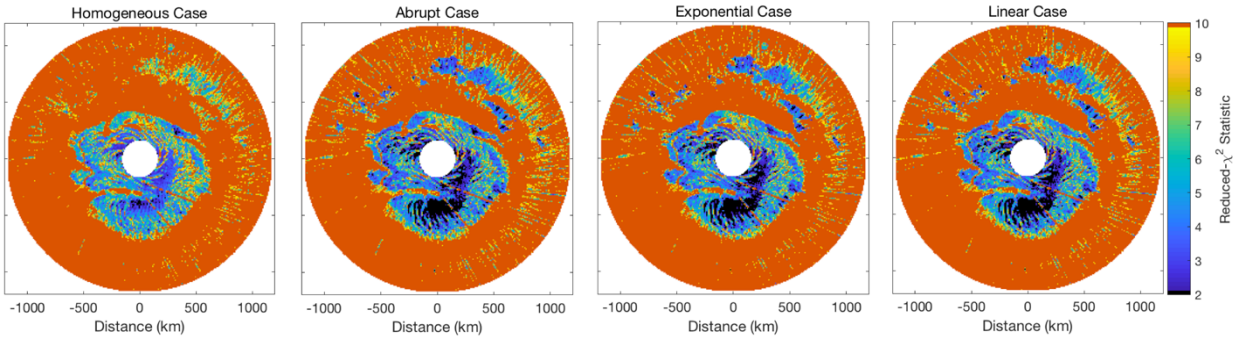

Figure 4.7. Reduced-χ^2 statistic for the four cases of depth dependence explored.

4.3.4 *Properties of Residual Ice*

To explore the vertical structure of the ice in the interior of the NRC, we choose a 10 by 10 bin region in Gemina Lingula, centered at 82.5°N, 6.5°E (~10^4 km^2), as a representative site. This region is ideal as it is devoid of polar troughs that span much of the NRC, has a relatively uniform albedo and TI in all cases explored (Fig. 4.2, 4.5, 4.6), and has low fitting errors (Fig. 4.7).

Models with depth-dependent density converge on similar solutions of surface TI and subsurface changes in density (Fig. 4.8). As stated in section 4.3.2, for regions of the NRC interior, like this one, we see relatively shallow depths to pure ice. Our best-fit for abrupt transitions to pure ice falls between 0.5-1.0 m. The most common fit for the exponential case

shows an e-folding depth of 1 m, but with some values converging on deeper skin depths (3 and 5 m). The linearly decreasing porosity case, when displayed as e-folding depth, results in all values being ≤1 m.

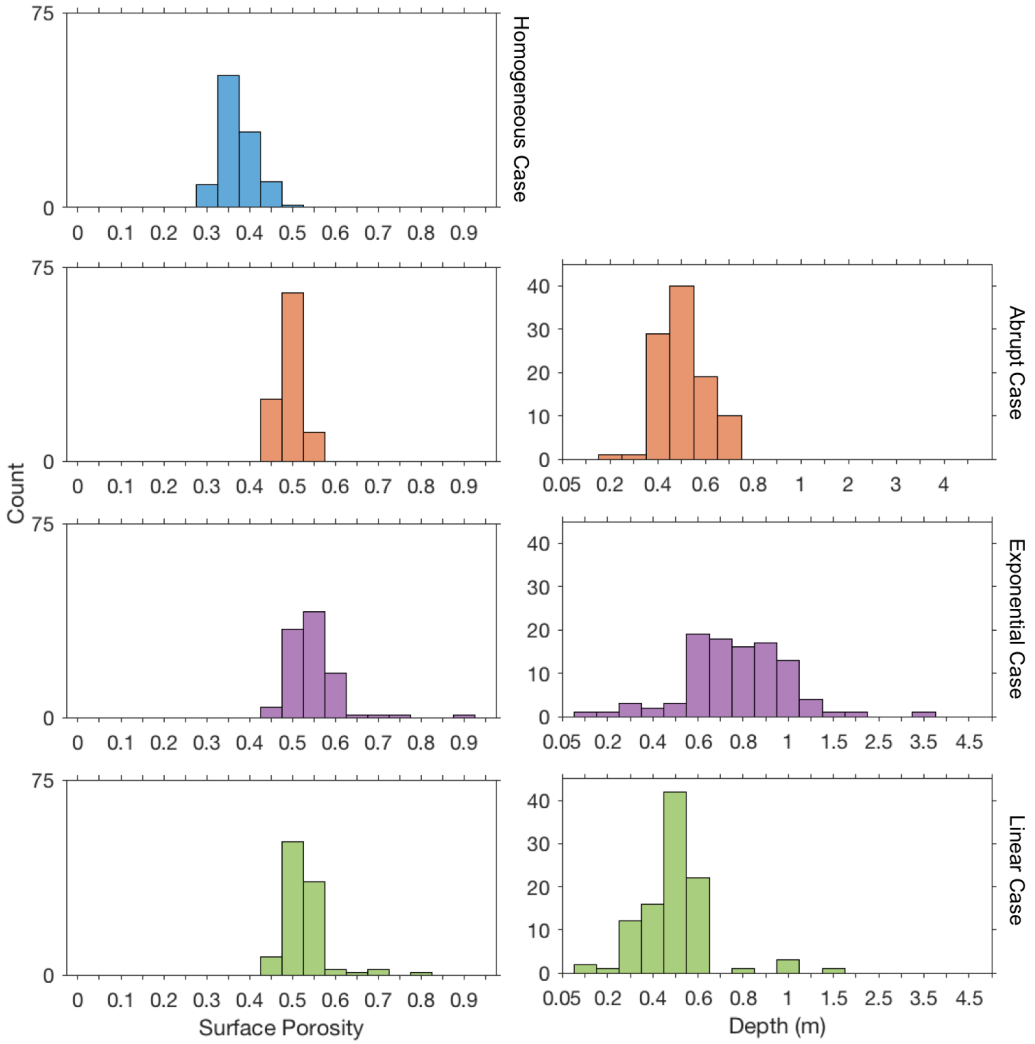

Figure 4.8. Histograms of derived surface porosity and depth-dependence values for a ~10^4 km^2 region of Gemina Lingula, representative of the NRC interior. These results indicate a lower surface TI for depth-dependent fits, as well as shallow depths (≤1 m) of porous ice transitioning to pure ice. Note the horizontal axis of depth-dependent properties for the abrupt case is slightly different due to different lookup table elements (Table 4.3).

4.4 Discussion and Conclusions

4.4.1 *Comparison to Previous Work*

Our findings for the homogeneous case (Section 4.3.1) are consistent with TI derivations made by previous authors using Viking IRTM data. Poleward of 86ºN a value of 1250±400 J m^{-2} K^{-1} $s^{-1/2}$ was derived by Paige and Ingersoll (1985), using an energy balance approach and Viking data. Using Viking IRTM-derived surface temperatures Paige *et al.* (1994) found an average TI of 1151 J m^{-2} K^{-1} $s^{-1/2}$ poleward of 86ºN. We lack TES observations poleward of 87ºN, due to the orbital inclination of MGS; however, we have ~10^3 TI derivations above 86ºN, which yield a mean value of 1090 J m^{-2} K^{-1} $s^{-1/2}$, and a standard deviation of 62 J m^{-2} K^{-1} $s^{-1/2}$ (i.e., the solution of Paige *et al.* (1994) is within 1-σ of our best fit). Paige *et al.* (1994) derive values of NRC albedo close to the measured value from TES (<0.10; see Fig. 4.2), and within 0.10 of estimates from Viking IRTM-derived albedo. A potential cause for our derived albedo being in poorer agreement with observations is our more simplistic approach to atmospheric radiation (i.e., parameterized as a fraction of the incoming insolation; see Section 4.2.2). Essentially, we may be overestimating downwelling fluxes, thus requiring more-reflective surfaces to agree with observed temperatures.

Putzig *et al.* (2007) used a one-point method for TI derivation that is susceptible to error at polar latitudes for multiple reasons. One known effect is that of a layered subsurface (Bandfield and Feldman, 2008; Putzig *et al.*, 2014) yielding seasonally-dependent TI retrievals that Putzig *et al.* (2007) averages. Putzig *et al.* (2014) explore a dune-covered region, adjacent to the NPLD, to study the effect of layering on derived TI. However, we are not aware this analysis applied to the NRC and its TI derivations. Putzig *et al.* (2007) also do not omit springtime data, and so highly variable TI derivations are averaged into their polar results. Additionally, Putzig *et*

al. (2007) prescribe model albedo using TES values, which, as we've shown, are significantly different compared to our derived values (≥0.15; Fig. 4.2, 4.5, 4.6). The effect of prescribing too low of an albedo would cause TI derivations from afternoon (~2 PM) temperatures to be erroneously large, in order for the surface to remain cool. The opposite is true for data acquired at ~2 AM, where prescribing a low albedo requires effective cooling in the AM (i.e., low TI), thus leading to underestimates of TI. Despite these differences, surface TI derived by Putzig *et al.* (2007) over the NRC is consistent with our results, albeit with larger scatter.

4.4.2 *Spatial Heterogeneity of the North Residual Cap*

We interpret the derived properties of Gemina Lingula as the consequence of recently accumulating ice, where the material being deposited at the surface is relatively porous (40-60%), and densifies with depth (many solutions reaching properties of pure ice in ~1 m; Fig. 4.8). This scenario may be representative of the NRC interior. If water ice is accumulating at a sufficient rate, high porosities can be maintained at and near the surface (Arthern *et al.*, 2000). The derived depth-density gradients derived here are much steeper than predictions from Arthern *et al.* (2000) and a full interpretation of these results requires modeling of densification rates.

Along the edge of the NRC, we derive denser ice properties (20-40% surface porosity), relative to the NRC interior. Densified ice might be present near the surface for a few reasons.

One possible explanation is that the ice is accumulating slowly, such that porosity is initially low or cannot be maintained (Arthern *et al.*, 2000). However, the edge of the residual cap also has a systematically lower albedo (Fig. 4.2). It is unclear why accumulating ice would be contaminated by dust in only this region. Very small mixing fractions of dust at the surface, consistent with Langevin *et al.* (2005), could be responsible for the lower albedo (Warren, 1982; Kieffer, 1990).

Another possibility is that this is older ice and has undergone some degree of densification. In this scenario, this older ice is being exhumed and is retreating, with some mechanism (e.g., aeolian transport; Smith *et al.*, 2013) acting to remove dust lags from its surface. We favor this explanation, i.e., the NRC edge is densified ice from a more-ancient climate. The notion that ice at the surface can be simultaneously accumulating and retreating, as a function of location, can complicate the interpretation of NPLD layers. It may also help explain the higher density of NPLD troughs at lower latitudes. Troughs, which are tied to sublimation and aeolian processes (Smith and Holt, 2010; Smith *et al.*, 2013) may be aided in initiation due to increased dust content at surface (i.e., lithic material liberated via sublimation of retreating ice).

One particular region of the residual cap edge shows some of the highest derived TI, located at approximately 83°N, 125°E. Unlike the edge of the residual cap, this region also appears to have an anomalously high TI in the homogeneous solution. All cases suggest low surface porosities of ~20% and TI≥1500 J m^{-2} K^{-1} $s^{-1/2}$. This region exhibits large e-folding/abrupt depths, suggesting a homogeneous layer. Derived albedo is relatively low suggesting significant contamination by dust at the surface, but with the high TI signal remaining intact. We interpret this region of the NRC as comprised of older ice than what is typically at the surface around its edge. This ice has almost fully densified but is being exhumed by simultaneous retreat and removal of lithic material via wind.

4.4.3 *Ice Conductivity Models and Temperature Dependency*

The relationship between the density of water ice in the NRC and its conductivity is uncertain for a number of reasons, many relating to the microstructure of the ice (e.g., pore radius, grain size, degree of roundness, etc.; see Sturm *et al.*, 1997). Because we lack *in-situ*

measurements of these properties on Mars we explore, in addition to the model by Calonne *et al*. (2011), two additional models for ice conductivity: Sturm *et al*. (1997) and Schwerdtfeger (1963) (see Fig. 4.3). The models tested do not result in appreciable differences in derived properties (Fig. 4.9). Thus, our results and interpretations from Section 3 are not particularly sensitive to alternative models of thermal conductivity for porous water ice.

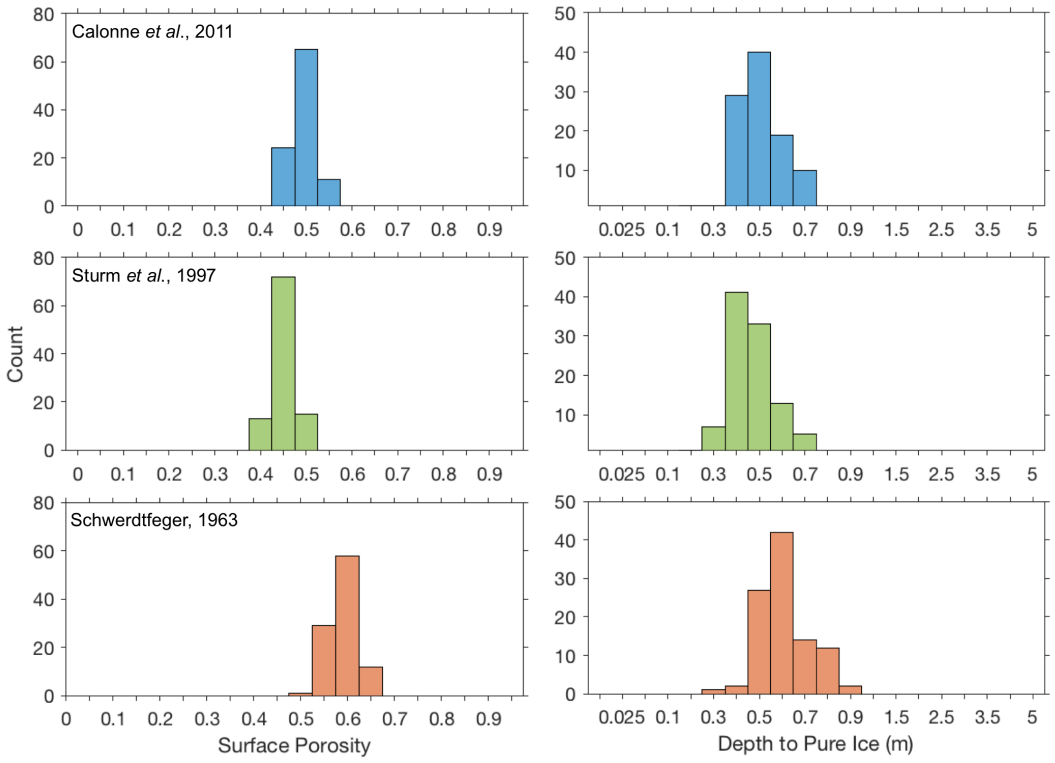

Figure 4.9. Histograms of derived surface porosity and depth to zero-porosity ice (abrupt change with depth) for the three models of ice conductivity explored (see Fig. 4.3). The region sampled is the same as in Figure 4.8.

The temperature-dependent effects on ice thermal properties are well known and used in terrestrial glaciology (Yen, 1981; Cuffey and Patterson, 2010). Here we consider the effect of temperature on thermal conductivity, k, and heat capacity, c (after Cuffey and Patterson, 2010).

$$c = 152.5 + 7.122T \qquad (4.5)$$

$$k = 9.828 \exp\left(-5.7 \times 10^{-3} T\right) \qquad (4.6)$$

Uncertainty in ice microstructure will have a major impact as these properties are valid for only zero-porosity water ice. The addition of porosity and interstitial gases of varying composition, density and temperature (e.g., the martian atmosphere) into the pore space can significantly change the effective conductivity (Mellon *et al.*, 1993; Sturm *et al.*, 1997). Here, we determine how the temperature-dependence of the solid conductivity and heat capacity affect our results. Because the temperature-dependent model is significantly slower, computationally, only a single bin (centered at the same location as Fig. 4.8, 4.9) is tested (Table 4.4). In general, the temperature-dependence has a small effect on the derived results. The largest influence appears to be on the depth to pure ice, however the value remains in the range resulting from different conductivity models.

Table 4.4. Effect of Temperature-Dependent Properties on Derived Parameters

Derived Property	**Temperature Independent**	**Temperature Dependent**
Porosity	0.45	0.5
Albedo	0.5	0.525
Depth to Pure Ice (m)	0.6	0.4
Reduced χ^2	1.23	1.44

4.4.4 *Conclusions*

In the work presented, we investigated the thermophysical nature of the upper-most layer of the NPLD, the NRC, with emphasis on depth-density relationships within the subsurface (depths of a few meters). We find a strong depth dependence associated with the brightest

regions of the NRC interior (i.e., a more-porous layer of ice overlying a denser layer). We interpret this as a result of recent accumulation. This change in density occurs typically within 1 m of the surface. At the edges of the NRC we derive a more-homogeneous subsurface that is denser, and likely older, ice. We interpret this ice as having recently undergone ablation, which is consistent with, and may help explain, its lower albedo.

Chapter 5. CONCLUSIONS

I have presented three chapters concerning water ice and its presence on the martian surface, thus providing insight into the recent climate and the present-day water cycle. In the first chapter, I showed a stark difference between north and south hemispheres, with respect to the presence of seasonal water ice. The northern hemisphere of Mars shows clear evidence of seasonal water ice, while the southern hemisphere, which is known to have a drier atmosphere, did not, during the respective cold seasons. The second chapter included models of mass balance of the northern icy outliers, in order to understand both annual and seasonal trends in accumulation. At present, any secular changes in outlier size are unresolvable (<0.25 m) over multiple Mars years via HiRISE, which is consistent with the near-zero net mass balance that we simulate. The third chapter focused on deriving thermal properties of the north polar residual cap. Inhomogeneous depth-density relationships were found to best-replicate observed temperatures. The results imply recent accumulation has occurred where the albedo is largest (residual cap interior), and that the edges of the residual cap may be actively ablating.

Much of this work uses data from the TES instrument described in the presented chapters. Beyond TES, the Thermal Emission Imaging System (THEMIS) is an imaging spectrometer flown on the 2001 Mars Odyssey mission (Christensen *et al*., 2004). Its absolute accuracy is worse than TES by a factor ≥5 (Ferguson *et al*., 2006), but there is more than an order of magnitude improvement in spatial resolution between the two, where THEMIS infrared images have a spatial resolution of ~100 m. Careful treatment of THEMIS data may make a higher-resolution study of thermophysical properties at the north pole worthwhile (improving upon chapter 4). In particular, regions of interest where we observed thermal inertia anomalies make good candidates for follow-up with THEMIS.

To better understand the ice deposits on the surface of Mars, I will recommend a few instruments as examples that would generate great scientific return. This could also be aided by a shallow penetrating radar which provides sub-meter information about the physical nature of the residual cap. Several basic gaps exist in our knowledge of near-surface conditions especially wind speed and the vertical distribution of water vapor. A meteorological station on the residual cap would be ideal to constrain these, but more meteorological measurements in the polar region, in general, could assist a better understanding of the water cycle. Technology to survive the polar night and the seasonal CO_2 cap would be essential. Observed changes in albedo remain poorly quantified and largely unexplained (see Section 3.4.3). A medium-resolution visible spectrometer that could accurately measure reflectance at high incidence angles (i.e. low signals), and multiple times of day (to encompass many phase angles), would be ideal for determining the cause(s) of albedo change. Lastly, a higher-spatial-resolution neutron spectrometer, to improve upon the dataset of the Mars Odyssey Neutron Spectrometer, would be of value. This instrument is useful for studying subsurface water ice and could more sharply identify the equatorward boundary of shallow ground ice (Mellon *et al*., 2004). It could also help characterized buried ice sheets in the mid-latitudes (Bramson *et al*., 2015; Stuurman *et al*., 2016).

5.1 Astrobiological Relevance

The astrobiological potential of Mars is limited by liquid water. Temperatures in the tropics can exceed 273 K very near the surface, and in regions where boiling is mitigated by higher atmospheric pressures (Hecht, 2002). However, sources of water (i.e., ice) are only present beneath the surface in the mid-latitudes, and on the surface at polar latitudes, where temperatures remain low (<200-220 K; Mellon *et al*., 1993). There is no perfect Earth analog for

the low humidity and low temperatures of present-day Mars, although parts of the Antarctic Dry Valleys have shallow ground ice similar to its higher latitudes (Mellon *et al*., 2008).

Chapter 2 focuses on the seasonal occurrence of water ice on the surface, which was primarily limited to the northern hemisphere at mid-to-high latitudes. Because seasonal water ice is only present at low temperatures (Schorghofer and Aharonson, 2005; Bapst *et al*., 2015) its astrobiological potential is low. Additionally, melting of seasonal frost faces the same challenges as other ice on Mars (Ingersoll, 1970).

Chapter 3 is a study of the most-equatorward examples of perennial water ice deposits, potentially the best candidates for habitable regions at present. Regardless of their relatively low-latitude location our thermal models suggest temperatures of the ice at these locations does not reach much above ~220 K. During different orbital configurations, these ice deposits could experience temperatures >220 K, however, it appears that ice at the surface of Mars strongly follows equilibrium with the current climate. Water ice at high temperatures (i.e., near the melting point) would have to avoid sublimation over long periods, and is therefore unlikely (Ingersoll, 1970; Hecht, 2002).

In chapter 4, the thermal properties of the north polar residual cap are investigated. We find strong evidence for a recent layer of accumulation on the north residual cap, and argue that its edges are currently or recently were in a state of retreat. The temperature range of the surface of the polar deposits is well below the melting point of water (<220 K). Additionally, the surface of the residual cap is covered by seasonal CO_2 ice almost ¾ of the martian year, which necessarily enforces a surface temperature of ~150K.

The work presented here improves our understanding of martian sinks and sources of water over different timescales. We have used a combination of observations and models to

constrain fluxes of water within the climate system. This is important for understanding the global water cycle, and narrows potentially-habitable regions of Mars. More directly, my work provides insight into where ice has occurred or where it is likely to occur again. Conditions in these other epochs may have implications for habitability. Although temperatures of the ice studied here do not exceed the melting point, it is possible during different epochs that transient conditions, where melting occurs, would be possible. The martian atmosphere acts as a conduit for water to be transported. Melting water ice at the surface from sunlight is difficult-to-impossible (Ingersoll, 1970), and surface ice is only located near the poles where temperatures are sufficiently low. Thus, the most likely setting for sustained liquid water on geologic timescales involves melting in the deep subsurface (Clifford, 1993).

BIBLIOGRAPHY

Aharonson, O., Schorghofer, N., 2006. Subsurface ice on Mars with rough topography. J. Geophys. Res. E Planets 111, 1–10. doi:10.1029/2005JE002636

Appéré, T., Schmitt, B., Langevin, Y., Douté, S., Pommerol, A., Forget, F., Spiga, A., Gondet, B., Bibring, J.P., 2011. Winter and spring evolution of northern seasonal deposits on Mars from OMEGA on Mars Express. J. Geophys. Res. E Planets 116, E05001. doi:10.1029/2010JE003762

Armstrong, J.C., Nielson, S.K., Titus, T.N., 2007. Survey of TES high albedo events in Mars' northern polar craters. Geophys. Res. Lett. 34, L01202. doi:10.1029/2006GL027960

Armstrong, J.C., Titus, T.N., Kieffer, H.H., 2005. Evidence for subsurface water ice in Korolev crater, Mars. Icarus 174, 360–372. doi:10.1016/j.icarus.2004.10.032

Arthern, R.J., Winebrenner, D.P., Waddington, E.D., 2000. Densification of Water Ice Deposits on the Residual North Polar Cap of Mars. Icarus 144, 367–381. doi:10.1006/icar.1999.6308

Arthern, R.J., Wingham, D.J., 1998. The Natural Fluctuations of Firn Densification and Their Effect on the Geodetic Determination of Ice Sheet Mass Balance. Clim. Change 40, 605–624. doi:10.1023/A:1005320713306

Bandfield, J.L., 2007. High-resolution subsurface water-ice distributions on Mars. Nature 447, 64–67. doi:10.1038/nature05781

Bandfield, J.L., Feldman, W.C., 2008. Martian high latitude permafrost depth and surface cover thermal inertia distributions. J. Geophys. Res. E Planets 113, E08001. doi:10.1029/2007JE003007

Bapst, J., Bandfield, J.L., Wood, S.E., 2015. Hemispheric asymmetry in martian seasonal surface water ice from MGS TES. Icarus 260, 396–408. doi:10.1016/j.icarus.2015.07.025

Bapst, J., Byrne, S., Brown, A.J., 2017. On the icy edge at Louth and Korolev craters. Icarus. doi:10.1016/j.icarus.2017.10.004

Bass, D.S., Herkenhoff, K.E., Paige, D. A., 2000. Variability of Mars' North Polar Water Ice Cap: I. Analysis of Mariner 9 and Viking Orbiter Imaging Data. Icarus 144, 382–396. doi:10.1006/icar.1999.6300

Becerra, P., Byrne, S., Sori, M.M., Sutton, S., Herkenhoff, K.E., 2016. Stratigraphy of the north polar layered deposits of Mars from high-resolution topography. J. Geophys. Res. Planets 121, 1445–1471. doi:10.1002/2015JE004992

Benson, J.L., Kass, D.M., Kleinböhl, A., 2011. Mars' north polar hood as observed by the Mars Climate Sounder. J. Geophys. Res. E Planets 116, E03008. doi:10.1029/2010JE003693

Bramson, A.M., Byrne, S., Putzig, N.E., Sutton, S., Plaut, J.J., Brothers, T.C., Holt, J.W., 2015. Widespread excess ice in Arcadia Planitia, Mars. Geophys. Res. Lett. 42, 6566–6574. doi:10.1002/2015GL064844

Bramson, A.M., Byrne, S., Bapst, J., 2017. Preservation of Mid-Latitude Ice Sheets on Mars. J. Geophys. Res. Planets 1–17. doi:10.1002/2017JE005357

Brothers, T.C., Holt, J.W., 2016. Three-dimensional structure and origin of a 1.8 km thick ice dome within Korolev Crater, Mars. Geophys. Res. Lett. 43, 1443–1449. doi:10.1002/2015GL066440

Brown, A.J., Bapst, J., Byrne, S., 2017. Louth Crater and Depositional Mode Flips. 48th Lunar Planet. Sci. Conf. held 20-24 March 2017, Woodlands, Texas. LPI Contrib. No. 1964, id.2672 48.

Brown, A.J., Byrne, S., Tornabene, L.L., Roush, T., 2008. Louth crater: Evolution of a layered water ice mound. Icarus 196, 433–445. doi:10.1016/j.icarus.2007.11.023

Brown, A.J., Calvin, W.M., Becerra, P., Byrne, S., 2016. Martian north polar cap summer water cycle. Icarus 277, 401–415. doi:10.1016/j.icarus.2016.05.007

Brown, A.J., Calvin, W.M., Murchie, S.L., 2012. Compact Reconnaissance Imaging Spectrometer for Mars (CRISM) north polar springtime recession mapping: First 3 Mars years of observations. J. Geophys. Res. E Planets 117, 1–19. doi:10.1029/2012JE004113

Byrne, S., 2009. The Polar Deposits of Mars. Annu. Rev. Earth Planet. Sci. 37, 535–560. doi:10.1146/annurev.earth.031208.100101

Byrne, S., Dundas, C.M., Kennedy, M.R., Mellon, M.T., McEwen, A.S., Cull, S.C., Daubar, I.J., Shean, D.E., Seelos, K.D., Murchie, S.L., Cantor, B. a, Arvidson, R.E., Edgett, K.S., Reufer, A., Thomas, N., Harrison, T.N., Posiolova, L. V, Seelos, F.P., 2009. Distribution of mid-latitude ground ice on mars from new impact craters. Science 325, 1674–1676. doi:10.1126/science.1175307

Byrne, S., Ingersoll, A.P., 2003. A sublimation model for Martian south polar ice features. Science 299, 1051–1053. doi:10.1126/science.1080148

Calonne, N., Flin, F., Morin, S., Lesaffre, B., Du Roscoat, S.R., Geindreau, C., 2011. Numerical and experimental investigations of the effective thermal conductivity of snow. Geophys. Res. Lett. 38. doi:10.1029/2011GL049234

Cantor, B. A., James, P.B., Calvin, W.M., 2010. MARCI and MOC observations of the atmosphere and surface cap in the north polar region of Mars. Icarus 208, 61–81. doi:10.1016/j.icarus.2010.01.032

Carrozzo, F.G., Bellucci, G., Altieri, F., D'Aversa, E., Bibring, J.P., 2009. Mapping of water frost and ice at low latitudes on Mars. Icarus 203, 406–420. doi:10.1016/j.icarus.2009.05.020

Chamberlain, M. A., Boynton, W. V., 2007. Response of Martian ground ice to orbit-induced climate change. J. Geophys. Res. E Planets 112, 1–20. doi:10.1029/2006JE002801

Chittenden, J., Chevrier, V., Roe, L., Bryson, K., Pilgrim, R., Sears, D., 2008. Experimental study of the effect of wind on the stability of water ice on Mars. Icarus 196, 477–487. doi:10.1016/j.icarus.2008.01.016

Christensen, P.R., Bandfield, J.L., Hamilton, V.E., Ruff, S.W., Kieffer, H.H., Titus, T.N., Malin, M.C., Morris, R. V., Lane, M.D., Clark, R.L., Jakosky, B.M., Mellon, M.T., Pearl, J.C., Conrath, B.J., Smith, M.D., Clancy, R.T., Kuzmin, R.O., Roush, T., Mehall, G.L., Gorelick, N., Bender, K., Murray, K., Dason, S., Greene, E., Silverman, S., Greenfield, M., 2001. Mars Global Surveyor Thermal Emission Spectrometer experiment: Investigation description and surface science results. J. Geophys. Res. Planets 106, 23823–23871. doi:10.1029/2000JE001370

Christensen, P.R., Jakosky, B.M., Kieffer, H.H., Malin, M.C., McSween, Jr., H.Y., Nealson, K., Mehall, G.L., Silverman, S.H., Ferry, S., Caplinger, M., Ravine, M., 2004. The Thermal Emission Imaging System (THEMIS) for the Mars 2001 Odyssey Mission. Space Sci. Rev. 110, 85–130. doi:10.1023/B:SPAC.0000021008.16305.94

Clancy, R.T., Grossman, A.W., Wolff, M.J., James, P.B., Rudy, D.J., Billawala, Y.N., Sandor, B.J., Lee, S.W., Muhleman, D.O., 1996. Water vapor saturation at low altitudes around Mars aphelion: A key to Mars climate? Icarus 122, 36–62. doi:10.1006/icar.1996.0108

Clifford, S.M., 1993. A Model for the Hydrologic and Climatic Behavior of Water on Mars. J. Geophys. Res. 98, 10973–11016. doi:10.1029/93JE00225

Conway, S.J., Hovius, N., Barnie, T., Besserer, J., Le Mouélic, S., Orosei, R., Read, N.A., 2012. Climate-driven deposition of water ice and the formation of mounds in craters in Mars' north polar region. Icarus 220, 174–193. doi:10.1016/j.icarus.2012.04.021

Cull, S., Arvidson, R.E., Morris, R. V., Wolff, M., Mellon, M.T., Lemmon, M.T., 2010. Seasonal ice cycle at the Mars Phoenix landing site: 2. Postlanding CRISM and ground observations. J. Geophys. Res. E Planets 115, E00E19. doi:10.1029/2009JE003410

Cuffey, K.M., Paterson, W.S.B., 2010. Physics of Glaciers, Fourth Edition, The Physics of Glaciers.

Dundas, C.M., Byrne, S., 2010. Modeling sublimation of ice exposed by new impacts in the martian mid-latitudes. Icarus 206, 716–728. doi:10.1016/j.icarus.2009.09.007

Dundas, C.M., Byrne, S., McEwen, A.S., Mellon, M.T., Kennedy, M.R., Daubar, I.J., Saper, L., 2014. HiRISE observations of new impact craters exposing Martian ground ice. J. Geophys. Res. E Planets 119, 109–127. doi:10.1002/2013JE004482

Edwards, C.S., Bandfield, J.L., Christensen, P.R., Fergason, R.L., 2009. Global distribution of bedrock exposures on Mars using THEMIS high-resolution thermal inertia. J. Geophys. Res. E Planets 114, 1–18. doi:10.1029/2009JE003363

Feldman, W.C., Boynton, W. V, Tokar, R.L., Prettyman, T.H., Gasnault, O., Squyres, S.W., Elphic, R.C., Lawrence, D.J., Lawson, S.L., Maurice, S., McKinney, G.W., Moore, K.R., Reedy, R.C., 2002. Global distribution of neutrons from Mars: Results from Mars Odyssey. Science 297, 75–78. doi:10.1126/science.1073541

Fergason, R.L., Christensen, P.R., Kieffer, H.H., 2006. High-resolution thermal inertia derived from the Thermal Emission Imaging System (THEMIS): Thermal model and applications. J. Geophys. Res. Planets 111, n/a-n/a. doi:10.1029/2006JE002735

Forget, F., Haberle, K.M., Montmessin, F., Levrard, B., Head, J.W., 2006. Formation of glaciers on Mars by atmospheric precipitation at high obliquity. Science 311, 368–371. doi:10.1126/science.1120335

Greve, R., Grieger, B., Stenzel, O.J., 2010. MAIC-2, a latitudinal model for the Martian surface temperature, atmospheric water transport and surface glaciation. Planet. Space Sci. 58, 931–940. doi:10.1016/j.pss.2010.03.002

Haberle, R.M., Houben, H.C., Hertenstein, R., Herdtle, T., 1993. A boundary-layer model for Mars - Comparison with Viking lander and entry data. J. Atmos. Sci. doi:10.1175/1520-0469(1993)050<1544:ABLMFM>2.0.CO;2

Hayne, P.O., Bandfield, J.L., Siegler, M.A., Vasavada, A.R., Ghent, R.R., Williams, J.-P., Greenhagen, B.T., Aharonson, O., Elder, C.M., Lucey, P.G., Paige, D.A., 2017. Global Regolith Thermophysical Properties of the Moon From the Diviner Lunar Radiometer Experiment. J. Geophys. Res. Planets. doi:10.1002/2017JE005387

Head, J.W., Marchant, D.R., 2003. Cold-based mountain glaciers on Mars: Western Arsia Mons. Geology 31, 641–644.

Head, J.W., Mustard, J.F., Kreslavsky, M. A, Milliken, R.E., Marchant, D.R., 2003. Recent ice ages on Mars. Nature 426, 797–802. doi:10.1038/nature02114

Hecht, M.H., 2002. Metastability of liquid water on Mars. Icarus 156, 373–386. doi:10.1006/icar.2001.6794

Herkenhoff, K.E., Byrne, S., Russell, P.S., Fishbaugh, K.E., McEwen, A.S., 2007. Meter-scale morphology of the north polar region of mars. Science 317, 1711–1715. doi:10.1126/science.1143544

Herron, M.M., Langway, C.C., 1980. Firn Densification: An Empirical Model. J. Glaciol. 25, 373–385. doi:10.3189/S0022143000015239

Hess, S.L., Henry, R.M., Leovy, C.B., Ryan, J.A., Tillman, J.E., 1977. Meteorological results from the surface of Mars: Viking 1 and 2. J. Geophys. Res. 82, 4559–4574. doi:10.1029/JS082i028p04559

Holstein-Rathlou, C., Gunnlaugsson, H.P., Merrison, J.P., Bean, K.M., Cantor, B.A., Davis, J.A., Davy, R., Drake, N.B., Ellehoj, M.D., Goetz, W., Hviid, S.F., Lange, C.F., Larsen, S.E., Lemmon, M.T., Madsen, M.B., Malin, M., Moores, J.E., Nørnberg, P., Smith, P., Tamppari, L.K., Taylor, P.A., 2010. Winds at the phoenix landing site. J. Geophys. Res. E Planets 115, E00E18. doi:10.1029/2009JE003411

Holt, J.W., Safaeinili, A., Plaut, J.J., Head, J.W., Phillips, R.J., Seu, R., Kempf, S.D., Choudhary, P., Young, D.A., Putzig, N.E., Biccari, D., Gim, Y., 2008. Radar sounding evidence for buried glaciers in the southern mid-latitudes of Mars. Science 322, 1235–1238. doi:10.1126/science.1164246

Houben, H., Haberle, R.M., Young, R.E., Zent, A.P., 1997. Modeling the Martian seasonal water cycle. J. Geophys. Res. 102, 9069. doi:10.1029/97JE00046

Hudson, T.L., Aharonson, O., Schorghofer, N., Farmer, C.B., Hecht, M.H., Bridges, N.T., 2007. Water vapor diffusion in Mars subsurface environments. J. Geophys. Res. E Planets 112, 1–27. doi:10.1029/2006JE002815

Hvidberg, C.S., Fishbaugh, K.E., Winstrup, M., Svensson, A., Byrne, S., Herkenhoff, K.E., 2012. Reading the climate record of the martian polar layered deposits. Icarus 221, 405–419. doi:10.1016/j.icarus.2012.08.009

Ingersoll, A.P., 1970. Mars: Occurrence of Liquid Water. Science 168, 972–973. doi:10.1126/science.168.3934.972

Jakosky, B.M., Farmer, C.B., 1982. The seasonal and global behavior of water vapor in the Mars atmosphere - Complete global results of the Viking atmospheric water detector experiment. J. Geophys. Res. 87, 2999–3019. doi:10.1029/JB087iB04p02999

Jones, K.L., Arvidson, R.E., Guinness, E.A., Bragg, S.L., Wall, S.D., Carlston, C.E., Pidek, D.G., 1979. One Mars year: viking lander imaging observations. Science 204, 799–806. doi:10.1126/science.204.4395.799

Kieffer, H.H., 1990. H2O grain size and the amount of dust in Mars' Residual north polar cap. J. Geophys. Res. 95, 1481. doi:10.1029/JB095iB02p01481

Kieffer, H.H., Martin, T.Z., Peterfreund, A.R., Jakosky, B.M., Miner, E.D., Palluconi, F.D., 1977. Thermal and albedo mapping of Mars during the Viking primary mission. J. Geophys. Res. 82, 4249–4291. doi:10.1029/JS082i028p04249

Kieffer, H.H., Titus, T.N., 2001. TES mapping of Mars' north seasonal cap. Icarus 154, 162–180. doi:10.1006/icar.2001.6670

Kieffer, H.H., Titus, T.N., Mullins, K.F., Christensen, P.R., 2000. Mars south polar spring and summer behavior observed by TES: Seasonal cap evolution controlled by frost grain size. J. Geophys. Res. 105, 9653. doi:10.1029/1999JE001136

Kreslavsky, M. A., Head, J.W., 2002. Mars: Nature and evolution of young latitude-dependent water-ice-rich mantle. Geophys. Res. Lett. 29, 14-1-14–4. doi:10.1029/2002GL015392

Kreslavsky, M.A., Head, J.W., 2000. Kilometer-scale roughness of Mars: Results from MOLA data analysis. J. Geophys. Res. Planets 105, 26695–26711. doi:10.1029/2000JE001259

Landis, M.E., Byrne, S., Daubar, I.J., Herkenhoff, K.E., Dundas, C.M., 2016. A revised surface age for the North Polar Layered Deposits of Mars. Geophys. Res. Lett. 43, 3060–3068. doi:10.1002/2016GL068434

Langevin, Y., Poulet, F., Bibring, J.P., Schmitt, B., Douté, S., Gondet, B., 2005. Summer evolution of the north polar cap of Mars as observed by OMEGA/Mars express. Science 307, 1581–1584. doi:10.1126/science.1109438

Laskar, J., Correia, A.C.M., Gastineau, M., Joutel, F., Levrard, B., Robutel, P., 2004. Long term evolution and chaotic diffusion of the insolation quantities of Mars. Icarus 170, 343–364. doi:10.1016/j.icarus.2004.04.005

Laskar, J., Levrard, B., Mustard, J.F., 2002. Orbital forcing of the martian polar layered deposits. Nature 419, 375–377. doi:10.1038/nature01066

Leighton, R.B., Murray, B.C., 1966. Behavior of carbon dioxide and other volatiles on Mars. Science 153, 136–144. doi:10.1126/science.153.3732.136

Levrard, B., Forget, F., Montmessin, F., Laskar, J., 2007. Recent formation and evolution of northern Martian polar layered deposits as inferred from a Global Climate Model. J. Geophys. Res. E Planets 112, 1–18. doi:10.1029/2006JE002772

Lewis, S.R., Collins, M., Read, P.L., Forget, F., Hourdin, F., Fournier, R., Hourdin, C., Talagrand, O., Huot, J.-P., 1999. A climate database for Mars. J. Geophys. Res. Planets 104, 24177–24194. doi:10.1029/1999JE001024

McEwen, A.S., Eliason, E.M., Bergstrom, J.W., Bridges, N.T., Hansen, C.J., Delamere, W.A., Grant, J. A., Gulick, V.C., Herkenhoff, K.E., Keszthelyi, L., Kirk, R.L., Mellon, M.T.,

Squyres, S.W., Thomas, N., Weitz, C.M., 2007. Mars reconnaissance orbiter's high resolution imaging science experiment (HiRISE). J. Geophys. Res. E Planets 112, 1–40. doi:10.1029/2005JE002605

Mellon, M.T.M.T., Jakosy, B.M., Jakosky, B.M., 1993. Geographic variations in the thermal and diffusive stability of ground ice on Mars. JGR 98, 3345–3364. doi:10.1029/92JE02355

Mellon, M.T., Boynton, W. V., Feldman, W.C., Arvidson, R.E., Titus, T.N., Bandfield, J.L., Putzig, N.E., Sizemore, H.G., 2008. A prelanding assessment of the ice table depth and ground ice characteristics in Martian permafrost at the Phoenix landing site. J. Geophys. Res. 113, 1–14. doi:10.1029/2007JE003067

Mellon, M.T., Arvidson, R.E., Sizemore, H.G., Searls, M.L., Blaney, D.L., Cull, S., Hecht, M.H., Heet, T.L., Keller, H.U., Lemmon, M.T., Markiewicz, W.J., Ming, D.W., Morris, R. V., Pike, W.T., Zent, A.P., 2009. Ground ice at the Phoenix landing site: Stability state and origin. J. Geophys. Res. E Planets 114, 1–15. doi:10.1029/2009JE003417

Mellon, M.T., Feldman, W.C., Prettyman, T.H., 2004. The presence and stability of ground ice in the southern hemisphere of Mars. Icarus 169, 324–340. doi:10.1016/j.icarus.2003.10.022

Milkovich, S.M., Head, J.W., 2005. North polar cap of Mars: Polar layered deposit characterization and identification of a fundamental climate signal. J. Geophys. Res. E Planets 110, 1–21. doi:10.1029/2004JE002349

Milliken, R.E., 2003. Viscous flow features on the surface of Mars: Observations from high-resolution Mars Orbiter Camera (MOC) images. J. Geophys. Res. 108, 5057. doi:10.1029/2002JE002005

Mischna, M.A., *et al*. 2003. On the orbital forcing of Martian water and CO 2 cycles: A general circulation model study with simplified volatile schemes. J. Geophys. Res. 108, 5062. doi:10.1029/2003JE002051

Mustard, J.F., Cooper, C.D., Rifkin, M.K., 2001. Evidence for recent climate change on Mars from the identification of youthful near-surface ground ice. Nature 412, 411–414. doi:10.1038/35086515

Paige, D.A., Bachman, J.E., Keegan, K.D., 1994. Thermal and albedo mapping of the polar regions of Mars using Viking thermal mapper observations: 1. North polar region. J. Geophys. Res. 99, 25959. doi:10.1029/93JE03428

Paige, D.A., Ingersoll, A.P., 1985. Annual heat balance of martian polar caps: viking observations. Science 228, 1160–8. doi:10.1126/science.228.4704.1160

Phillips, R.J., Zuber, M.T., Smrekar, S.E., Mellon, M.T., Head, J.W., Tanaka, K.L., Putzig, N.E., Milkovich, S.M., Campbell, B. a, Plaut, J.J., Safaeinili, A., Seu, R., Biccari, D., Carter, L.M., Picardi, G., Orosei, R., Surdas Mohit, P., Heggy, E., Zurek, R.W., Egan, A.F., Giacomoni, E., Russo, F., Cutigni, M., Pettinelli, E., Holt, J.W., Leuschen, C.J., Marinangeli, L., 2008. Mars north polar deposits: stratigraphy, age, and geodynamical response. Science 320, 1182–1185. doi:10.1126/science.1157546

Pierce, T.L., Crown, D.A., 2003. Morphologic and topographic analyses of debris aprons in the eastern Hellas region, Mars. Icarus 163, 46–65. doi:10.1016/S0019-1035(03)00046-0

Pierce, T.L., Crown, D.A., 2003. Morphologic and topographic analyses of debris aprons in the eastern Hellas region, Mars. Icarus 163, 46–65. doi:10.1016/S0019-1035(03)00046-0

Piqueux, S., Byrne, S., Kieffer, H.H., Titus, T.N., Hansen, C.J., 2015a. Enumeration of Mars years and seasons since the beginning of telescopic exploration. Icarus 251, 332–338. doi:10.1016/j.icarus.2014.12.014

Piqueux, S., Kleinböhl, A., Hayne, P.O., Kass, D.M., Schofield, J.T., McCleese, D.J., 2015b. Variability of the martian seasonal CO<inf>2</inf> cap extent over eight Mars Years. Icarus 251, 164–180. doi:10.1016/j.icarus.2014.10.045

Plaut, J.J., Picardi, G., Safaeinili, A., Ivanov, A.B., Milkovich, S.M., Cicchetti, A., Kofman, W., Mouginot, J., Farrell, W.M., Phillips, R.J., Clifford, S.M., Frigeri, A., Orosei, R., Federico,

C., Williams, I.P., Gurnett, D. a, Nielsen, E., Hagfors, T., Heggy, E., Stofan, E.R., Plettemeier, D., Watters, T.R., Leuschen, C.J., Edenhofer, P., 2007. Subsurface radar sounding of the south polar layered deposits of Mars. Science 316, 92–95. doi:10.1126/science.1139672

Putzig, N.E., Mellon, M.T., 2007. Apparent thermal inertia and the surface heterogeneity of Mars. Icarus 191, 68–94. doi:10.1016/j.icarus.2007.05.013

Putzig, N.E., Mellon, M.T., Herkenhoff, K.E., Phillips, R.J., Davis, B.J., Ewer, K.J., Bowers, L.M., 2014. Thermal behavior and ice-table depth within the north polar erg of Mars. Icarus 230, 64–76. doi:10.1016/j.icarus.2013.07.010

Putzig, N.E., Mellon, M.T., Kretke, K.A., Arvidson, R.E., 2005. Global thermal inertia and surface properties of Mars from the MGS mapping mission. Icarus 173, 325–341. doi:10.1016/j.icarus.2004.08.017

Richardson, M.I., Wilson, R.J., 2002. A topographically forced asymmetry in the martian circulation and climate. Nature. doi:10.1038/416298a

Schorghofer, N., 2010. Fast numerical method for growth and retreat of subsurface ice on Mars. Icarus 208, 598–607. doi:10.1016/j.icarus.2010.03.022

Schorghofer, N., Aharonson, O., 2005. Stability and exchange of subsurface ice on Mars. J. Geophys. Res. E Planets 110, 1–16. doi:10.1029/2004JE002350

Schorghofer, N., Forget, F., 2012. History and anatomy of subsurface ice on Mars. Icarus 220, 1112–1120. doi:10.1016/j.icarus.2012.07.003

Schwerdtfeger, P., 1963. Measurement of Conducted Flow of Heat in a Sea Ice Cover. Nature 200, 769–769. doi:10.1038/200769a0

Searls, M.L., Mellon, M.T., Cull, S., Hansen, C.J., Sizemore, H.G., 2010. Seasonal defrosting of the Phoenix landing site. J. Geophys. Res. E Planets 115, E00E24. doi:10.1029/2009JE003438

Smith, I.B., Holt, J.W., Spiga, A., Howard, A.D., Parker, G., 2013. The Spiral troughs of Mars as cyclic steps. J. Geophys. Res. Planets 118, 1835–1857. doi:10.1002/jgre.20142

Smith, I.B., Putzig, N.E., Holt, J.W., Phillips, R.J., 2016. An ice age recorded in the polar deposits of mars. Science 352, 1075–1078. doi:10.1126/science.aad6968

Smith, M.D., 2004. Interannual variability in TES atmospheric observations of Mars during 1999-2003. Icarus. doi:10.1016/j.icarus.2003.09.010

Smith, M.D., 2002. The annual cycle of water vapor on Mars as observed by the Thermal Emission Spectrometer. J. Geophys. Res. Planets 107, 25-1-25–19. doi:10.1029/2001JE001522

Smith, M.D., 2008. Spacecraft Observations of the Martian Atmosphere. Annu. Rev. Earth Planet. Sci. 36, 191–219. doi:10.1146/annurev.earth.36.031207.124334

Smith, M.D., Pearl, J.C., Conrath, B.J., Christensen, P.R., 2001. One Martian year of atmospheric observations by the Thermal Emission Spectrometer. Geophys. Res. Lett. 28, 4263–4266. doi:10.1029/2001GL013608

Sori, M.M., Perron, J.T., Huybers, P., Aharonson, O., 2014. A procedure for testing the significance of orbital tuning of the martian polar layered deposits. Icarus 235, 136–146. doi:10.1016/j.icarus.2014.03.009

Squyres, S.W., 1979. The evolution of dust deposits in the Martian north polar region. Icarus 40, 244–261. doi:10.1016/0019-1035(79)90070-8

Stuurman, C.M., Osinski, G.R., Holt, J.W., Levy, J.S., Brothers, T.C., Kerrigan, M., Campbell, B.A., 2016. SHARAD detection and characterization of subsurface water ice deposits in Utopia Planitia, Mars. Geophys. Res. Lett. 43, 9484–9491. doi:10.1002/2016GL070138

Sturm, M., Perovich, D.K., Holmgren, J., 2002. Thermal conductivity and heat transfer through the snow on the ice of the Beaufort Sea. J. Geophys. Res. 107, 1–17. doi:10.1029/2000JC000409

Svitek, T., Murray, B., 1990. Winter frost at Viking Lander 2 site. J. Geophys. Res. 95, 1495–1510. doi:10.1029/JB095iB02p01495

Tanaka, K.L., 2005. Geology and insolation-driven climatic history of Amazonian north polar materials on Mars. Nature 437, 991–994. doi:10.1038/nature04065

Tillman, J.E., Johnson, N.C., Guttorp, P., Percival, D.B., 1993. The Martian annual atmospheric pressure cycle: Years without great dust storms. J. Geophys. Res. 98, 10963. doi:10.1029/93JE01084

Titus, T.N., Kieffer, H.H., Mullins, K.F., Christensen, P.R., 2001. TES premapping data: Slab ice and snow flurries in the Martian north polar night. J. Geophys. Res. 106, 23181–23196. doi:0.1029/2000je001284

Titus, T.N., 2005. Thermal infrared and visual observations of a water ice lag in the Mars southern summer. Geophys. Res. Lett. 32, 1–4. doi:10.1029/2005GL024211

Titus, T.N., Kieffer, H.H., Christensen, P.R., 2003. Exposed water ice discovered near the south pole of Mars. Science 299, 1048–1051. doi:10.1126/science.1080497

Toigo, A.D., Smith, M.D., Seelos, F.P., Murchie, S.L., 2013. High spatial and temporal resolution sampling of Martian gas abundances from CRISM spectra. J. Geophys. Res. E Planets 118, 89–104. doi:10.1029/2012JE004147

Toon, O.B., Pollack, J.B., Ward, W., Burns, J.A., Bilski, K., 1980. The astronomical theory of climatic change on Mars. Icarus 44, 552–607. doi:10.1016/0019-1035(80)90130-X

Vasavada, A.R., Bandfield, J.L., Greenhagen, B.T., Hayne, P.O., Siegler, M.A., Williams, J.P., Paige, D.A., 2012. Lunar equatorial surface temperatures and regolith properties from the Diviner Lunar Radiometer Experiment. J. Geophys. Res. E Planets 117. doi:10.1029/2011JE003987

Vincendon, M., Forget, F., Mustard, J., 2010. Water ice at low to midlatitudes on Mars. J. Geophys. Res. E Planets 115, 1–13. doi:10.1029/2010JE003584

Viola, D., McEwen, A.S., Dundas, C.M., Byrne, S., 2015. Expanded secondary craters in the Arcadia Planitia region, Mars: Evidence for tens of Myr-old shallow subsurface ice. Icarus 248, 190–204. doi:10.1016/j.icarus.2014.10.032

Wagstaff, K.L., Titus, T.N., Ivanov, A.B., Castaño, R., Bandfield, J.L., 2008. Observations of the north polar water ice annulus on Mars using THEMIS and TES. Planet. Space Sci. 56, 256–265. doi:10.1016/j.pss.2007.08.008

Warren, S.G., 1982. Optical properties of snow. Rev. Geophys. doi:10.1029/RG020i001p00067

Whiteway, J.A., Komguem, L., Dickinson, C., Cook, C., Illnicki, M., Seabrook, J., Popovici, V., Duck, T.J., Davy, R., Taylor, P. a, Pathak, J., Fisher, D., Carswell, a I., Daly, M., Hipkin, V., Zent, a P., Hecht, M.H., Wood, S.E., Tamppari, L.K., Renno, N., Moores, J.E., Lemmon, M.T., Daerden, F., Smith, P.H., 2009. Mars water-ice clouds and precipitation. Science (80). 325, 68–70. doi:10.1126/science.1172344

Wood, S.E., Paige, D. A., 1992. Modeling the Martian seasonal CO2 cycle 1. Fitting the Viking Lander pressure curves. Icarus 99, 1–14. doi:10.1016/0019-1035(92)90166-5

Yen, Y.-C., 1981. Review of Thermal Properties of Snow, Ice, and Sea Ice. CRREL Rep. 34pp.

Zent, A.P., Haberle, R.M., Houben, H.C., Jakosky, B.M., 1993. A Coupled Subsurface-Boundary Layer Model of Water on Mars. J. Geophys. Res. 98, 3319–3337. doi:10.1029/92JE02805

Zent, A.P., Hecht, M.H., Cobos, D.R., Wood, S.E., Hudson, T.L., Milkovich, S.M., Deflores, L.P., Mellon, M.T., 2010. Initial results from the thermal and electrical conductivity probe (TECP) on phoenix. J. Geophys. Res. E Planets 115, 1–23. doi:10.1029/2009JE003420

SUPPLEMENTARY MATERIAL

Table 5.1. List of images used for analysis at Louth in Chapter 3.

HiRISE image ID	Emission Angle	Solar Longitude	Local Time
PSP_001370_2505_RED	1.7	133.7	15.0
PSP_001700_2505_RED	9.3	146.4	15.2
PSP_008741_2505_RED	1.2	82.3	14.8
PSP_008886_2505_RED	3.3	87.2	14.8
PSP_008952_2500_RED	4.6	89.5	14.9
PSP_009031_2505_RED	5.0	92.2	14.8
PSP_009242_2505_RED	2.3	99.5	14.9
ESP_017233_2505_RED	9.8	71.2	14.9
ESP_017457_2505_RED	3.6	78.8	14.7
ESP_017589_2505_RED	8.2	83.3	14.9
ESP_017668_2505_RED	4.9	86.0	14.7
ESP_017813_2505_RED	8.6	91.0	14.7
ESP_018235_2505_RED	0.2	105.7	14.9
ESP_018301_2505_RED	3.1	108.0	14.9
ESP_018947_2505_RED	4.9	131.6	14.9
ESP_019013_2505_RED	1.8	134.1	15.0
ESP_026661_2505_RED	4.4	92.1	14.7
ESP_027017_2505_RED	8.3	104.5	14.7
ESP_027782_2505_RED	7.2	132.3	15.1
ESP_035298_2505_RED	0.2	86.0	14.8
ESP_037210_2505_RED	2.5	156.3	15.1
ESP_037276_2505_RED	3.6	159.0	15.3
ESP_044885_2505_RED	0.9	112.8	14.7
ESP_045439_2505_RED	9.0	133.2	14.9
ESP_045887_2505_RED	19.8	150.6	14.4

Table 5.2. From Chapter 3, a summary of our best-fit thermal properties/albedo (for different combinations of AM and PM data) tested back against all TES data (both AM and PM data). We find using AM+PM fits is best for both constant and varying albedo treatments.

Fit Type*	Thermal Inertia (MKS)	Albedo	RMS Error (K)	Reduced Chi-squared Statistic	Mean Residuals (K)	Standard Deviation (K)
AM	2000	0.47	9.520	52.206	7.824	9.513
PM	1800	0.39	9.441	44.328	7.538	8.589
AM+PM	1550	0.42	8.951	39.104	6.974	8.718
AM TI; PM albedo	2000	0.39	9.892	49.179	7.941	8.875
AM	1600	0.12 (offset)	9.013	42.777	7.243	8.940
PM	1650	0.07 (offset)	9.672	46.296	7.695	8.637
AM+PM	1250	0.10 (offset)	8.759	36.952	6.829	8.407
AM TI; PM albedo	1600	0.07 (offset)	9.660	46.298	7.689	8.652

*All fits involved TES target temperatures

Constant Albedo
Varying Albedo

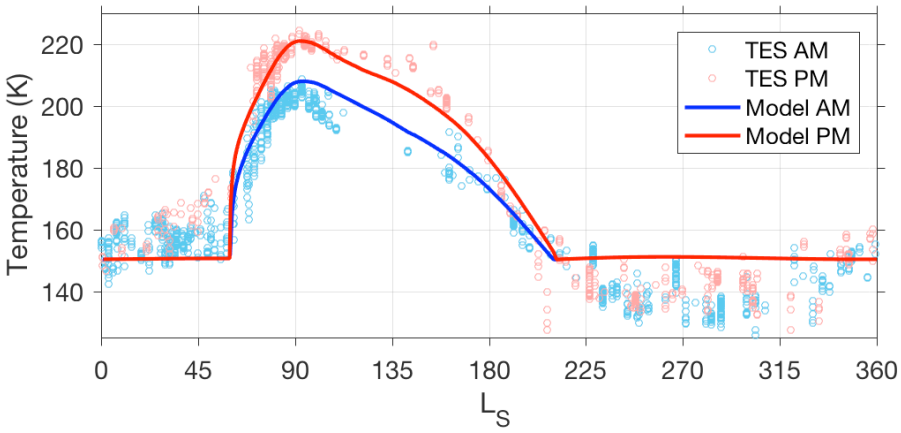

Figure 5.1. Best fit AM+PM with varying albedo, TI=1250, and an albedo offset=0.10.

VITA

Jonathan Bapst — Ph.D. Candidate in Planetary Science

Education

Dual-Title Ph.D., Earth and Space Sciences & Astrobiology, University of Washington, Seattle (*expected February 2018*)

B.S., 2010: Mechanical and Aerospace Engineering, State University of New York at Buffalo

Employment

2010 – present	**Graduate Research Assistant** Advisors: Dr. Shane Byrne, Dr. Joshua Bandfield, and Dr. Stephen Wood Department of Earth & Space Sciences, University of Washington (2010-2014) Lunar and Planetary Laboratory, University of Arizona (2014-present)
Spring 2014	**UW Astrobiology Research Rotation** Tunable Laser Spectroscopy of Short-chained Alkanes Advisors: Dr. Steve Vance and Dr. Lance Christensen Jet Propulsion Laboratory, Pasadena, CA
2009 - 2010	**Undergraduate Research Assistant** Advisor: Dr. Matthew Ringuette Department of Mechanical and Aerospace Engineering, SUNY Buffalo
Summer 2008	**NASA Exploration and Systems Mission Directorate Internship** Research in Power and Propulsion Technologies Division Mentor: David Plachta NASA Glenn Research Center

Refereed Publications (Underlined text includes hyperlink)

Bapst, J., Byrne, S., and A. J. Brown. 2017. "On the Icy Edge at Louth and Korolev Craters". *In press in Icarus*

Bramson, A.M., Byrne, S., **Bapst**, J., 2017. "Preservation of Mid-Latitude Ice Sheets on Mars". *J. Geophys. Res. Planets* 1–17.

Sori, M. M., **Bapst, J.**, Bramson, A. M., Byrne, S., Landis, M. E. 2017. "A Wunda-full world? Carbon dioxide ice deposits on Umbriel and other Uranian moons". *Icarus* 290, 1–13.

Bapst, J., Bandfield, J. L., and S. E. Wood. 2015. "Hemispheric Asymmetry in Martian Seasonal Surface Water Ice from MGS TES". *Icarus* 260, 396–408.

Refereed First Author Conference Abstracts

Bapst, J., and S. Byrne. 2017. "Mass Balance of Polar Icy Outliers: Louth and Korolev Craters". Poster session at 48th Lunar and Planetary Science Conference, The Woodlands, TX.

Bapst, J., and S. Byrne. 2016. "Constraining Water Vapor Abundance on Mars using a Coupled Heat-Water Transport Model and Seasonal Frost Observations". P21A-2075, Poster session at AGU Fall Meeting, San Francisco, CA.

Bapst, J., and S. Byrne, 2016. "Mass Balance Estimates of Louth Crater Water Ice and Climatic Implications". Oral session at 6th International Mars Polar Science Conference, Reykjavik, Iceland.

Bapst, J., and S. Byrne, 2016. "Louth Crater Water Ice as a Martian Climate Proxy". Poster session at 47th Lunar and Planetary Science Conference, The Woodlands, TX.

Bapst, J., and S. Byrne, 2015. "Martian Icy Outliers and Climate History". Poster session at 46th Lunar and Planetary Science Conference, The Woodlands, TX. (E-Poster here)

Bapst, J., Bandfield, J. L., and S. E. Wood, 2014. "Mars Dynamic Albedo: Evidence for Widespread Seasonal H_2O Frost in the Northern Hemisphere from TES, HiRISE and THEMIS". Poster session at 8th International Conference on Mars, Pasadena, CA. (E-poster here)

Bapst, J., Bandfield, J. L., and S. E. Wood. 2014. "Investigating the Timing and Extent of Seasonal Surface Water Frost on Mars with MGS TES". Poster session at 45th Lunar and Planetary Science Conference, The Woodlands, TX. (E-Poster here)

Bapst, J., Bandfield, J. L., and S. E. Wood. 2013. "Identifying and Mapping Seasonal Surface Water Frost with MGS TES". P31C-04, Oral session at AGU Fall Meeting, San Francisco, CA. (Recorded here)

Bapst, J., and S. E. Wood. 2013. "Seasonal Release of Water Vapor by Ground Ice on Mars: Implications for Surface Frosts and Atmospheric Water Abundance". Poster session at 44th Lunar and Planetary Science Conference, The Woodlands, TX. (E-Poster here)

Bapst, J., Wood, S. E. and S. Griffiths. 2012. "The Persistence of Mid-latitude Ground Ice on Mars (Past 1 Myr)". Oral session at Mars Recent Climate Change Workshop at NASA Ames, Mountain View, CA.

Bapst, J., and S. E. Wood, 2012. "The long-term effects of surface frosts, seasonal atmospheric water variation and ice fraction-dependent thermal conductivity on Martian ground ice". Poster session at 43rd Lunar and Planetary Science Conference, The Woodlands, TX.

Bapst, J., and S. E. Wood, 2011. "Modeling of Martian subsurface ice in response to recent (≤1 Myr) orbital progression". Poster session at 5th International Mars Polar Science Conference, Fairbanks, AK.

Bapst, J., and S. E. Wood, 2010. "Quasi-steady-state model of subsurface ice on Mars through obliquity variation". Poster session at 42nd Meeting AAS Division of Planetary Science, Pasadena, CA.

Non-refereed Presentations

Bapst, J., 2017. "Thermal Properties of Martian Ice Sheets". HiRISE Team Meeting, West Yellowstone, MT.

Bapst, J., 2017. "Temperature and Albedo of Martian Ice Sheets". Icy Regolith Workshop, Green Bank Observatory, Green Bank, WV

Bapst, J., 2016. "Louth Crater Ice Mound Thermal Structure". HiRISE Team Meeting, Desert Studies Center, Zyzzyx, CA.

Bapst, J., 2015. "Modeling Louth Crater Ice Mound with TES and THEMIS". THEMIS Team Meeting, Arizona State University, Tempe, AZ.

Bapst, J., 2015. "Louth Crater Ice Mound and Climate Change". HiRISE Team Meeting, Mývatn, Iceland.

Bapst, J., 2013. "Seasonal Release of Water Vapor by Ground Ice on Mars: Implications for Surface Frosts and Atmospheric Water Abundance". Poster session at 4th Annual University of Washington ESS Research Gala, Seattle, WA.

Bapst, J., 2012. "Recent Ice Ages on Mars (≤1 Ma)" Oral session at 3rd Annual University of Washington ESS Research Gala, Seattle, WA.

Bapst, J., 2012. "Steady-state water systems on Mars and consequences of extensive subsurface water reservoirs." Oral session at 2nd Annual University of Washington ESS Research Gala.

Bapst, J., 2011. "Climate Change on Mars." August 17th, 2011, University of Washington Astronomy Public Viewing Night, Jacobsen Observatory, Seattle, WA.

Bapst, J., 2011. "Steady-state water systems on Mars and consequences of extensive subsurface water reservoirs." Oral session at 2nd Annual University of Washington ESS Research Gala, Seattle, WA.

Professional Service and Memberships

- Member of American Geophysical Union
- Member of American Astronomical Society
- Reviewer for Journal of Geophysical Research Planets and Icarus
- Served as Executive Secretary on NASA Review Panel

Awards and Fellowships

- NASA Earth and Space Science Fellowship (2012 – 2015)
- Best Poster in Modern Processes at 4th Annual ESS Gala ($125)
- Chevron Field Camp Support ($600)
- Best Oral Presentation in Planetary Science at 3rd Annual ESS Gala ($100)
- SUNY Buffalo MAE Zimmer Summer Research Award (2009)
- Member of Tau Beta Pi Engineering Honors Society
- SUNY Buffalo Scholar Award (2005-2009)
- SUNY Buffalo Engineering Dean's List

Workshops / Short Courses

- Icy Regolith Workshop: Green Bank Observatory, Green Bank, WV (September, 2017)
- UW Astrobiology Workshop 2014: 3-Day Cruise off the coast of the Olympic Peninsula, WA (Northeast Pacific Ocean) aboard R/V Thomas G. Thompson
- JPL Planetary Science Summer School (June, 2014)
- NASA Astrobiology Institute Nordic Winter School: Hawaii (January 2014)
- UW Astrobiology Workshop 2013: Hell Creek, MT
- Astrobiology Summer School 2013: Santander, Spain
- UW Astrobiology Workshop 2012: NASA JPL, Pasadena, CA
- UW ESS Field Camp: Dillon, MT (3 weeks - June, 2012)

- UW Astrobiology Workshop 2011: Friday Harbor Laboratories, Friday Harbor, WA

Teaching

- Graduate teaching assistant (University of Washington):
    - ESS 104 Prehistoric Life (Winter 2012)
    - ESS 102 Intro. to Space and Space Travel (Spring 2011, Autumn 2011)
- Undergraduate teaching assistant:
    - MAE 335 Intro. to Fluid Mechanics (Spring 2010, SUNY Buffalo)

Educational Outreach

- UA LPL Outreach at Pima Air and Space Museum (Night Wings)
- Pacific Science Center Polar Science Weekend 2014
- UW Earth and Space Sciences Rocking Out (outreach program)
- Volunteer at 2012 Emerald City Comic Con NASA Booth
- Volunteer at 2012 UW ESS Family Day
- Volunteer at UW Astronomy Public Viewing Night